Functional properties of III-V nanowires addressed by Raman spectroscopy

THÈSE N^{O} 7929 (2017)

PRÉSENTÉE LE 29 SEPTEMBRE 2017
À LA FACULTÉ DES SCIENCES ET TECHNIQUES DE L'INGÉNIEUR
LABORATOIRE DES MATÉRIAUX SEMICONDUCTEURS
PROGRAMME DOCTORAL EN SCIENCE ET GÉNIE DES MATÉRIAUX

ÉCOLE POLYTECHNIQUE FÉDÉRALE DE LAUSANNE

POUR L'OBTENTION DU GRADE DE DOCTEUR ÈS SCIENCES

PAR

Francesca AMADUZZI

acceptée sur proposition du jury:

Prof. P. Bowen, président du jury
Prof. A. Fontcuberta i Morral, directrice de thèse
Dr E. Alarcón Lladó, rapporteuse
Prof. M. Johnston, rapporteur
Prof. E. Matioli, rapporteur

ÉCOLE POLYTECHNIQUE
FÉDÉRALE DE LAUSANNE

Suisse
2017

Acknowledgements

After more than four years, I am completing my journey at EPFL. I would like to take the opportunity to thank all the people who contributed in different ways to the success of my work.

The first person I would like to thank is Anna Fontcuberta i Morral. You bet on me, giving the possibility to work with you in your group. Your guidance, passion and support were indispensable to arrive at the end of the PhD. And especially I thank you for the help received when I became a mum.

My work with Raman spectroscopy would have not possible without Esther, to whom I address a special tribute. From the beginning, you helped me immeasurably. Thank you to being an exceptional scientist and a tireless supporter and, over all, a so special friend.

Thank you to all the present and former members of LMSC: Anna, Daniel, Sonia, Yannik, Alberto, Federico, Gozde, Jelena, Heidi, Eleonora, Andreana, Luca, Martin, Dimitry, Jean-Baptiste, Mahdi, Marco, Wonjong, Pablo, Lea and Simon. Thanks for growing the sample, for the many collaborations, for the scientific discussions, for the help and for the great time we spent together.
I would also thank the students and trainee: Jill, Ignasi, Luca , Hubert, Pierre.
Thanks to Monika, who makes our everyday life much easier.

I am also grateful to Prof. Micheal Johnston, Prof. Elison Matioli and Dr. Esther Alarcon Llado for accepting to be the member of my thesis jury.
My acknowledgements goes to Prof. Jordi Arbiol and Sonia Conesa for their transmission electron microscopy investigations in this thesis.
During my PhD I have had a chance to visit the group of Dr. Paulina Plochocka. I would like to thank her for the fruitful discussions and for the collaboration we had.

Thank you Vaghissimi Amici: Odeta, Davide, Framcesca C., Francesca V., Nico, Daniele e Damiano. You have brought a piece of home in Lausanne.

Grazie a Lucia per il suo supporto, specialmente come nonna durante la stesura della tesi.
Un ringraziamento a zia Miriana, per essere molto più che una zia.

Grazie mille ai miei genitori, Alessandro e Maria, per avermi insegnato il valore della cultura e dell'educazione su tutto. Siete dei genitori amorevoli e dei nonni dolcissimi.
Un ringraziamento speciale a Chiara e Arnaldo che sono sempre stati al mio fianco e, nonostante la distanza, non mi hanno mai fatto sentire sola.

Grazie al mio bellissimo bimbo, Alessandro. Hai riempito la nostra vita di gioia e amore. Grazie per darci molto più di quello che chiedi.
In ultimo, il mio ringraziamento va a Raffaele. Grazie per tutto quello che abbiamo costruito insieme. Questa tesi non sarebbe esistita senza il tuo incondizionato amore.

Lausanne, 29 September 2017 Francesca Amaduzzi

Abstract

In recent years, semiconductor nanowires have attracted considerable attention as a result of their unique properties and potential applications in many fields. In particular, they can be very attractive materials for certain optoelectronic and electronic devices, such as lasers, detectors and solar cells, which benefit from the photonic properties of nanowires. In order for these future technologies to become a reality, a good understanding of the functional properties of nanowires is fundamental.

In this thesis we have investigated the optical and the electrical properties of III-V semiconductors nanowires by the means of Raman spectroscopy. Thanks to its non-destructive and spatial resolution, Raman spectroscopy is a powerful contact-less tool for the characterization of semiconductor nanowires. Raman spectroscopy can provide information about crystallinity, orientation, size and chemical composition. In polar semiconductors it is also possible to characterize the free carriers, through the coupling of plasmons with longitudinal optical modes.

Due to the small size and particular morphology of nanowires, the interaction of light can be more complex than in thin films. In particular, the existence of photonic modes alters significantly the corresponding light-matter interaction. In this thesis we exploit the use of photonic modes for the compositional mapping of nanowire core-shell heterostructures and also to circumvent the macroscopic selection rules.

In the first part of this thesis, we have performed Raman scattering measurements on GaAs/AlGaAs core/shell nanowires. We have shown that it is possible to select and characterize regions of the structure with different aluminum content, by performing the measurements at different laser wavelengths. Then, we have shown that the photonic modes can be modified by suspending the nanowires on a trench. We have shown that in this case it is possible to enhance the response of the longitudinal optical phonon mode. We have then applied this configuration for the characterization of the hole concentration on p-type GaAs nanowires in back-scattering geometry.

The second part of the thesis focused on the assessment of free carriers by Raman spectroscopy in systems with an expected high electron mobility: GaAs nanowires with a modulation doped structure and InAs(Sb) nanowires. Raman measurements were performed as a function of the temperature on modulation doped GaAs/AlGaAs nanowires. By characterizing the coupling between free carrier and the LO phonons, we have extracted the concentration and the mobility of charge carriers. We have found that Si donors are mostly ionized for a temperature above 50 K. We have shown that the mobility is limited by interface scattering, with values of

400 cm^2/Vs at room temperature and 2700 cm^2/Vs at low temperature.
Finally, we investigated the electronic properties of InAs(Sb) nanowires as a function of the temperature. The effect of a dielectric coating on the electronic properties was also studied. We have found an increase of mobility and electron concentration with the antimony content , moving from 5100 cm^2/Vs for InAs nanowires, to 17500 cm^2/Vs for InAsSb with35% of antimony at 14 K. Moreover, we have shown that in the case of InAs electrons are located in the accumulation layer at the surface, while for InAsSb our measurements are consistent with the carriers located in the nanowire core.

Key words: III-V semiconductors, Raman spectroscopy, light-matter interaction, GaAs nanowire, radial heterostructure, modulation doping, mobility, LO-phonon plasmon coupling, InAs-InAsSb nanowires, nanowire photonics.

Résumé

Durant ces dernières années, les nanofils semiconducteurs ont attirés beaucoup d'attention par leurs propriétés exceptionnelles et leurs potentielles applications dans de nombreux domaines. Ils sont notamment des matériaux très attirants pour certains appareils optoélectroniques et électroniques tels que les lasers, les détecteurs et les cellules solaires qui mettent à profit leurs propriétés photoniques. Une bonne compréhension des propriétés des nanofils est essentielle afin de faire de cette technologie futuriste une technique de pointe actuelle.

Dans cette thèse, nous avons étudié les propriétés optiques et électriques de nanofils III-V à l'aide de spectroscopie Raman. Des mesures non-destructives, sans contact et une bonne résolution spatiale font de la spectroscopie Raman un important outil de caractérisation des nanofils semiconducteurs. La spectroscopie Raman peut fournir des informations à propos de la cristallinité, l'orientation, la taille et la composition chimique. Dans les semiconducteurs polaires, il est également possible de caractériser les porteurs de charge libres grâce au couplage entre les plasmons et les modes optiques longitudinaux.

En raison de la taille et la morphologie des nanofils, leurs interactions avec la lumière peuvent être plus compliquées que dans les couches minces. En particulier, l'existence de modes photoniques modifie les interactions lumière-matière correspondantes de manière significative. Dans cette thèse, nous tirons profit des modes photoniques pour cartographier la composition chimique de nanofils en hérétostructure noyau-enveloppe et pour contrevenir aux règles de sélection macroscopiques.

Dans la première partie de cette thèse, nous avons effectué des mesures de diffusion Raman sur des nanofils de GaAs/AlGaAs structurés en noyau/enveloppe. Nous avons démontré qu'il est possible de choisir et de caractériser des régions de la structure ayant des teneurs d'aluminium variables en effectuant les mesures avec différentes longueurs d'onde de laser. Ensuite, nous avons montré que les modes photoniques peuvent être modifiés en suspendant les nanofils au-dessus d'une tranchée. Dans ce cas, nous avons démontré qu'il est possible de renforcer la réponse des phonons dans le mode optique longitudinal. Nous avons alors utilisé cette configuration pour la caractérisation de la concentration des trous dans des nanofils de GaAs de type p en géométrie de rétro-diffusion.

La deuxième partie de cette thèse s'est intéressée à l'évaluation des porteurs de charge libres par spectroscopie Raman dans des systèmes dans lesquels une grande mobilité des électrons était attendue : des nanofils de GaAs avec dopage modulé et des nanofils de InAs(Sb). Des mesures Raman à température variable ont été effectuées sur des nanofils de GaAs/AlGaAs avec dopage modulé. En analysant le couplage entre les porteurs de charge libres et les

phonons LO, nous avons extrait les concentrations et les mobilités des porteurs de charge. Nous avons découvert que les donneurs Si sont presque ionisés à une température au-dessus de 50 K. Nous avons montré que la mobilité est limitée par la diffusion à l'interface, avec des valeurs de 400 cm^2/Vs à température ambiante et 2700 cm^2/Vs à basse température. Pour terminer, nous avons étudié les propriétés électroniques de nanofils de InAs(Sb) en fonction de la température. L'effet d'un revêtement diélectrique sur les propriétés électroniques a aussi été étudié. Nous avons trouvé une augmentation de la mobilité et de la concentration d'électrons avec la teneur d'antimoine, allant de 510 cm^2/Vs pour des nanofils de InAs à 17500 cm^2/Vs pour du InAsAb avec 35% d'antimoine à 14 K. De plus, nous avons montré que dans le cas du InAs, les électrons sont situés dans la couche d'accumulation à la surface, tandis que pour le InAsSb, nos mesures sont cohérentes avec des porteurs de charge situés dans le noyau du nanofil.

Mots-clés : Semiconducteurs III-V, spectroscopie Raman, interaction lumière-matière, nanofil de GaAs, hétérostructure radiale, modulation du dopage, couplage phonon-LO plasmon, nanofils de InAs-InAsSb, photonique de nanofil.

Contents

Acknowledgements **i**

Abstract (English/Français/Italiano) **iii**

List of figures **ix**

List of tables **xi**

1 Introduction **1**
1.1 Towards III-V semiconductor nanostructures 2
1.2 Nanowires 3
1.2.1 Nanowire properties 3
1.2.2 Applications based on nanowires 4
1.2.3 Nanowire growth 4
1.3 Review on Raman spectroscopy techniques applied on semiconductor nanowires 7
1.4 Electronic properties detected by Raman spectroscopy 11
1.4.1 Photoluminescence spectroscopy 13
1.4.2 TeraHertz spectroscopy 15
1.5 Outlook of my thesis 17
1.6 Papers included in my thesis work 17

2 Raman scattering **21**
2.1 Phonon dispersion in zinc-blende and wurtzite structures 22
2.2 Phonon modes of ternary alloys 24
2.3 Macroscopic theory of Raman scattering 25
2.4 Microscopic theory of Raman scattering 26
2.5 Raman selection rules in zinc-blende and wurtzite structures 28
2.6 Surface optical modes 29
2.7 Raman scattering by LO phonon-plasmon coupled modes 30
2.8 Raman spectroscopy set-up 33

3 The role of Photonic modes in nanowires in Raman scattering **37**
3.1 Introduction 38
3.2 Probing inhomogeneous composition in core/shell nanowires by Raman spectroscopy. 42

3.2.1 Abstract . . . 42
3.2.2 Introduction . . . 42
3.2.3 Experiment . . . 43
3.2.4 Results and Discussion . . . 45
3.2.5 Conclusion . . . 49
3.2.6 Acknowledgments . . . 49
3.3 Tuning the response of non-allowed Raman modes in GaAs nanowires . . . 50
3.3.1 Abstract . . . 50
3.3.2 Introduction . . . 50
3.3.3 Experiment . . . 51
3.3.4 Results and Discussion . . . 52
3.3.5 Conclusion . . . 59

4 Determination of electronic properties with Raman spectroscopy 61
4.1 Modulation-doped structures . . . 62
4.1.1 Introduction . . . 62
4.1.2 Inelastic light scattering in modulation-doped structures . . . 65
4.1.3 Nanowires with a modulation-doped structure . . . 67
4.1.4 Simulations . . . 70
4.1.5 Experimental . . . 70
4.1.6 Results . . . 71
4.2 InAs-InAsSb nanowires . . . 75
4.2.1 Introduction . . . 75
4.2.2 Raman scattering by LOPPCM in InAs and $InAs_{1-x}Sb_x$ bulk material . . . 75
4.2.3 Theory of LO phonon plasmon coupled mode in a ternary alloy . . . 76
4.2.4 Experiment . . . 78
4.2.5 Effect of Sb concentration . . . 79
4.2.6 Effect of the temperature . . . 81
4.2.7 Effect of surface passivation . . . 82
4.2.8 Discussion: origin of carrier and scattering mechanism . . . 83

5 Conclusions and Outlook 87

A Supporting Information 91
A.1 Growth protocol . . . 91
A.2 Movie . . . 91

Bibliography 108

Curriculum Vitae 109

List of Figures

1.1 Scheme of Molecular Beam Epitaxy 5
1.2 VLS growth process of GaAs NWs 6
1.3 Raman scan along a nanowire presenting ZB and WZ structure 7
1.4 Phonon confinement On Ge NW 8
1.5 Surface mode of GaP NW in different media 9
1.6 Surface mode of GaAs NW with different diameters 10
1.7 Raman line scan for GaAs NW with antenna 10
1.8 Raman spectroscopy on $GaAs_{1-x}Sb_x$ NW 11
1.9 Local Vibrational Modes 12
1.10 Raman spectra of p-type GaAs NWs 13
1.11 PL and PLE spectra for $GaAs/Al_{0.35}Ga_{0.65}As$ NW 14
1.12 Decay of photoconductivity for modulation doped and undoped NWs 15
1.13 Conductivity spectra for the modulation doped and undoped NWs 16

2.1 Schematic representation of phonon dispersion of GaAs for ZB and WZ phase . 22
2.2 Optical phonon energy of $Al_xGa_{1-x}As$ as a function of Al content 24
2.3 Feynman diagram representing the first order Raman process 27
2.4 backscattering configuration for NWs 29
2.5 Position of the SO mode for GaAs NW embedded in air as function of phonon wavevector times nanowire radius. 31
2.6 Frequency position of the coupled modes 32
2.7 Raman setup 34

3.1 Absorption efficiency of individual Ge NWs with different diameters 38
3.2 Absorption efficiency as a function of wavelength and radius of a Ge NW 39
3.3 Diameter dependence of the analytical solution and FDTD simulation for cylinder with and without Au substrate 40
3.4 HAADF-STEM of $GaAs/Al_xGa_{1-x}As$ core/shell NWs 44
3.5 Raman spectra of $GaAs/Al_xGa_{1-x}As$ core/shell NWs 45
3.6 Simulated cross-sectional maps of the internal field energy density distribution for $GaAs/Al_xGa_{1-x}As$ core/shell NW 48
3.7 Raman spectra of GaAs NWs 52
3.8 Experimental scattering geometry and polar plots for the TO and LO modes . . 54

3.9 Calculated LO/TO ratio by Raman selection rules 55
3.10 Calculated electric field intensity squared maps 56
3.11 Raman spectra of p-type GaAs NWs in backscattering configuration 57

4.1 Bending of the conduction band for GaAs-$Al_{1-x}Ga_xAs$ modulation doped heterojunction 62
4.2 History of temperature dependence of the Hall mobility for modulation-doped structures 63
4.3 Scattering mechanisms in modulation doped system 64
4.4 Light scattering spectra of modulation doped quantum well GaAs-AlGaAs heterostructures 66
4.5 Scheme of modulation-doped NWs 68
4.6 Structure of the modulation doped core-multishell GaAs-AlGaAs with distribution of electrons in the quantum well shell 69
4.7 Simulation of the electron density in modulation doped NWs 70
4.8 Raman spectra of un-doped and modulation-doped NWs at 14 K and T_{room} . . 72
4.9 Temperature evolution of electron concentration for undoped and modulation-doped NWs 73
4.10 Temperature evolution of electron mobility for undoped and modulation-doped NWs 73
4.11 Horizontal linescan of electron density distribution through the NW center . . 74
4.12 Raman spectra in back scattering geometry of n-type (100) InAs 76
4.13 Raman spectra of n-type $Al_{0.25}Ga_{0.75}As$ 77
4.14 Coupled-modes frequencies vs. electron density in $InAs_{0.65}Sb_{0.35}$ 79
4.15 Raman spectra of $InAs_{1-x}Sb_x$ NWs 80
4.16 Electrons concentration and mobility for $InAs_{1-x}Sb_x$ at T_{room} 81
4.17 Raman spectra of InAs and $InAs_{0.65}Sb_{0.35}$ in the range 14-293 K 82
4.18 Electron concentration and mobility for InAs and $InAs_{0.65}Sb_{0.35}$ at different T . 83
4.19 Raman spectra of InAs and $InAs_{0.65}Sb_{0.35}$ pure and coated with Al_2O_3 84
4.20 Electron concentration and mobility for different temperature for InAs and $InAs_{0.65}Sb_{0.35}$ coated with Al_2O_3 85

A.1 Growth protocol Table 91
A.2 Electric energy density for GaAs/$Al_{0.5}Ga_{0.5}As$ excited by a top plane wave 92

List of Tables

2.1 Raman optical phonon modes in WZ GaAs 23
2.2 Raman optical phonon modes in WZ InAs 23
2.3 Selection rules for ZB and WZ structures in backscattering 29

3.1 Optical phonon energies with the relative alloy compositions 46
3.2 Input parameters for the coupled phonon-plasmon modes Raman cross section 59

4.1 Input parameters for the LOPCM line-shape model for $InAs_{0.65}Sb_{0.35}$ 78

1 Introduction

This thesis is dedicated to the characterization of the functional properties of III-V nanowires by Raman spectroscopy. Understanding the functional properties is a fundamental step for the use of nanowires in future applications. Beside to new controlled ways to growing complex nanostructures, also new characterization tools are needed to be developed for their study, due to the small size. The characterization of nanowires is also important in the framework of the development of devices in order to predict the possibility of their use in future technologies.

In the first part of this chapter, we introduce nanowires and their role in the history of down scaling of devices. We will describe the new physical properties, their possible applications and how they can be obtained.

In the second part, we review the use of Raman spectroscopy on nanowires. Additionally, we introduce the technique of Photoluminescence and TeraHertz spectroscopy as contact-less techniques, for the assessment of electronic properties of nanowire systems.

At the end, an overview of the thesis is given.

1.1 Towards III-V semiconductor nanostructures

The semiconductor transistor was invented at the Bell labs in 1947 by John Bardeen, Walter Brattain and William Shockley [1]. They were aiming to find an alternative of the amplifying vacuum tubes using a solid state device. It was a breakthrough which enabled the development of the electronics that now we are so used having in our daily life. Moreover, it marked the beginning of an increased of interest in the study of semiconductor materials.

This invention, together with the development of the integrated circuits, represents the starting point of the so-called " Microelectronic-age", or "Silicon-age", the material that has practically dominated the electronics market. The invention of integrated circuits developed by Jack Kilby at the Texas Instruments in 1957 represent the second big step in the history of electronics [2]. The planar manufactured process allowed to create and connect multiple transistors concurrently.

Since that moment, the progression of circuit fabrication followed the Moore's law, with a doubling of the number of transistors every 18 month. The benefits to the circuits characteristics in terms of the reduction of the size, as the higher performance and the less power consumption, explain the tremendous accelerated down-sizing.

At the moment, the electronic industry has reached the ~10 nanometer scale. At these dimensions, the capability limit with the top-down conventional fabrication methods is a serious obstacle to a further down-scaling. The top-down approach consists on the fabrication of nanostructures from the bulk material. The emergence of a different methodology called bottom-up brought a new perspective in overcoming the limitation of the down-scaling [3]. The bottom-up synthesis method implies that the nanostructures synthesized onto a substrate by stacking atoms onto each other. In this context, we can understand the increased interest during the last years for nanostructures, as nanowires and nanomembranes, realized with the bottom-up method.

Even if the commercial market of integrated circuits is dominated by Silicon, III-V compound semiconductors are catching the interest for modern electronics and integrated optoelecronics. In fact, most of the III-V semiconductors present a higher carrier mobilities and higher carrier velocities than Si [4]. This results in an improvement of the device performance. From another point of view, silicon has indirect bandgap. On the contrary, most of III-V semiconductors have a direct band-gap which makes them better suited for optoelectronic devices, such as laser diodes and solar cells. The integration of III-V materials with the existing Si technology would be advantageous for the modern technology [5].

The integration of the two materials presents some challenging issues due to the effect of the lattice and thermal mismatches, and the non-polarity of silicon and polarity of III-V semiconductors. Growing III-V semiconductors in the form of nanostructures can minimize these effects. Nanowires seem to be among the most promising building-blocks of nanodevices.

1.2 Nanowires

Nanowires are filamentary crystals with a tailored diameter ranging between few and hundred nanometers. Nanowires were reported for the first time by Wagner and Ellis [6] in the early 1960's. It was demonstrated the possibility to grow microstructures with a high aspect ratio, using a new growth mechanism called Vapor Liquid Solid (VLS).

Nanowires, initially called Whiskers at the time of their discovery, did not attract attention immediately. Only in the early 1990's the interest in nanowires was renewed thanks to the work of Hiruma et al. [7], where the Vapor Liquid Solid mechanism was used with droplets at the nanometer scale. The resulting GaAs and InAs nanowire structures were used to demonstrate a functional p-n junction device. Thereafter the field showed a rapid growth, attracting many laboratories to enter into the nanowire community. As the research on the growth mechanism was catching the attention of scientific community, experiments of electro-transport, mechanics and optics were implemented. The possibility to combine materials with strongly different lattice parameter limiting strain-related defect contributed to rise the interest of this emerging field. At the present time, different growth mechanisms and fabrication techniques are used to synthesized nanowires, made of many different materials: Si, ZnO, GaN, GaAs and so on.

1.2.1 Nanowire properties

Nanowires have attracted considerable attention not only for their promising potential applications in micro-electronics. Thanks to their particular morphology, they present unique properties, which are not observed in bulk materials. Indeed, the physical properties of nanowire materials, like crystal and electronic band structure, can be different respect to the bulk properties. In nanowire form, many materials can be grown in a crystal phase, which is not stable in the correspondent bulk material. This gives the possibility to study new materials, such as wurtzite for GaAs.

Moreover, nanowire structures allow studying new physical effects. The main ones are connected with surface and finite-size properties. For example, the effect of surface states in nanowires are dominant due to the high length-diameter ratio. The presence of surface states are detrimental for both the optical and electronic properties. Nanowires coated with a wide band-gap material are the most studied structure to limit this effect. Furthermore, the finite -size and the shape anisotropy are responsible for special interaction of light with nanowires.

Nanowires give also the possibility to build complex structures, as heterostructures, in two different ways: along and across the nanowire axis, giving rise to axial and radial heterostructures, respectively. In axial heterostructures, mismatched materials are combined along the nanowire, thanks to a radial strain release. In radial heterostructures, shells of one or more materials can be grown around a nanowire core. The possibility to grow radial heterostructures leads to grow more complex structures, such as modulation doping nanowire structure. With this arrangement, two or one dimension gas on the facets or on the edge of the core can be

achieved respectively.

1.2.2 Applications based on nanowires

Thanks to their unique properties, nanowires enable applications potentially enhancing the device performance in many fields, such as electronics, opto-electronics, photonics, biosensing, energy conversion and storage. Some examples are presented in the following.

As we have mentioned, nanowires can be used as field effect transistor, i.e. the main component of integrated circuits. Thanks to the good gate controllability over the channel, nanowire Field Effect Transistor with a cylindrical gate-all-around can offer efficient device [8]. Moreover, nanowires offers also the possibility of implementing Tunnel-FET scheme [9]

In the field of energy conversion, the geometry of nanowires, which is advantageous to capture light and to minimize material usage make them ideal building blocks for high efficiency solar cells [10]. Moreover, the low thermal conductivity of nanowires renders them suited for thermoelectric devices [11].

The study of nanowires as photonic components has been widely exploited, because of the properties to confine electromagnetic waves in the radial direction and to guide light in the axial direction. These properties arise from the size of nanowire diameter, smaller than the light wavelength in the visible range. The waveguiding behavior and the gain media for light amplification allow a highly directional lasing. The first ZnO nanowire laser has been demonstrated in 2001. [12] Consequently, nanowires made of various materials are used as lasers, covering a wide range of the visible and infrared range [13, 14]

Finally, nanowires can be interfaced with living cell for delivery drugs or doing sensing activity. Thanks to their small diameter, nanowire reduce the invasiveness and the high surface volume ration ensures a good interaction with the cell [15]

1.2.3 Nanowire growth

The growth of semiconductor nanowires has taken great advantage of growth techniques originally developed for the growth of semiconductor materials on plane (2D). Among them, the most used techniques to grow high quality III-V nanowires are the metal-organic chemical vapour deposition (MOCVD), and the molecular beam epitaxy (MBE). All the nanowires characterized in this thesis were produced by MBE, which is briefly described in the following section.

Molecular Beam Epitaxy (MBE)

Molecular beam epitaxy (MBE) is an epitaxy method for thin-film deposition of single crystals, originally invented in the late 1960s at Bell Telephone Laboratories by J.R. Arthur and A.Y.

Cho [16]. This technique, widely used in the manufacture of semiconductor devices, takes place in ultra-high vacuum environment (typically 10^{-8} to 10^{-12} Torr). In solid source MBE, ultra-pure elements such as gallium and arsenic are heated in separate effusion cells. When As begins to sublimate and Ga to evaporate, they form extremely low density jets (molecular beam) directed toward a heated growth substrate (see Fig. 1.1). The most important aspect of MBE is the deposition rate, that allows the material to grow epitaxially. Indeed, lower growth rates, resulting from lower beam fluxes, can ideally yield the creation of close-to-perfect interfaces and extreme-purity materials. The beam flux can be controlled by a shutter and the temperature of the effusion cells.

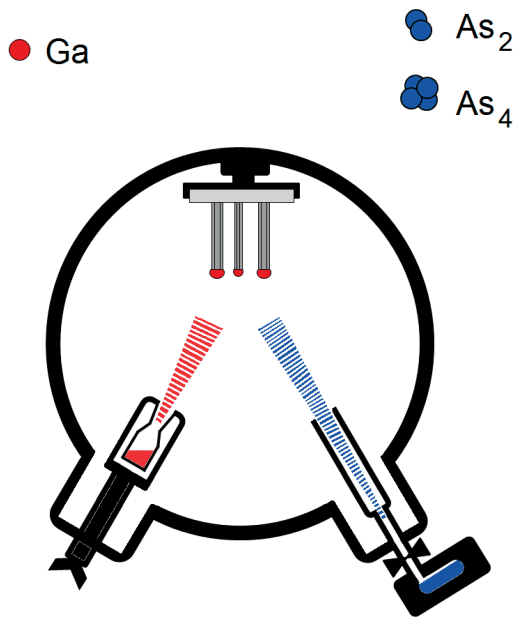

Figure 1.1 – Scheme of Molecular Beam Epitaxy, with the use directly of Gallium as a catalyst.

Nanowire growth by MBE relies on two main mechanisms: the selective area epitaxy (SAE), involving a patterned mask deposited on a semiconductor substrate to ensure exclusive growth of the exposed substrate, and the vapor-liquid-solid (VLS) growth. In the present work, VLS mechanism has been used. This mechanism is mainly described by three stages, as reported by Wagner and Ellis in 1964 [6] to explain the growth of silicon microwires from the gas phase, catalyzed by gold particles placed upon a silicon substrate. The three main stages of VLS growth are the following:

1. Gold droplets are deposited upon the wafer substrate from which the wires are to be grown.
2. The substances to be grown are introduced as a vapor. The liquid surface of the droplet absorbs the growth materials, which diffuse into the catalyst droplet.
3. When supersaturation level of growth elements in the catalyst droplet is reached, pre-

cipitation occurs and crystal growth can subsequently take place from nucleated seeds at the liquid–solid interface. Nanowire growth is then sustained by a constant feeding of the materials through the catalyst, as well as through diffusion on the substrate or side facets for certain species.

Even if gold is extensively used as the catalyst in nanowire growth for many compounds and substrates, it can be deleterious if it comes to be incorporated in the semiconductor, either during growth or afterward by diffusion. Indeed, in certain semiconductors, gold atoms act as deep traps, scattering and non-radiative recombination centers for the electronic carriers. For these reasons, gold is generally banned from growth process of nanowires requiring either high carrier mobilities and/or high luminescence.

An alternative approach to prevent the inclusion of gold in GaAs nanowires is called self-catalyzed growth, and takes advantage from the direct use of a group III (Ga or In) droplet to absorb vapor phase particles. With respect to the Au-catalyzed growth method, this approach, also known as catalyst-free or Ga-assisted growth. It guarantees no-gold incorporation, with the aforementioned advantages in terms of mobilities and luminescence yield. In this case, the growth substrate is formerly covered by a SiO_2 layer. This coating does not allow As_2/As_4 adatoms to stick, but can traps Ga atoms. The accumulation of diffusing Ga adatoms on the substrate leads to the formation of nanodroplets. Above a certain size, these droplets start to absorb and include the arsenic molecules. Once arsenic concentration in the droplets overcome its solubility, GaAs compounds precipitate to the bottom of the droplets and the nanowires start to grow [17]. A diagram of this growth process is presented on Figure 1.2. Even if the growth is a non-equilibrium process, an approximate value for the arsenic solubility can be estimated from Ga-As phase diagram for a given temperature.

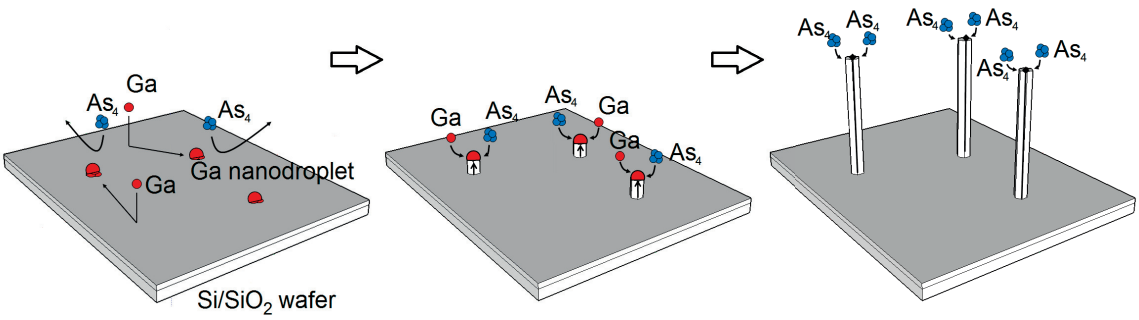

Figure 1.2 – VLS growth process of GaAs nanowires. In the first step droplets formation is shown, followed by the nanowires growth and the termination phase.

Ga-droplets are formed and VLS (Vapor Liquid Solid) can be achieved in Ga-rich conditions. By changing it to As-rich conditions and decreasing the temperature from 600-700°C to 400-500°C, 2D growth typical for Molecular Beam occurs. In this condition, it is possible to grow radial shell around the core.

1.3 Review on Raman spectroscopy techniques applied on semiconductor nanowires

Thanks to its non-destructive nature and spatial resolution, micro-Raman spectroscopy is a powerful tool for the characterization of nanostructures. Raman scattering is widely used for probing optical phonons at Γ point in semiconductors. It gives information about the crystallinity, orientation, strain, size, chemical composition, electronic structure and temperature. Here, we review the main results of Raman scattering by optical phonons on nanowires. We start by presenting the possibility of Raman spectroscopy to assess the crystal phase in nanowires. III-As bulk materials exhibit a zinc-blende structure. However, nanowires can also show a wurtzite structure, or a mixture of the two phases.

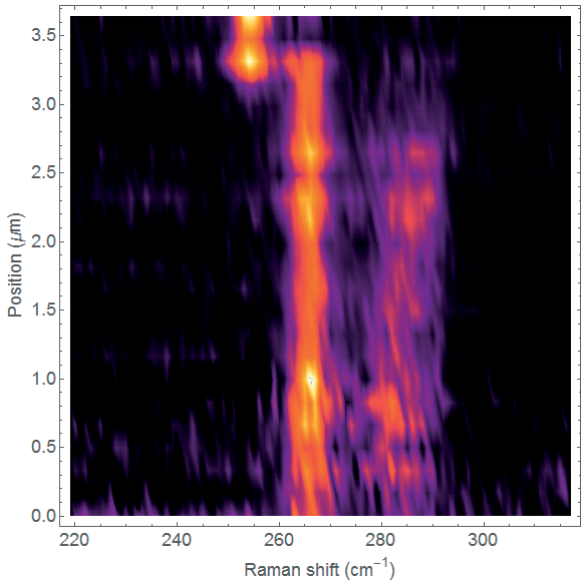

Figure 1.3 – Raman scan along a nanowire presenting zinc-blende and wurtzite structure with light incident perpendicular to the nanowire axis.

Spatially resolved Raman spectroscopy experiments give information on the lattice structure. For example, the presence of the peak at ~258 cm^{-1} associated to the wurtzite structure in Ga As can help to identify the corresponding domains [18]. As an illustration of this, Fig.1.3 shows a Raman scan along a nanowire presenting both zinc-blende and wurtzite structure with light incident perpendicular to the nanowire axis. In the lower part of the scan TO and LO mode of zinc-blende GaAs are observed. The upper part of the scan is characterized by the presence of a peak at lower frequency of TO mode, distinctive of the wurtzite phase.

Now, we discuss the effects on the Raman scattering as a function of the size of nanowires. Usually, the phonon peaks in nanostructures are similar to the bulk. However, decreasing the size to few nanometers, phonon modes get confined within the nanowire material. Due to the uncertainty of the wavevector, the Raman lines get contribution of phonons away from the center of the Brillouin zone. This results in the broadening and shift of the Raman peaks.

Fig.1.4 shows a linescan of Raman spectra nanowire formed by a crystalline Ge core with around an amorphous Ge shell [19]. The changes in intensity and energy of the main peak related to crystalline germanium are associated to the confinement of phonons. In fact, the diameter of the core varies along the nanowire, down to few nanometers.

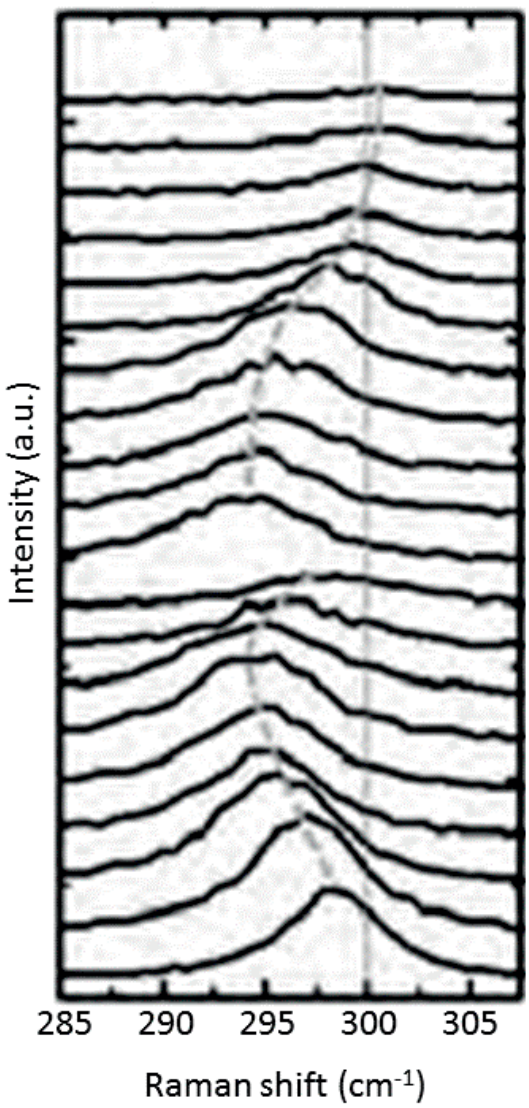

Figure 1.4 – Raman scan along a thin Ge nanowire. Adapted from [20]

Apart from the phonon confinement, another effect of the reducing size is the appearance of new modes, such as the surface optical modes. Surface optical modes originate at the interface of materials with different dielectric constants. Thanks to the high surface-volume ratio, several works report the presence of an extra-peak with frequency between TO and LO phonon in nanowires [21, 22]. Their energy are dependent on the dielectric constant of the medium surrounding the nanowire. Fig.1.5 shows the dependence with the dielectric constant

of the medium of the surface optical mode for gallium phosphide nanowires [22]. We can observe that the surface optical mode down shift, increasing the dielectric constant of the medium.

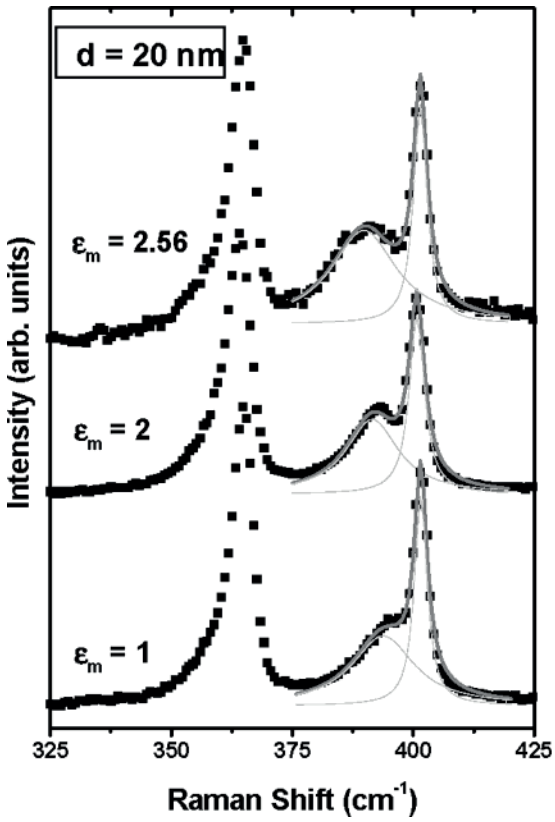

Figure 1.5 – Raman spectra of GaP nanowires recorded in three different media with different dielectric constants. Reprinted with permission from Ref. [22]. Copyright (2003) American Chemical Society.

Moreover, the surface optical phonons are dependent on the diameter of the wire. The trend of the position in function of the diameter can be observed in Fig.1.6, where Raman spectra for GaAs nanowires with different diameters are shown [21]. As expected from theory (see Sec 2.6), surface optical mode shifts to higher wavenumber increasing the diameter.

Another phenomenon due to the longitudinal shape of the nanowires is the so-called "Raman antenna effect": the enhancement response of the Raman scattering for light polarizations along the nanowire axis [23, 24]. This enhancement is dependent on the diameter of the wire and on the wavelength of the incident light. These features suggest a resonant nature. This effect is extensively treated in Chapter 3. Here, it is also worth mentioning that Raman spectroscopy can be used to demonstrate the localization of light by using a nanoscale bowtie antenna array around the nanowire [25]. In this work, it was demonstrated that a highly dense arrays of bow/tie antennas around a GaAs nanowire are able to modify the light polarization response. Raman scans along the nanowire with antennas 1000 nm apart for longitudinal

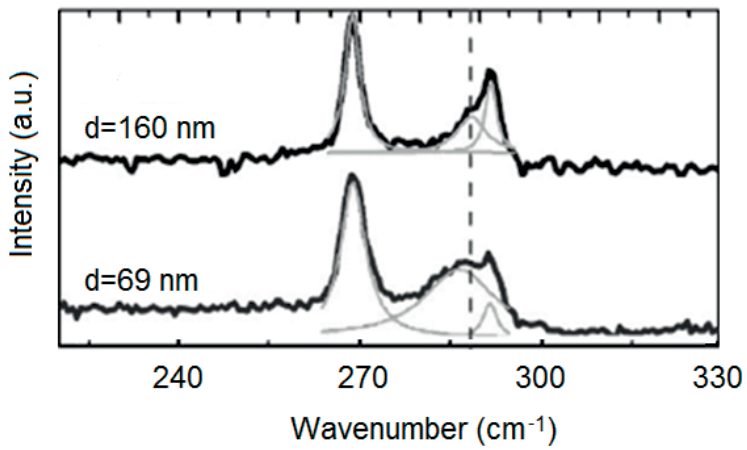

Figure 1.6 – Raman spectra of GaAs nanowires with two different diameters. Adapted from [20].

and transverse polarized light was used. For longitudinally polarized light, the TO peak is homogeneous along the full nanowire. On the other hand, transverse polarization shows the peaks of the Raman intensity between the nanoantennas. Because the Raman signal is directly linked to the local internal field, the results show the ability of nanoantennas to modulate the absorption inside the nanowire for light polarized perpendicular to the nanowire.

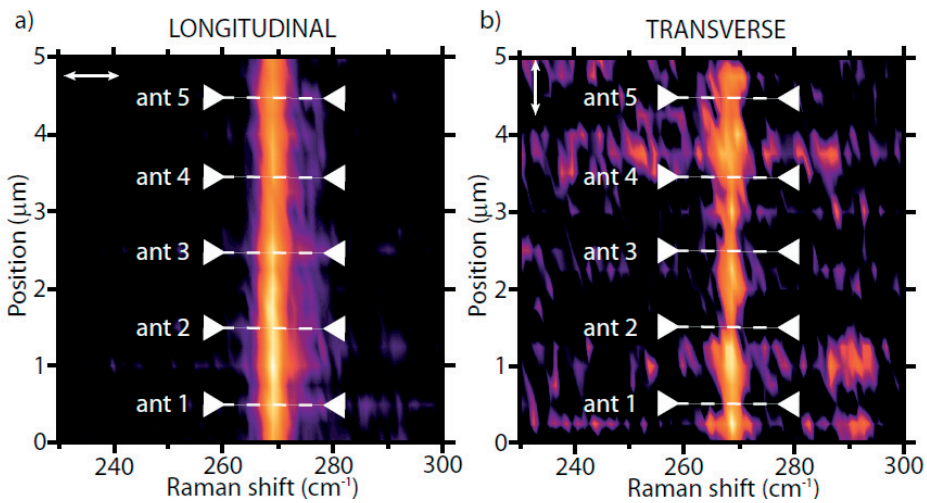

Figure 1.7 – Raman shift line scan along the GaAs nanowire with an array of bow tie antenna with a distance of 1000 nm for parallel (a) and perpendicular (b) polarization at 647 nm wavelength. From Supporting Informations of Ref. [25].

Raman spectroscopy was also used to probe the chemical composition of nanowires [26, 27]. For example, Raman spectroscopy can determine the composition of $GaAs_{1-x}Sb_x$ nanowires, as shown in Fig. 1.8 [26]. The panel a) of Fig. 1.8 shows Raman spectra of $GaAs_{1-x}Sb_x$ nanowire with different x composition. An increase of the fraction of antimony leads a shift of alloy modes to lower wavenumber. The phonon energies of the modes are obtained from Lorentzian

fits of each spectra and reported in the panel b) of Fig. 1.8. The phonon energies are compared with the theoretical estimation of the alloy phonon modes. This comparison gives the possibility to evaluate inhomogeneities in composition.

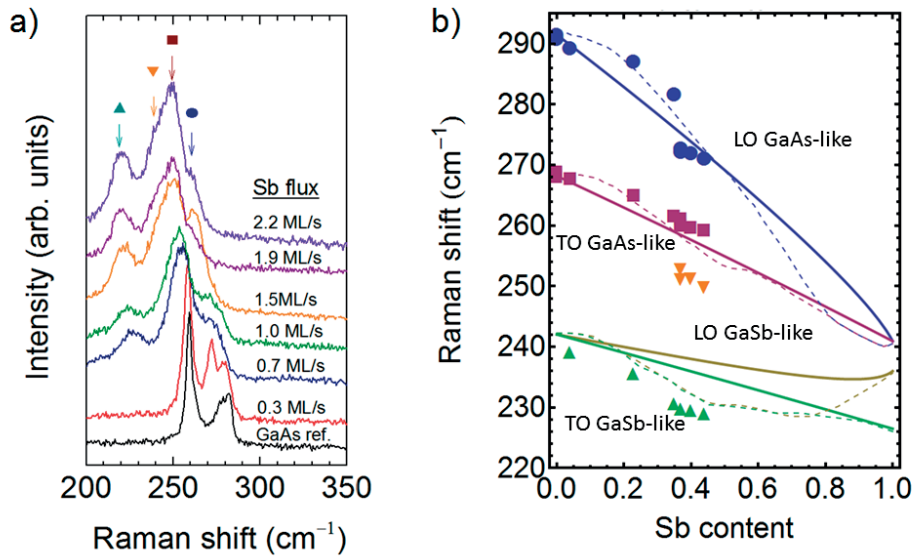

Figure 1.8 – a) Raman spectra of $GaAs_{1-x}Sb_x$ nanowires for different x content. b) Phonon energies of alloy modes as a function of Sb content. Adapted from [26].

Resonant Raman scattering has also been used to investigate the electronic band structure in nanowires [28, 29]. In fact, when the energy of the incident light approaches a real electronic state, an enhancement of the Raman scattering occurs. Varying the excitation energy of light or the energy of the electronic transition (for example with pressure or temperature) give direct access to the energy of the electronic transition. By applying this technique, Ketterer et al. [28] found that the band gap of wurtzite and zinc-blende GaAs is equivalent.

1.4 Electronic properties detected by Raman spectroscopy

The measurement of doping characteristics and electronic properties of a single nanowire is a challenging task. In addition to crystallinity, orientation, size and chemical composition, Raman spectroscopy can assess the type and concentration of dopants. Moreover, Raman spectroscopy can detect free charge carriers in polar semiconductors. Thanks to its non-destructive and contact-less nature, Raman spectroscopy is ideally suited for nanowire studies.

Local vibrational modes, detected by Raman spectroscopy, can give information about impurity lattice sites. For example, Si and Be are widely used dopants to produce n-type or p-type GaAs layes by molecular beam epitaxial growth. Both atoms are lighter than Ga and As, which form the host lattice, and give rise to local vibrational modes (LVM) with frequencies higher than those of intrinsic GaAs phonon modes. For a given dopant atom, the frequency and the fine structure of the LVM indicates the lattice site occupied by the atom. This local vibrational

mode spectroscopy became extremely important to understand and control the concentration and the position of dopants in the nanowire during growth. For example, combining local vibrational mode spectroscopy with electrical measurements, it has been found that the p-doping is governed by the incorporation of Si atoms from the side facets during the radial growth of the GaAs nanowires(Fig. 1.9) [30].

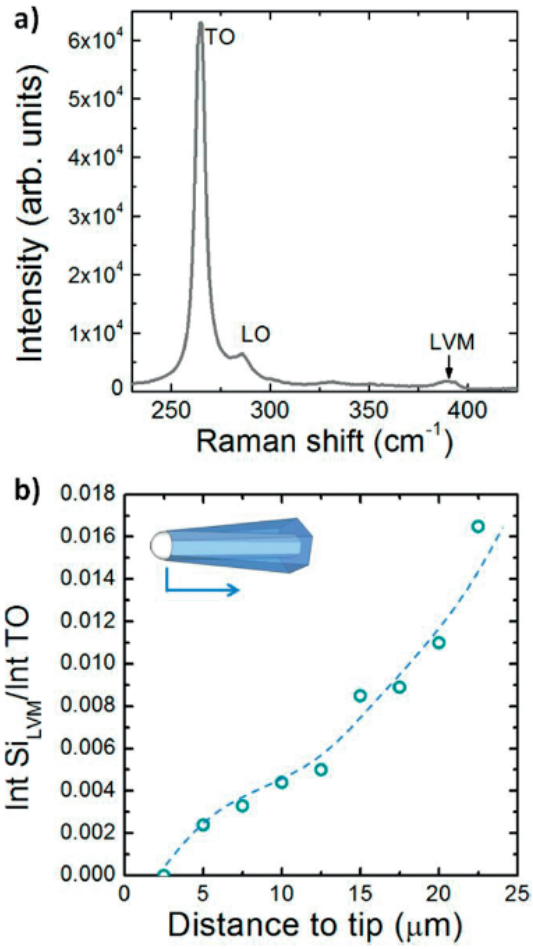

Figure 1.9 – a)Raman spectrum of a single nanowires doped with Silicon. The Local Vibrational mode at 393 cm^{-1} corresponds to the incorporation of Silicon in arsenic sites; b) Spatial dependence of the intensity ratio between the LVM and TO modes along the nanowire. Reprinted from [30], with the permission of AIP Publishing

The possibility to obtain information on the carrier concentration and mobility in polar semiconductors, using Raman scattering comes from the interaction between collective carrier oscillations (plasmon) and the electric field of the LO phonons. Because of this interaction, a bound state of two elemental excited particles is formed, the LO phonon-plasmon coupled modes, which have phonon-plasmon mixed character. Raman scattering by LOPCMs has been studied by many authors in polar bulk semiconductors. In n-type III-V semiconductors, two coupled modes appear in the spectrum [31]. For p-type III-V semiconductors, as a

consequence of the lower mobility of holes, only one coupled mode LOPCM is observed in the spectra with a position between LO and TO peaks [32]. Literature on Raman scattering by LOPCMs in nanowires is less frequent. Ketterer et al. [33] were able to determine the hole concentration and mobility using Raman spectroscopy in forward scattering geometry of GaAs nanowires with different Si-doping concentration (Fig. 1.10).

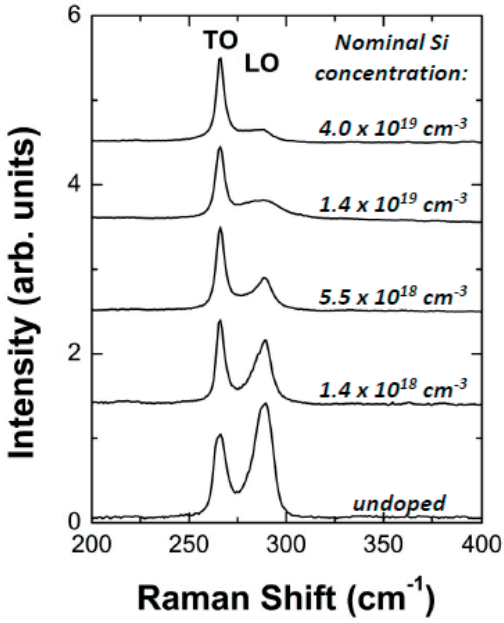

Figure 1.10 – Room-temperature Raman spectra of p-type GaAs nanowires with different doping concentration in cm^{-3} taken in forward scattering configuration with 520.8 nm laser. Reproduced from [34].

1.4.1 Photoluminescence spectroscopy

Another non-destructive technique that gives access to the electronic properties of semiconductors is Photoluminescence spectroscopy. This technique concerns the radiative recombination paths of photoexcited electron-hole pairs. The photoluminescence emission can be affected by many factors such as strain, impurities and charge carriers. The presence of impurities creates states between the band gap, so the presence of them between the band gap could results in emission between those levels. For example, in p-type GaAs doped with Si, Kressel et al. have shown optical transitions between levels within the band gap [35].

The quantum efficiency depends on the relative magnitude of the radiative recombination rate compared to non-radiative recombination rate. In semiconductors, surface or interface states can become a source of non-radiative centers. Non-radiative recombination has a detrimental effect on the optical and electronic properties of semiconductor devices. In nanowire structures, the large surface-to-volume ratio results in the presence of surface traps, offering

easy access to non-radiative carrier recombination. The addition of a passivation $Al_xGa_{1-x}As$ shell around a GaAs nanowires, the emission from the NW increases dramatically [36].

Recently, several groups have studied the photoluminescence emission as a function of the shell thickness and the alloy concentration. Hocevar et al. [37] reported a systematic red shift of the PL peak of $GaAs/Al_{0.35}Ga_{0.65}As$ and of the absorption band edge with increasing shell thickness (Fig. 1.11a,b,c). They have associated a part of such shift to a small tensile strain imposed to the GaAs core by the AlGaAs shell. The blueshift of PL peak as a function of the power suggests that also a piezoelectric field, which develops inside the core due to Al fluctuations in the shell, contributes to the energy shift.

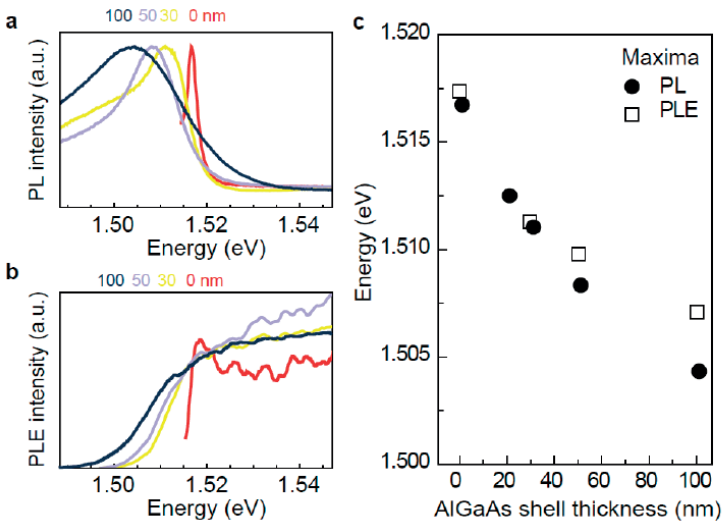

Figure 1.11 – a) PL spectra and b)PLE spectra of nanowire $GaAs/Al_{0.35}Ga_{0.65}As$ ensembles with shell thickness varying from 0 to 100nm. c) Shift of the band edge emission and absorption photon energy versus shell thickness. Reprinted from Ref. [37], with the permission of AIP Publishing.

Moreover, a blue-shift of the PL emission as a function of the power could also be a consequence of a band bending at the core/shell interface due to the existence of impurities in the shell. Increasing the photoexcitation intensity, the large concentration of electrons in the conduction band screens the Coulomb interaction between photoexcited electrons and holes. Therefore a reduction of the binding energy of the exciton occurs. Such an interpretation is given by Dhaka et al. [38], who have studied the PL emission of the core of $GaAs/Al_xGa_{1-x}As$ grown using metal-organic vapor phase epitaxy with Au as catalyst. They reported a red shift with different magnitude in the PL emission of the nanowire core with the increase of the aluminum concentration (x) in the shell, and a blue-shift as a function of the power, saying that the band-bending that induces carriers confinement at the interface is due to Al inhomogeneity and traps.

In a recent work [39], we have observed the same red-shift of GaAs nanomembrane capped with AlGaAs shell. We have shown that this shift originates from oxygen contamination of

aluminum.

1.4.2 TeraHertz spectroscopy

Optical pump-TeraHertz probe spectroscopy is a powerful tool to study charge carrier dynamics in semiconductor nanostructures. In fact, Terahertz spectroscopy allows the characterization of charge carriers not only under steady-state, but also in non-equilibrium conditions. This is possible because the density of the carriers created with an optical pulse can be monitored on a femtosecond time scale. By using such time-resolved TeraHertz spectroscopy setup, Joyce et al. [40] have demonstrated that InP nanowires exhibit a very long photoconductivity lifetime that is weakly dependent on their diameter. On the contrary, it is found [41] that carrier lifetimes in GaAs nanowires are extremely short, because of the high surface recombination rate.

The frequency-dependent conductivity, measured at a fixed delay after excitation, provides information on the carrier properties such as the mobility and carrier densities. The THz response of free carriers is generally described by a Drude model. In addition to the free carriers response, a plasmon response is frequently observed for semiconductors in THz range. Fitting the data with the expression for the complex photoconductivity of a free electron plasma with a surface plasmon resonance, Joyce et al. have found that the mobility of GaAs nanowires is a factor of 6 lower than typical mobilities in bulk GaAs [41].

Boland et al. [42] employed optical-pump TeraHertz probe spectroscopy to measure carrier transport and dynamics at room temperature on modulation Doped nanowires. A Mmdulation doped nanowire is a nanowire with a radial heterostructure, which allows the enhancement of the electron mobility.

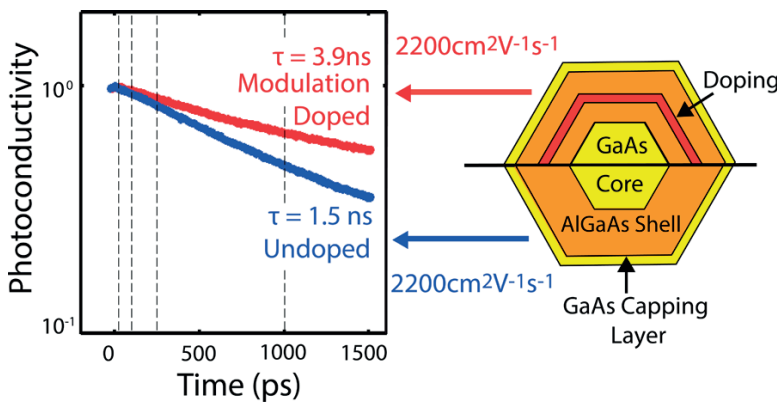

Figure 1.12 – The decay of photoconductivity with time for the modulation doped and undoped reference nanowires as depicted in the left. From Ref. [42], Copyright 2015, American Chemical Society.

Fig. 1.12 shows the decay of photoconductivity with time for the modulation doped and

undoped reference nanowires. The photoconductivity lifetime for modulation doped nanowire structure is found higher than the one of the reference sample. This has been interpreted as an effect of the passivation of interfacial traps by donate electrons. In fact,in modulation doped sample, a high electron concentration should be present at the interface of GaAs/AlGaAs. Part of this electron polpulation has a passivation effect on interfacial traps.

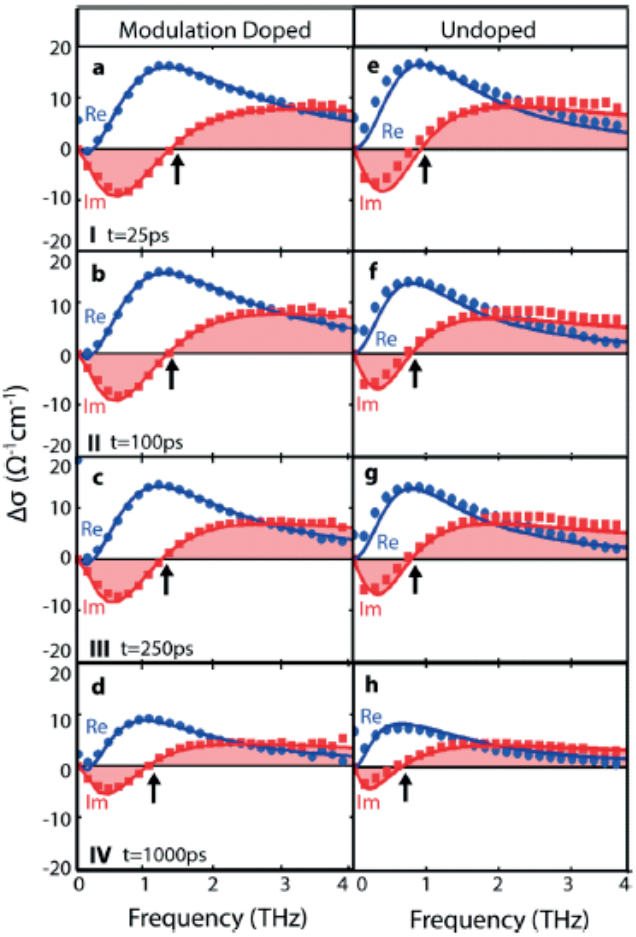

Figure 1.13 – Conductivity spectra for the modulation doped and undoped reference nanowires at different time after photoexcitation. From Ref. [42], Copyright 2015, American Chemical Society.

Fig. 1.13 shows the photoconductivity spectra measured at different time after photoexcitation. From the analysis of the data, the authors found an n-type extrinsic carrier concentration in the order of $\sim 10^{16}$ cm^{-3}. The electron mobility was found dependent on the electron concentration. Boland et al. proposed that carrier-carrier interaction is the main mechanism that governs the mobility in this system.

1.5 Outlook of my thesis

The outline of this thesis is the following:

- **Chapter I**
  Introduction
- **Chapter II**
  In Chap. II the vibrational properties of wurtzite and zincblende and the theoretical basis of Raman scattering are introduced. Moreover, the experimental set-up employed for Raman scattering experiment is described.
- **Chapter III**
  Chapter III is devoted to the study of the effects of resonance modes in nanowires on the Raman spectra, in terms of local probing and selection rules. In the first part, we have investigated the possibility to use photonic modes in Raman scattering to chemically characterize selective areas inside the nanowire. We have performed Raman measurements GaAs/AlGaAs core/shell nanowires with different wavelength excitations. Nanowires with different aluminum contents and different diameter and shell thicknesses are also studied. In the second part, we have studied how it is possible to modify the macroscopic Raman selection rules by changing the photonic environment, i.e. by suspending the nanowire. This method is used to enhance the response of the longitudinal optical and to probe free carrier in GaAs.
- **Chapter VI**
  Chapter VI is devoted to the detection of free carriers by Raman spectroscopy in modulation doping GaAs/AlGaAs core/shell and InAsSb nanowire. We have done a comparison study of the electronic properties of modulation doping GaAs/AlGaAs core/shell nanowire respect to the corresponding non-doped reference. For the InAsSb nanowires, the effects of the content of Antimony, the temperature and the passivation on the electronic properties is presented.
- **Chapter V**
  Chapter V summarizes the results of this thesis

1.6 Papers included in my thesis work

Parts of this thesis have been published in peer-reviewed journals. In Chap. 3, publications are reproduced with permission of the corresponding publisher. I was the principal responsible for the majority of the experimental work as well as data analysis and writing of the manuscript.

- **Probing inhomogeneous composition in core/shell nanowires by Raman spectroscopy.**
  F. Amaduzzi, E. Alarcón-Lladó, E. Russo-Averchi, F. Matteini, M. Heiß, G. Tütüncüoglu,

S. Conesa-Boj, M. de la Mata, J. Arbiol, and A. Fontcuberta i Morral, *Journal of Applied Physics*, page 184303, Volume 116, 2014.

- **Tuning the response of non-allowed Raman modes in GaAs nanowires.**
  Francesca Amaduzzi, Esther Alarcón-Lladó, Hubert Hautmann, Rawa Tanta, Federico Matteini, Gözde Tütüncüoğlu, Tom Vosch, Jesper Nygard, Thomas Jespersen, Emanuele Uccelli and Anna Fontcuberta i Morral, *Journal of Physics D: Applied Physics*, Number 9, Page 095103, Volume 49, 2016

In Chap. 4,the results will be published in a paper currently in preparation.

During my PhD, I also contribute to the following papers, co-authored by me:

- **Polarization response of nanowires à la carte.**
  Alberto Casedei, Esther Alarcón-Lladó, Francesca Amaduzzi, Eleonora Russo-Averchi, Daniel Ruffer, Martin Heiss, Luca Dal Negro and Anna Fontcuberta i Morral, *Scientific Reports*,Page 7651, Volume 5, 2015

- **Modulation Doping of GaAs/AlGaAs Core–Shell Nanowires With Effective Defect Passivation and High Electron Mobility.**
  Jessica L. Boland, Sonia Conesa-Boj, Patrick Parkinson, Gözde Tütüncüoglu, Federico Matteini, Daniel Rüffer, Alberto Casadei, Francesca Amaduzzi, Fauzia Jabeen, Christopher L. Davies, Hannah. J. Joyce, Laura M. Herz, Anna Fontcuberta i Morral and Michael B. Johnston, *NanoLetters*,Page 1336, Volume 15, 2015

- **From Twinning to Pure Zincblende Catalyst-Free InAs(Sb) Nanowires.**
  Heidi Potts, Martin Friedl, Francesca Amaduzzi, Kechao Tang, Gözde Tütüncüoglu, Federico Matteini, Esther Alarcon Lladó, Paul C. McIntyre, and Anna Fontcuberta i Morral *NanoLetters*,Page 637, Volume 16, 2015

- **Morphology and composition of oxidized InAs nanowires studied by combined Raman spectroscopy and transmission electron microscopy.**
  Rawa Tanta, Thomas Kanne, Francesca Amaduzzi, Zhiyu Liao, Morten H Madsen, Esther Alarcón-Lladó, Peter Krogstrup, Erik Johnson, Anna Fontcuberta i Morral, Tom Vosch,J. Nygard and T.S. Jespersen *Nanotechnology*,Page 305704, Volume 27, 2016

- **Revealing Large-Scale Homogeneity and Trace Impurity Sensitivity of GaAs Nanoscale Membranes.**
  Zhuo Yang, Alessandro Surrente, Gözde Tütüncüoglu, Krzysztof Galkowski, Melanie Cazaban-Carrazé, Francesca Amaduzzi, Pierre Leroux, Duncan K. Maude, Anna Fontcuberta i Morral and Paulina Plochocka. *Nano Letters*,Page 2979, Volume 17, 2017

- **Nanoporous silicon tubes: the role of geometry in nanostructure formation and application to light emitting diodes.**
  Jelena Vukajlovic Plestina, Derek, Luca Francaviglia, Heidi Potts, Francesca Amaduzzi,

Mile Ivanda and Anna Fontcuberta i Morral. *Journal of Physics D: Applied Physics*,Accepted Manuscript online 8 May 2017.

2 Raman scattering

When light interacts with a material several processes can occur, as reflection, refraction absorption and scattering. The scattering process can be elastic or inelastic. The elastic scattering is predominant and is called Rayleigh scattering. One type of inelastic scattering was discovered by C.V. Raman, who named the phenomenon.

In the Raman scattering process, the photons are scattered by excitations that can be created (Stokes process) or annihilated (AntiStokes process). Various type of excitations, like phonons and plasmons (charge excitations) presents in a solid can participate in this process. In addition, thanks to its non-destructive nature, Raman spectroscopy is a powerful tool to study the spectrum of elementary excitations of semiconductors.

Raman scattering by phonon provides information on the structural properties of the material, such as composition, phase, and crystal orientation. Moreover, Raman spectroscopy in polar semiconductors can provide information on the carrier concentration and mobility thanks to scattering by plasmons.

This chapter is dedicated to the theory of Raman scattering, and organized as follows. In the first two sections of the chapter, the description of phonons in a zinc-blende and wurtzite structures are introduced, as well as in the alloys. The section three and four are dedicated to present the Raman theory based on classical and quantum mechanical treatments. Then, the Raman selection rules for zinc-blende and wutzite structures are presented in the section five, the surface optical modes in section six. Section seven illustrates the Raman scattering mechanism by plasmons and its coupling with phonons, while the last section of the chapter presents the experimental set-up used in our studies.

2.1 Phonon dispersion in zinc-blende and wurtzite structures

A lattice constituted of N atoms has $3N$ normal modes of oscillation. The energy of a normal mode is quantized in form of phonons. A phonon is a quasiparticle defined by its energy ($\hbar\omega$) and wavevector ($\vec{k}$). The energy and the wavevector are related through the dispersion curve. In a 3 dimensional lattice with N atoms per primitive basis, $3N$ branches exist. Three of these are called acoustic and are characterized by having zero frequency for $\vec{k} = 0$. In contrast, the optical branches are the remaining $3N$-3 branches. They have no zero frequency at $\vec{k} = 0$ and, in fact, atoms within the primitive cell move out of phase, even if the center of mass is fixed.

Phonons are also distinguished in transverse and longitudinal, depending if the vibration is perpendicular or parallel to the propagation direction.

InAs and GaAs presents a cubic phase in bulk material. The cubic phase of these compounds is the zinc-blende structure. Zinc-blende structure with two different atoms, as a primitive basis, presents 3 acoustic mode and 3 optical modes. Despite the high symmetry of the structure, there is no degeneracy at $\vec{k} = 0$. This is due to the additional restoring force, which arises from the ionic displacement in the case of the longitudinal mode.

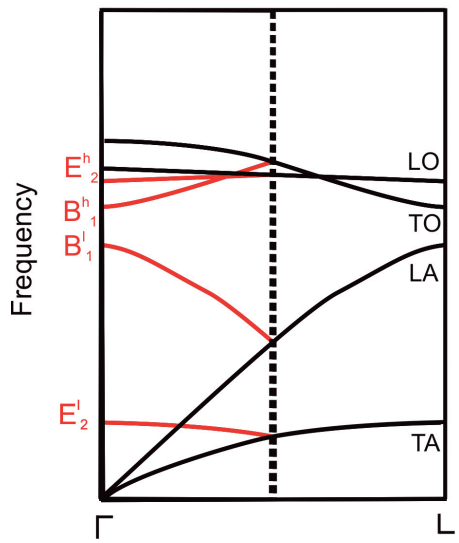

Figure 2.1 – Schematic representation of phonon dispersion of GaAs for zinc-blende and wurtzite phase. The dispersion for the wurtzite phase is obtained by folding the zinc-blende dispersion along $\Gamma \rightarrow L$

In nanowire form, the arsenide III-V compounds can also crystallize in a different crystal phase from bulk, such as the hexagonal wurtzite structure. Wurtzite structures differ from the zinc-blende one for the sequence of stacking of anion-cation planes. Zinc-blende presents an ABCABC sequence along (111) direction, while Wurtzite shows an ABAB stacking sequence in the correspondent (0001) direction. Furthermore, wurtzite structure has four atoms in the primitive cell, which means that nine optical phonons are presents. Using group theory, the optical phonons obtained are A_1, $E_1^{(2)}$, $2E_2^{(2)}$ and $2B_1$ (where (2) means the double degeneracy).

The atomic motion of A_1 and B_1 is along the c axis. Contrarily, the displacement for E_1 and E_2 is orthogonal to it. Group theory predicts whenever a mode is Raman active. Among them, all the modes are Raman active except for B_1, which is called silent because is not active both for Raman and Infrared spectroscopy. The polar character of the A_1 and E_1 phonons lift the degeneracy between the transversal and longitudinal modes.

The additional modes of wurtzite at the Γ point correspond to modes at the L point in zinc-blende. This is because the extent of the Brillouin zone of zinc-blende, along (111) direction, is twice the one of wurtzite along (0001). This allows us to fold the phonon dispersion of zinc-blende along (111) direction, in order to deduce the phonon dispersion of wurtzite along (0001) direction [18]. Fig. 2.1 shows the phonon dispersion of zinc-blende and wurtzite, as a result of the zone folding of the zinc-blende dispersion along $\Gamma \rightarrow L$.

The frequencies of the zone center optical modes of the zinc-blende and wurtzite for GaAs and InAs are listed in table 2.1 and 2.2 respectively. The wurtzite phonon frequencies are estimated from the corresponding modes in zinc-blende at the Γ and L point, taken from Ref. [43] and Ref. [44] for GaAs and InAs, respectively

Table 2.1 – Raman optical phonon modes in wurtzite GaAs estimated from the experimental corresponding modes in zinc-blend at Γ and L point [43].

Structure	Mode	Position (cm^{-1})
zinc-blende	TO	267.7
	LO	291.9
wurtzite	A_1 (TO)	267.7
	A_1 (LO)	291.9
	E_1 (TO)	267.7
	E_1 (LO)	291.9
	${E_2}^h$	261.3
	${E_2}^l$	62.1

Table 2.2 – Raman optical phonon modes in wurtzite InAs estimated from the experimental corresponding modes in zinc-blend at at Γ and L point [44]

Structure	Mode	Position (cm^{-1})
zinc-blende	TO	217.3
	LO	238.6
wurtzite	A_1 (TO)	238.6
	A_1 (LO)	217.3
	E_1 (TO)	226
	E_1 (LO)	238.6
	${E_2}^h$	216
	${E_2}^l$	44

2.2 Phonon modes of ternary alloys

In the framework of this thesis, it is important to introduce the compositional dependence of optical phonons at the Γ point of an alloy. Phonons of alloys show a specific trend. In ternary semiconductors such as $A_xB_{1-x}C$, the optical phonons may exhibit a one-mode or two-mode behavior.

One-mode behavior presents only one set of LO and TO phonons, with frequencies showing an almost linear dependence from one end-member AC to the other BC. On the contrary, two-mode behavior exhibits two sets of LO and TO phonons, whose frequencies vary continuously from those of one end-member binary AC,BC to the impurity mode (Local Vibrational Mode) in the other end-member binary BC:A and AC:B, respectively. The Local Vibrational Mode arise from the presence of an impurity with different mass than the host atoms. and has different frequency than the host's vibrational frequency. The two-mode behavior is typical of alloys in which the atoms occupying equivalent lattice sites have significantly different masses. The REI (Random-Element-Isodisplacement) Model, proposed by Chen et al. [45], explains the two mode behavior of mixed crystal systems. Most of III-V alloy systems show a two mode behavior, as $Al_xGa_{1-x}As$ [46], $GaP_{1-x}As_x$ [47], $Ga_xIn_{1-x}Sb$ [48], $Ga_xIn_{1-x}As$ [49, 50], $InAs_{1-x}Sb_x$ [50].

Fig. 2.2 shows the phonon frequency dependence as a function of the alloy composition for $Al_xGa_{1-x}As$ semiconductor. In the graph, two set of optical modes are observed. The TO and

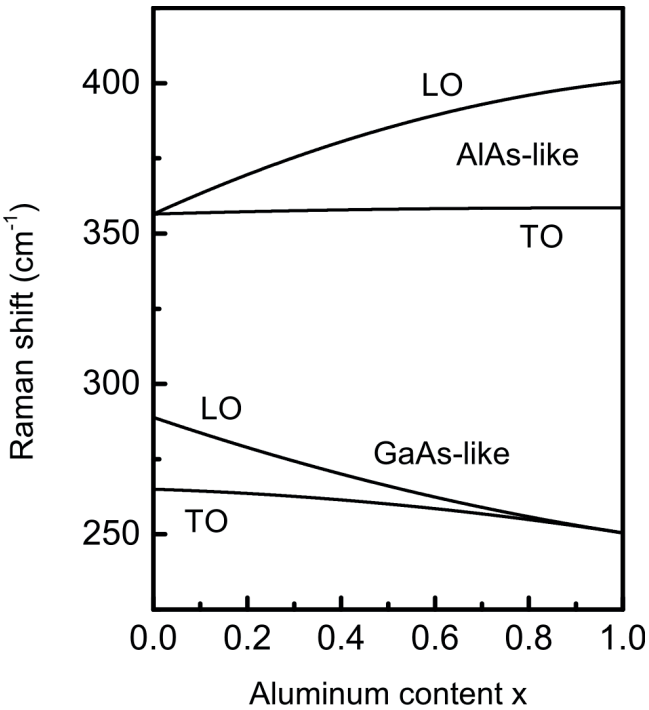

Figure 2.2 – The optical phonon energy of $Al_xGa_{1-x}As$ as a function of the Al content

LO modes close to those of GaAs (AlAs) are called GaAs-like modes (AlAs-like modes). At the end of the compositional range, GaAs-like modes tend to the Local Vibrational mode (LVM) of Ga in AlAs material, inversely the AlAs-like modes to the LVM of Al in a GaAs matrix.

2.3 Macroscopic theory of Raman scattering

From a classical point of view, Raman scattering arises from the polarizability of the material modulated by the vibrations, which causes the radiation of the induced dipole moment at frequencies different from those of the incoming electric field [51]. The electric field $\vec{E}\cos(\vec{k}\cdot\vec{r}-\omega_i\cdot t)$ causes an induced dipole moment $\vec{P}$, which is proportional to the electric field $\vec{E}$ through the susceptibility $\chi(\omega,\vec{k})$ of the crystal. The susceptibility can be expanded as a power series of the atomic normal coordinates:

$$\chi(\omega,\vec{k}) = \chi_0(\omega,\vec{k}) + \frac{\partial\chi(\omega,\vec{k})}{\partial\vec{u}}\vec{u} \tag{2.1}$$

where $\vec{u} = \vec{u}_0\cos(\vec{q}\cdot\vec{r}-\omega_q\cdot t)$ is the atomic displacement. With the expansion of the susceptibility in a Taylor series, the polarizability has the form of the sum of two terms as:

$$\vec{P} = \chi_0(\omega,\vec{k})\vec{E}\cos(\vec{k}\cdot\vec{r}-\omega_i\cdot t)+\frac{\partial\chi(\omega,\vec{k})}{\partial\vec{u}}\frac{\vec{u}_0\vec{E}}{2}(\cos((\vec{k}+\vec{q})\cdot\vec{r}-(\omega_i+\omega_q)\cdot t)+\cos((\vec{k}-\vec{q})\cdot\vec{r}-(\omega_i-\omega_q)\cdot t)) \tag{2.2}$$

The first term of the Eq. 2.2 represents the static polarizability and contributes to the elastic scattering, while the second term takes into account the modulation of the atomic displacement. The polarization resulting from this term oscillates at frequencies that are differents with respect to the incoming one.

In particular, the cosine term containing the difference of the wavevector $((\vec{k}-\vec{q})\cdot\vec{r})$ represents the excitation of a phonon, i.e. the Stokes process, while the cosine term containing the sum of the wavevector $((\vec{k}+\vec{q})\cdot\vec{r})$ represents the AntiStokes process, with the absorption of the excitation. Moreover, the conservation of energy and momentum in the scattering process are contained in the argument of the two cosines terms ($\vec{k_s} = \vec{k}\pm\vec{q}$ and $\omega_s = \omega_i \pm \omega_q$). The conservation of momentum yields the possibility to probe phonons only at Γ point due to the small momenta of the light incident and scattered.

From the radiation emitted by an electric dipole vibrating in time, the intensity of the light scattering in a direction $\hat{e}_s$ is given by [52]:

$$I_s \propto |\hat{e}_s\cdot\frac{\partial\chi(\omega,\vec{k})}{\partial\vec{u}}\cdot\hat{e}_i|^2 < u(q,\omega)u^*(q,\omega) > \tag{2.3}$$

The first term contains the Raman tensor ($\frac{\partial\chi(\omega,\vec{k})}{\partial\vec{u}}$) and is used to derive the Raman selection rules. The second term is called the power spectrum of fluctuations and is calculated with the dissipation-fluctuation theory. It is possible to demonstrate that the power spectrum given for Stokes scattering by phonon is given by:

$$\langle u(q,\omega)u^*(q,\omega)\rangle \propto \frac{\hbar}{2\omega_q}(n(\omega_q)+1)L(\omega_q) \tag{2.4}$$

where $n(\omega_q)$ is the Bose-Einstein distributions and $L(\omega_q)$ is the Lorentzian function.

2.4 Microscopic theory of Raman scattering

Within the quantum treatment, a first order process of scattering (with the excitation or the annihilation of only one phonon) can be described as a three-step process. In fact, as a phonon energy is significantly lower than the energy of photons of the exciting laser, the scattering process happens by a virtual intermediate state that involves electrons. Feynman diagrams in Fig. 2.3 represent the Stokes and the Anti-Stokes processes [53]. In each Feynman diagram the dashed lines stand for the incoming and outgoing photons, while the wavy line represents a phonon with e $\vec{q}$ momentum. The Fermion loop represents the electron-hole pairs, while the black dots and the black squares represented the electron-radiation and electron-phonon interaction, respectively.

In a first step, the photon impinging the crystal excites an electron from a ground state to a first intermediate state $|a\rangle$. The second step involves a transition from the first electron intermediate state $|a\rangle$ to another state $|b\rangle$. As a consequence of this transition, a phonon is created or annihilated. In the third step, a transition to the electron ground state leads the emission of a photon. After the whole process, the electron state remains unchanged. By using the time dependent perturbation theory, the Raman scattering probability may be calculated as:

$$P_{fi} = \frac{2\pi}{\hbar}\,|\sum_{a.b}\frac{\langle f|H_{e-R}|b\rangle\langle b|H_{e-ph}|a\rangle\langle a|H_{e-R}|i\rangle}{(\hbar\omega_i-(E_a-E_i))(\hbar\omega_f-(E_b-E_i))}|^2\,\delta(\hbar\omega_i-\hbar\omega_s-\hbar\omega_{ph}) \tag{2.5}$$

where $|i\rangle$ and $|f\rangle$ are the initial and the final state, while H_{e-R} and H_{e-ph} represent the electron-radiation and the electron-phonon Hamiltonian interactions.

Within the dipole approximation, the Hamiltonian representing the electron-radiation interaction is given by:

$$H_{e-R} = \frac{e}{mc}\vec{A}\cdot\vec{p} \tag{2.6}$$

where $\vec{p}$ is the momentum operator and $\vec{A}$ is the vector potential of the electromagnetic field.

In a polar semiconductor, we have to consider two types of electron-lattice interaction [54].

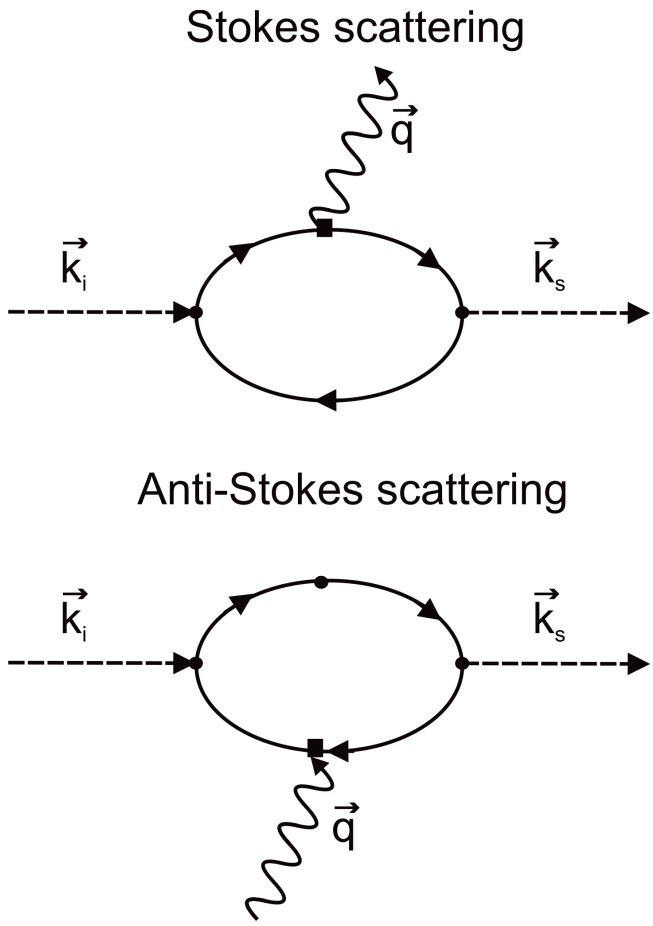

Figure 2.3 – Feynman diagram representing the first order Raman process.

The first one, called Deformation potential, is due to the effect that the relative ionic displacement of phonons causes on the electronic energies. In fact the electronic energy will change with the bond lengths and angles of atoms. In the case of crystal vibration, the interatomic distance varies and the electronic energies are modulated. Due to its nature, it is a short-range interaction. In fact electrons does not feel any long-range polar field, but only the modulation of the ionic distance. Since is electronic energy are connected to the dielectric function and then to the susceptibility, considering only the deformation potential, Eq. 2.5 and 2.3 are equivalent.

For polar material, a second effect should be taken into account. In fact longitudinal optical phonon cause a long-range dipole field with electrons interact. This effect is described by the Frölich interaction and has two components: the allowed and the forbidden mechanisms. The attribute allowed of forbidden are assigned whenever the mechanism has the same symmetry or not of than that of the deformational potential. The allowed mechanism is $\vec{q}$ independent interband scattering, involving states in different bands. It is characterized by the electro-optic tensor, which has the same symmetry as the corresponding to deformation potential. This mechanism gives the difference between the intensity of the TO and LO modes. The relative

strength between the deformation potential and the electro optic interaction connected by the ratio between TO and LO intensities is given by the Faust Henry coefficient. Contrarily, the forbidden term is due to the intraband scattering and has a vanishing contribution far from the resonance condition (i.e. energies of photon close to the a transition ones.) In fact close to the resonant condition, Raman scattering is dominated by the forbidden mechanism. The contribution of the forbidden scattering to the Raman tensors is represented by a diagonal matrix.

2.5 Raman selection rules in zinc-blende and wurtzite structures

As stated in Eq. 2.3, by knowing the scattering geometry and the Raman tensor, the Raman selection rules can be obtained. The scattering geometry is often indicated by using the Porto notation. In this notation the directions wavevectors $\hat{k}_i$ and $\hat{k}_s$, and the polarizations $\hat{e}_i$ and $\hat{e}_s$ of light incident and scattered, are specified with respect to an orthogonal system as: $\hat{k}_i(\hat{e}_i\hat{e}_s)\hat{k}_s$. The Raman tensor ($R = \frac{\partial\chi(\omega,\vec{k})}{\partial\vec{u}}$) depends on the crystal symmetry.

For a zinc-blende GaAs structures, the Raman tensors for deformation potential and allowed scattering mechanisms, are usually given in the base $\hat{e_1} = (1,0,0)$, $\hat{e_2} = (0,1,0)$ and $\hat{e_3} = (0,0,1)$ by [51]:

$$\mathbf{R}_{\hat{e_1}} = \begin{pmatrix} 0 & 0 & 0 \\ 0 & 0 & a \\ 0 & a & 0 \end{pmatrix} \qquad \mathbf{R}_{\hat{e_2}} = \begin{pmatrix} 0 & 0 & a \\ 0 & 0 & 0 \\ a & 0 & 0 \end{pmatrix} \qquad \mathbf{R}_{\hat{e_3}} = \begin{pmatrix} 0 & a & 0 \\ a & 0 & 0 \\ 0 & 0 & 0 \end{pmatrix} \tag{2.7}$$

Each Raman tensor corresponds to an oscillation polarized along the respective directions. Considering the geometry of the nanowires, it is convenient to transform the Raman tensor into the basis of the relevant crystallographic axis, which correspond to the directions x=(1,-1,0), y=(1,1,-2) and z=(1,1,1).

Meanwhile in wurtzite structure, choosing x,y, and z as the high symmetry axis of the structures, (c-axis as z=(0,0,0,1) and x=(1,-1,0,0) and y=(1,1,-2,0) in the hexagonal plane) the Raman tensor can be expressed as:

$$\mathbf{R}_x^{E_1} = \begin{pmatrix} 0 & 0 & 0 \\ 0 & 0 & c \\ 0 & c & 0 \end{pmatrix} \qquad \mathbf{R}_y^{E_1} = \begin{pmatrix} 0 & 0 & -c \\ 0 & 0 & 0 \\ -c & 0 & 0 \end{pmatrix} \qquad \mathbf{R}_z^{A_1} = \begin{pmatrix} a & 0 & 0 \\ 0 & a & 0 \\ 0 & 0 & b \end{pmatrix} \tag{2.8}$$

Table 2.3 – Selection rules for zinc-blende and wurtzite structures in backscattering. $x(i,j)\bar{x}$ and $z(i,j)\bar{z}$ configuration corresponds to a backscattering configuration for a nanowires lying down or standing on a substrate

Configuration	zinc-blende	wurtzite
$z(y,y)\bar{z}$	TO, LO	E_2, A_1 (LO)
$z(y,x)\bar{z}$	TO	E_2
$x(y,y)\bar{x}$	TO	E_2, A_1 (TO)
$x(y,z)\bar{x}$	TO	E_1 (TO)

$$\mathbf{R}_x^{E_2} = \begin{pmatrix} d & 0 & 0 \\ 0 & -d & 0 \\ 0 & 0 & 0 \end{pmatrix} \qquad \mathbf{R}_z^{E_2} = \begin{pmatrix} 0 & d & 0 \\ -d & 0 & 0 \\ 0 & 0 & 0 \end{pmatrix} \tag{2.9}$$

Table 2.3 summarizes which modes are allowed or not, in different conditions for a backscattering configuration of a nanowires lying down or standing on a substrate. Both the cases are schematically represented in Fig. 2.4.

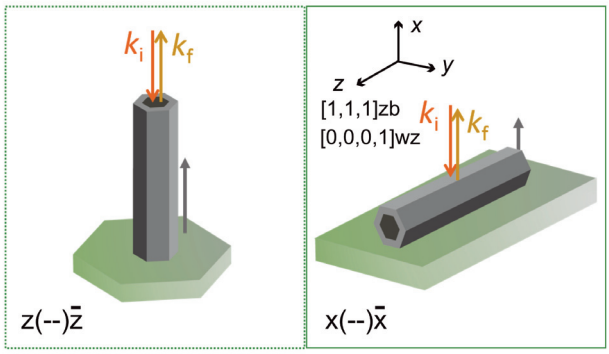

Figure 2.4 – Schematic representation of the backscattering configuration for a nanowire standing on a substrate or lying down

2.6 Surface optical modes

The finite size of an object plays a key role on the Raman scattering. In fact, by reducing the size of the structures, bulk modes can change their position because of the phonon confinement effect. Moreover, new modes can appear such as the surface optical modes. The surface optical phonons are generated at the interface between different materials, for example at the

air-semiconductor interface.

In nanowires, the presence of a peak with a frequency between TO and LO modes, associated to the Surface Optical mode is often observed. The position of the Surface Optical mode depends on the dielectric constant of the surrounding medium and the diameter of the nanowire.

Using the approximation of an infinitely long cylinder, the position of Surface Optical phonon can be predicted by using the following equation: [22]

$$\epsilon(\omega) + \epsilon_m f(qr) = 0 \tag{2.10}$$

where $f(qr)$ is given by:

$$f(qr) = \frac{I_0(qr)K_1(qr)}{I_1(qr)K_1(qr)} \tag{2.11}$$

where q is the phonon wavevector, r the nanowire radius and $I_i(qr)$ and $K_i(qr)$ the modified Bessel functions. For a finite long cylinder, the frequency of the Surface Optical phonon ω_s is represented by:

$$\omega_s^2 = \omega_s^2 + \frac{\omega_p^2}{\epsilon_\infty + \epsilon_\infty f(qr)} \tag{2.12}$$

where ω_p is the screened ion plasma frequency $\omega_p^2 = \epsilon_\infty(\omega_{LO}^2 - \omega_{TO}^2)$ and ϵ_∞ the high frequency dielectric function of the material.

Fig. 2.5 shows the dispersion of the SO modes. We can observe that the position of the SO mode depends on the external medium and on the size of the wire [22, 55, 21].

2.7 Raman scattering by LO phonon-plasmon coupled modes

During the Raman scattering process, light can be scattered by free carriers present in semiconductor that can be created via doping or thermal and optical excitations. Collective excitations, such as charge-density excitation usually referred as plasmons, and single-particle excitations can be observed [56, 57, 58, 59]. Plasma excitations can interact with the macroscopic longitudinal electric field of LO polar phonons, giving rise to the LO phonon-plasmon coupled modes (LOPPCM). The first observation of LOPPCM was reported by Mooridian and Wright in n-type GaAs [31]. Thanks to the scattering by LOPPCM, Raman spectroscopy can be used as a contact-less tool to probe carrier concentrations as well as their mobilities.

We proceed now to the explication of the plasmon modes. In semiconductors, electrons located in the conduction band can be represented by an electron gas in a solid, formed by fixed and opposite positive charge of the ion core. If it is displaced with respect to their

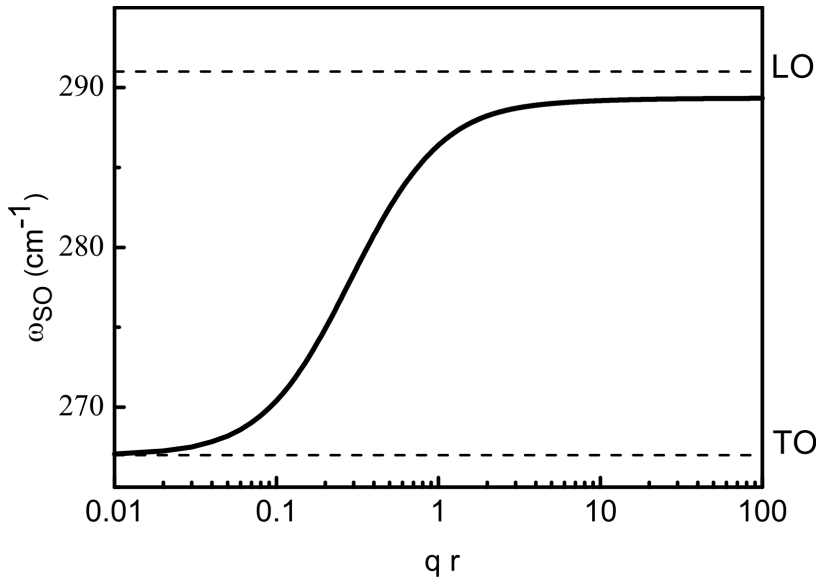

Figure 2.5 – Calculated position of the SO mode for GaAs nanowire embedded in air.

equilibrium position, the electron gas oscillates with a natural frequency, given by:

$$\omega_p^2 = \frac{4\pi}{\epsilon_\infty}\frac{N_0 e^2}{m^*} \tag{2.13}$$

withN_0 the free-electron concentrations. Throughout this thesis, we will use the cgs units, because they are most-often used in the literature.

Since this oscillation is longitudinal, as it is the case for the LO phonon modes in polar semiconductors, the LO mode interacts with the macroscopic electric field of the plasmon. The position of the resulting coupled modes can be obtained from the zero of the dielectric function according to the Maxwell‘s equations for a longitudinal waves. Then, the dielectric function, which includes both the lattice and the carriers contribution, has the form:

$$\epsilon(\omega) = \epsilon_\infty + 4\pi(\chi_I(\omega) + \chi_e(\omega)) \tag{2.14}$$

with the ionic $\chi_I(\omega)$ and free carrier $\chi_e(\omega)$ susceptibility.

As for the undoped semiconductors, the Raman line shape can be evaluated using the dissipation fluctuation theorem. With the presence of carriers in the formalism of Hon and Faust, the Raman cross-section by coupled modes assumes the form:

$$\frac{\partial^2\sigma}{\partial\omega\partial\Omega} \propto (n(\omega)+1)I[\frac{1}{\epsilon(\omega)}[\frac{\epsilon_\infty}{4\pi} + 2A\chi_I(\omega) - A^2\chi_I(\omega)(1+\frac{4\pi}{\epsilon_\infty}\chi_e(\omega))]] \tag{2.15}$$

where $n(\omega)$ is the Bose-Einstein distribution of phonons, A is defined as $A = \omega_{TO}^2 C/(\omega_{LO}^2 - \omega_{TO}^2)$ with C being the Faust-Henry coefficient, and ω_{TO}^2 and ω_{LO}^2 are the frequencies of TO and LO

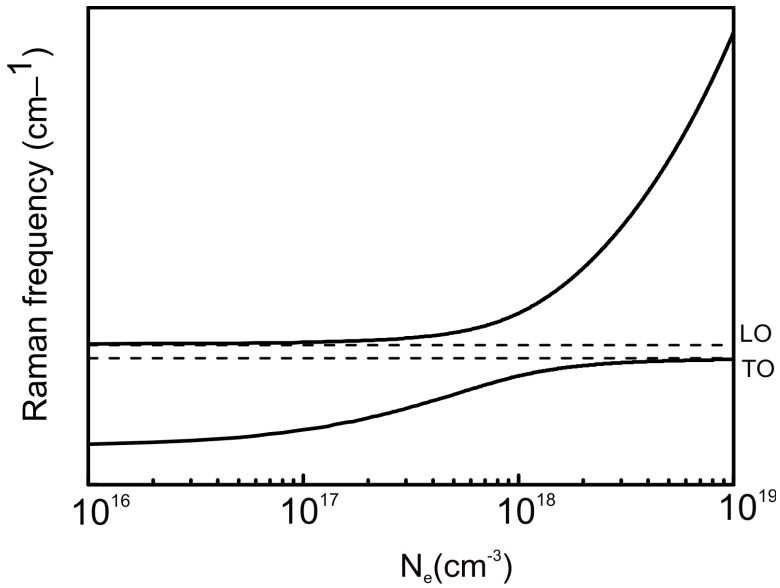

Figure 2.6 – Frequency position of the coupled modes obtained from the zeros of the dielectric permettivity.

modes respectively.

The ionic contribution to the susceptibility is given by:

$$\chi_I(\omega) = \frac{\epsilon_\infty}{4\pi} \frac{\omega_{LO}^2 - \omega_{TO}^2}{\omega_{TO}^2 - \omega^2 - i\omega\Gamma_i} \tag{2.16}$$

with Γ_i the phonon damping constant.

For the calculation of the electronic susceptibility, we consider the Drude and the Hydrodynamical model, both within a classical treatment. The Drude model is the simplest model one can use, which does not take into account the effects of the temperature, of the dispersion of the conduction band and of the wavevector of the plasmon.

Solving the dynamical equation of electrons, the electronic susceptibility derived by the Drude model is:

$$\chi_e(\omega) = -\frac{\epsilon_\infty}{4\pi} \frac{\omega_p^2}{\omega^2 - i\omega\Gamma_p} \tag{2.17}$$

where ω_p is the plasma frequency and Γ_e is the damping constant related to the mobility of the plasmon.

Neglecting the ionic and the electronic damping constant, it is possible to obtain the frequency of the coupled mode, L^+ andL^- from the zeros of the dielectric permittivity.

Fig. 2.6 shows the dependence of the frequency position of the coupled modes in function

of the carrier concentration. We can observe that at low carrier concentration regime, the L^- follows the position of the plasmon mode and L^+ is at the position of the LO mode. On the contrary, for high carrier concentration, the frequency of the L^+ becomes closer to the plasmon mode and the frequency of the L^- tends to the position of TO mode. The high concentration of carrier screens the extra Coulomb force induced by the LO longitudinal field.

When the temperature effect and the wavevector dependence should be considered, Hydrodynamical model can be used [60]. This model introduce an extra term in the dynamical equation of electrons $(-(1/N_e)\vec{\nabla}P)$, related to the pressure P of the electron gas. The pressure of the electron gas is defined as the sum of the forces of all electrons striking the wall of the solid per unit area. According to the kinetic theory, the pressure can be expressed as $P = -(1/3)N_e m^* < v^2 >$ where$< v^2 >$ is the electron mean square velocity. This gives as a results the following expression for the electronic susceptibility:

$$\chi_e = -\frac{\epsilon_\infty}{4\pi}\frac{\omega_p^2}{\omega^2 - < v^2 > q + i\omega\Gamma_e} \tag{2.18}$$

The electron mean square velocity can be calculated knowing the band energy dispersion with:

$$< v^2 > = -\frac{1}{\hbar N_e}\int_0^\infty (\frac{\partial E}{\partial k})^2 n_{FD} g(E) dE \tag{2.19}$$

where n_{FD} is the Fermi Dirac distribution, and $g(E)$ is the density of states.

The coupled-mode with their dispersion are well defined by Hydrodynamical model in the regime in which Landau damping is negligible. Landau damping occurs when the phase velocity of the electromagnetic wave is closed to the velocity of the electrons in a plasma. The Lindhard-Mermin model, which is based on a quantum approach, interprets successfully coupled modes at all wavevectors [61].

2.8 Raman spectroscopy set-up

Raman spectroscopy is the main experimental technique used in this thesis. The scheme of the experimental set-up used to carry out all the Raman measurements of this thesis is shown in Fig. 2.7. All the components are placed on an optical table with pneumatic legs.

The light source is produced by an Argon-Krypton laser. This allows to provide several characteristics spectral lines in the visible range. To avoid the plasma background, the laser light is spectrally filtered with a grating and a subsequent aperture. A series of various optical devices are presents in order to control the light polarization. Among them, a polarizer, a quarter-waveplate $\lambda/4$ (to generate a circularly polarized light) and half-waveplate $\lambda/2$ (to rotate the polarization) are used.

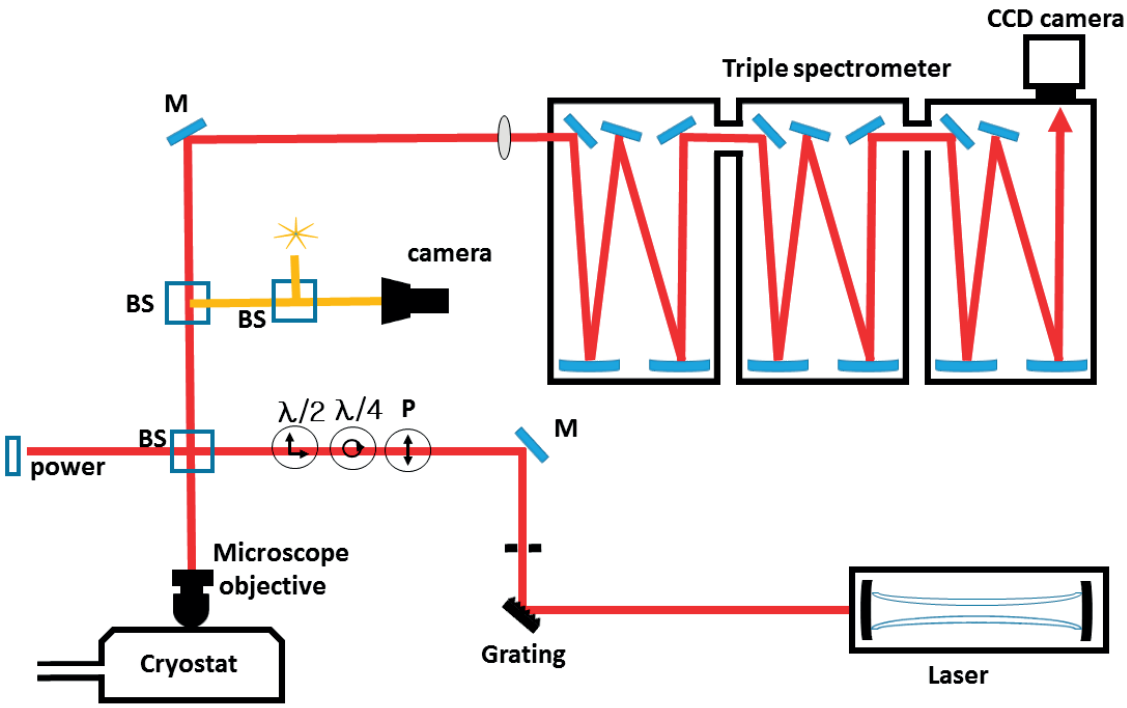

Figure 2.7 – Raman setup.

A beam splitter is applied to split the light in a reflected part and a transmitted part. In order to control the power of the light sent to the sample, the transmitted light is monitored by a power meter. The reflected light is focused on the sample by an objective lens of 0.75 N.A. (Numerical Aperture). The spot size is determined by the diffraction limit, according to the relation $d = (1.22 \cdot \lambda)/N.A.$, where d is the spot's diameter. The objective lens is mounted on a piezo-scanner controlled by a LabView routine, which allows to scan the surface with a precision of 2 nm. To carry out measurements at different temperatures, within the range 4.2 K - 300 K, the sample is placed inside a temperature-controlled liquid helium cryostat. This cryostat system consists in a window assess open circuit cryostat. The sample is cooled by adirect contact with Helium vapour provided by an external dewar and the temperature is measured by a resistor mounted close to the sample.

The same objective lens is used to collect the scattered light, which is collected by the Trivista 555 triple spectrometer. Inside the spectrometer, a set of three grating is used for the dispersion of the light. Different grating periods from 900 to 1800 l/mm can be choose for different applications. Trivista 555 triple spectrometer can operate in an addictive or subtractive configuration. In additive mode, gratings on all 3 stages contribute to disperse light. This mode gives high spectral resolution. In subtractive mode, the first grating is used to disperse light and the second one to recombine the dispersed light. Between them, the slit cut out a desirable portion of spectrum.This allowed to block the wavelengths close to the laser line inside the first spectrometer. In this context, we used only the subtractive configuration, with

the first two gratings employed in an opposite mode. The light, dispersed again by the third grating, is then collected by a charge coupled device detector which is cryogenically cooled with liquid nitrogen.

3 The role of Photonic modes in nanowires in Raman scattering

The high shape anisotropy and the small dimensions of nanowires impact the interaction of nanowire with light. Arising from these features, the differences in the optical properties of nanowires structures and bulk material have fascinated the scientific community, which is studying their fundamental aspects. The spectral dependence of light absorption on the nanowire diameter is one of them. It presents some peaks at certain wavelengths, related to the photonic interaction.

The aim of this chapter is to investigate how the photonic properties of the nanowires affect Raman spectroscopy measurements. In particular, we will outline how the way light gets trapped and/or propagates through the nanowire structure affects the excitation of different parts and/or the macroscopic selection rules.

The results presented in the following sections have been published in peer-reviewed journals.

3.1 Introduction

Raman scattering in nanowires has shown some differences with respect to the bulk or thin films [62]. Raman scattering signal in bulk material is subjected to certain selection rules, which depend on the light direction and polarization of the incoming and scattered light, as well as the symmetry of the vibrational mode. The bulk Raman selection rules in nanowires are masked due to the photonic properties of nanowires [63]. Cao et al. [24] have demonstrated a strong enhancement of the spontaneous Raman scattering from individual Silicon nanowires as a function of the diameter, excitation wavelength and incident polarization state.

Moreover, despite the light absorption as a function of the wavelength has a smooth trend in bulk material, it has been observed the presence of peaks at certain wavelength in nanowire structure. The position of these peaks also depends on the nanowire diameter. Fig. 3.1 shows the measured spectra of the absorption efficiency for individual Ge nanowires having different diameters (Brongersma Group). The spectra were obtained through the measurement of the photocurrent.

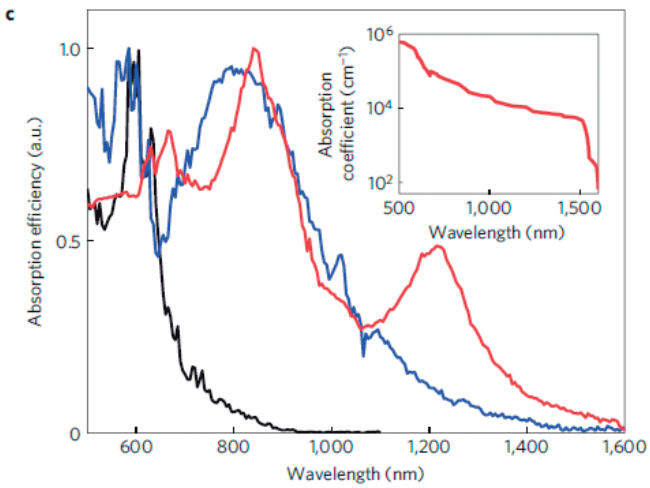

Figure 3.1 – Measured spectra of the absorption efficiency of individual Ge nanowires having different diameters. Reprinted by permission from Macmillan Publishers Ltd: Nature Materials (Ref. [64]), Copyright 2009

These results were explained by computing how light interacts with nanowires. In fact, due to the high-refractive-index of III-V semiconductors, nanowires may form a cavity in which light can circulate by multiple total internal reflections from the boundaries. As a back of the envelope calculation, a "resonance" occurs when the path length covered by the light is any multiple of the half wavelength. For the wavelengths where a photonic mode can be coupled and exist inside the nanowire, absorption is largely enhanced.

In 1908, Mie [65] developed a theory to explain the absorption and the scattering of light by particles with dimension comparable to the incident wavelength. Following Mie theory, it is possible to calculate analytically the absorption for an infinite cylinder, surrounded by

an homogeneous medium, with a light incident perpendicularly to the nanowire axis. The starting point of the model is the solution for the internal field at the exciting frequency in the nanowire. This is obtained by solving Maxwell's equations and by applying the appropriate boundary conditions in cylindrical polar coordinates.

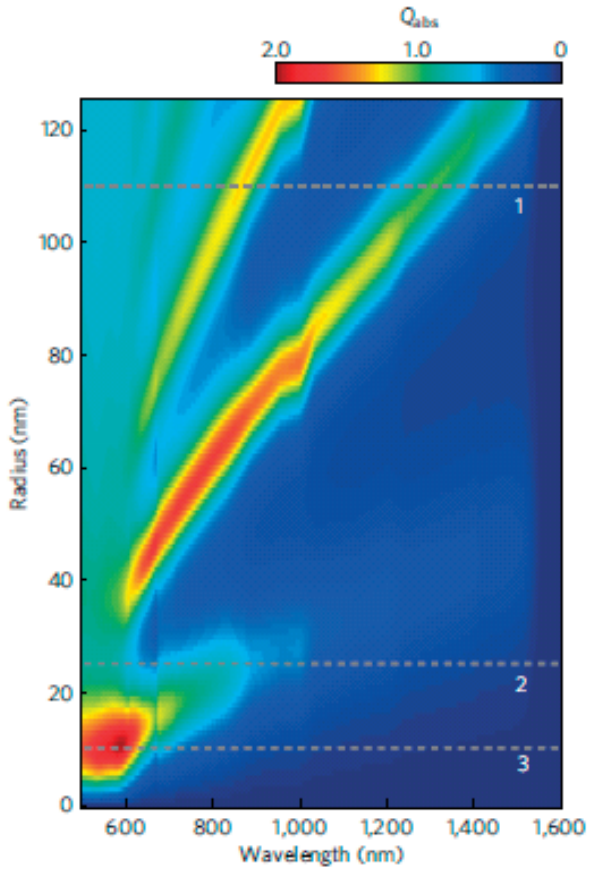

Figure 3.2 – Calculated absorption efficiency as a function of wavelength and radius of a Ge nanowire, for a planar wave directed perpendicularly to the nanowire axis. Reprinted by permission from Macmillan Publishers Ltd: Nature Materials (Ref. [64]), Copyright 2009

Fig. 3.2 shows the two-dimensional plot of calculated absorption efficiency as a function of wavelength and radius of the nanowire. The visible branches represent the resonance modes. We can observe that the increase of the diameter leads to an increase of the wavelength at which the resonance occurs. Moreover, we remark that the observed peaks in the absorption arise from different resonant modes at the same wavelength. Good agreement between the calculated and the measured absorption efficiency was found. The diameter dependence has been studied by J.Lopez et al. [66]. They have performed Raman scattering measurements along the length of a tapered Silicon nanowire. To validate the experimental results, they also performed Finite-Time Difference Domain simulation of a cylindrical nanowire on a substrate. Indeed, to consider the effect of the substrate, numerical calculations are required, as Mie theory is not valid anymore.

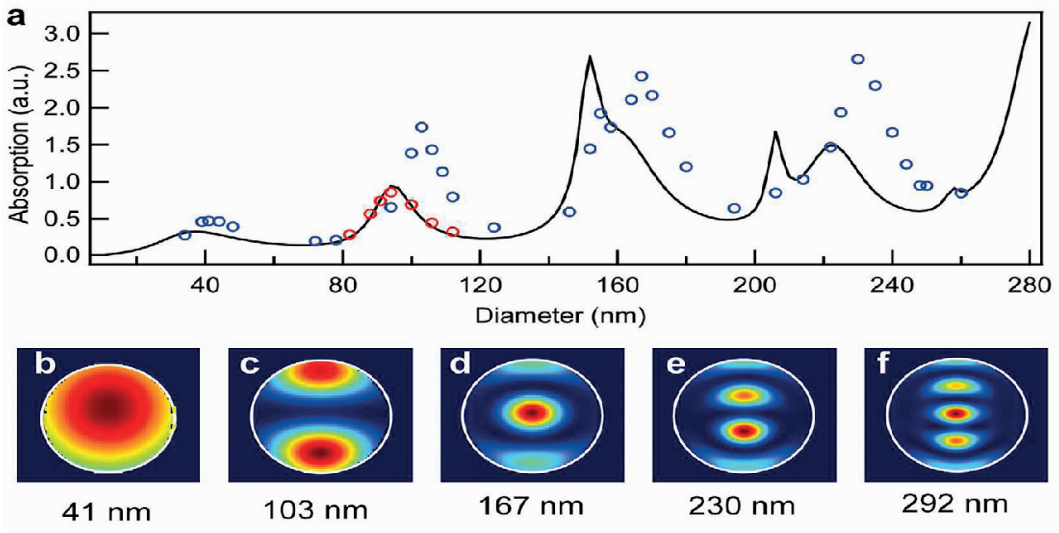

Figure 3.3 – The diameter dependence of the analytical solution (black line) and Finite Difference Time Domain simulation for cylinder with (red circle) and without the Au substrate (blue circle). Reprinted with permission from Ref.[66]. Copyright 2012, American Chemical Society.

The Fig. 3.3 shows the diameter dependence of the analytical solution (black line) and Finite Difference Time Domain simulation for cylinder with (red circle), and without the Au substrate (blue circle). The presence of the substrate shift the position of the peaks toward longer wavelengths. The cross-sectional maps of calculated electric field intensity squared for different diameters are shown in Fig. 3.3b-f. We remark that by increasing the diameter, the presence of photonic modes with higher order are observed.

Lopez et al. [66] performed measurements at different scattering geometries and compared the experimental data with the calculated Raman intensities. Raman intensities were calculated by using the internal field components at the excitation frequency inside the nanowire, as obtained from the simulation. A good agreement with experiments was found for three of the four configurations studied. Their results suggest that not only the light is locally enhanced inside the nanowire, but also, the local field might have a very different polarization with respect to the macroscopic incoming field, resulting into a Raman signal strongly dependent on NW diameter and excitation wavelength. Effectively, this leads a breakdown of the macroscopic selection rules in bulk material.

In this thesis, we have studied the effect of the photonic properties of nanowires on the Raman spectra, focusing on the local probing and change of the macroscopic Raman selection rules. We have shown the possibility to use these photonic modes in Raman scattering to chemically characterize selective areas inside the nanowire, by performing Raman measurements on nanowire core-shell GaAs/$Al_xGa_{1-x}As$ with different wavelength excitations. The results are reported in the first paper reproduced in this Chapter.

A second paper is devoted to the study of the effects of the change of the local field with respect to the incident field, on the macroscopic Raman selection rules. The dependence of these effects on the environment is used to enhance the longitudinal optical phonon of GaAs nanowires. This mode can be used for the characterization of the density and mobility of free carriers.

3.2 Probing inhomogeneous composition in core/shell nanowires by Raman spectroscopy.

F. Amaduzzi, E. Alarcón-Lladó, E. Russo-Averchi, F. Matteini, M. Heiß, G. Tütüncüoglu, S. Conesa-Boj, M. de la Mata, J. Arbiol, and A. Fontcuberta i Morral

Reproduced by permission of the of AIP Publishing. The paper was reformatted for uniformity and the references integrated into the thesis bibliography, but otherwise the content remains unchanged.

3.2.1 Abstract

Due to its non-destructive and its micro-spatial resolution, Raman spectroscopy is a powerful tool for a rapid structural and compositional characterization of nanoscale materials. Here, by combining the compositional dependence of the Raman peaks with the existence of photonic modes in the nanowires, we address the composition inhomogeneities of $Al_xGa_{1-x}As/GaAs$ core/shell structures. The experimental results are validated with complementary chemical composition maps of the nanowire cross-sections and Finite-Difference Time-Domain simulations of the photonic modes.

3.2.2 Introduction

Semiconductor nanowires are filamentary crystals with a tailored diameter between few and few hundred nanometers. Thanks to their geometry, they have inspired new avenues in a large variety of applications [67, 10, 68, 69, 70, 71, 72, 73, 74, 75]. In principle, nearly any material can be synthetized in a bottom-up manner in the nanowire form following the vapor-liquid-solid mechanism or similar [76, 19, 77, 78, 79, 17]. Nanowire-based structures can be further sophisticated by producing heterostructures in the axial, radial and branched directions [80, 81, 82, 83, 84, 85, 86, 87]. One of the most interesting challenges in the synthesis of nanowires is the fabrication of ternary and quaternary alloys. Being the surface-to-volume ratio enhanced, capillary forces, adatom diffusivities and surface energies amplify alloy segregation processes [88, 89]. The composition control at the atomic and nanoscale of ternary and quaternary materials in the form of nanowire has not yet reached maturity. In order for this area to progress, techniques that enable a fast and accurate assessment of the composition and its homogeneity are needed. Extremely precise but yet costly techniques such as atom probe tomography provide three dimensional information on the nanowire composition down to 0.01 % [90]. Less costly techniques include high resolution EELS (Electron Energy Loss Spectroscopy) and EDX (Energy Dispersive X-Ray Spectroscopy) in a transmission electron microscopy. One inconvenience of these techniques is that they destroy the specimen and probe only a small fraction of it. An alternative non-destructive technique which allow multiple nanowire sampling in a fast manner is the measurement of the phonon spectra by Raman spectroscopy [91, 92, 26].

The optical phonons in a ternary $Al_xGa_{1-x}As$ alloy exhibit a two-mode behavior. Two sets of longitudinal optical (LO) and transversal optical (TO) phonons are observed. Their frequencies vary continuously from those of GaAs(AlAs) to the impurity mode in the other end-member binary AlAs(GaAs), respectively. The random-element-isodisplacement model proposed by Chen et al. [45] explains this two mode behavior. Parayanthal et al. [91] used it to characterize both the epitaxial layer and the interface of $Al_xGa_{1-x}As/GaAs$ heterojunctions, to obtain information on Al composition of $Al_xGa_{1-x}As/GaAs$ from the frequency position of the phonon peaks. In this way Raman frequencies of phonon modes can be used to monitor the composition in a complicated multilayer structure, and that the relative Raman intensities can be related to variations in composition [93].

Raman spectroscopy has also recently been used for the characterization of crystal phase and chemical composition of III-V nanowires. [18, 26, 94, 95]. Due to the one-dimensional geometry of the nanowire and the dielectric mismatch with the surrounding medium, the bulk Raman selection rules are slightly modified leading to a strong dependence on the polarization angle between the incident electric field and the nanowire axis [63]. In particular, the intensity of the scattered mode is higher for incident and scattered light with polarization parallel to the nanowire axis. This effect is often called *antenna effect* [96]. It is also observed in absorption and luminescence studies [97, 98, 99]. Recently, resonant photonic effects leading to increased absorption have been demonstrated in nanowires [64, 10, 100]. These optical resonances in nanowires have shown to play an important role in the non-linear optical properties of nanowires, such as Raman scattering and second harmonic generation [24, 66, 101, 102, 103]. As an example, Cao et al. [24] have demonstrated a strong enhancement of the spontaneous Raman scattering from individual silicon nanowires, which depends in a very strong manner on the diameter, excitation wavelength and incident polarization.

In this work we investigate the use of Raman spectroscopy to determine the chemical composition of $GaAs/Al_xGa_{1-x}As$ core/shell nanowires. As a consequence of the wavelength dependence of photonic modes, incident light probes different regions of the structure in a non-intuitive manner and Raman spectra strongly depend on the excitation wavelength. This demonstrates the importance of theoretical simulations on the distribution of the electromagnetic field inside the nanowires for the understanding of Raman spectroscopy experiments on nanowires.

3.2.3 Experiment

The $GaAs/Al_xGa_{1-x}As$ nanowire core/shell structures were grown by molecular beam epitaxy in a DCA P600 MBE machine on a 2-inch Si (111) substrate. The core was obtained by the Gallium-assisted method as reported in Ref. [104, 105]. After stopping the axial growth, the conditions were switched from axial to radial growth in order to obtain an $Al_xGa_{1-x}As$ shell with different thickness and nominal Al composition of x=25%, 50% and 70%, as described in Ref. [106, 89]. The $Al_xGa_{1-x}As$ shell was capped with 5nm of GaAs to prevent oxidation upon

exposure to air. The exact growth protocol is reported in the Appendix A.

Compositional mappings of the nanowires were performed on cross-sections prepared by microtomy [107, 88]. The structure and composition was characterized by combining high-angle annular dark field scanning transmission electron microscopy (STEM) and Energy Dispersive X-Ray Spectroscopy (EDS or EDX) in Figure 3.4. From the different contrast we can distinguish between the GaAs regions (lighter contrast) and $Al_xGa_{1-x}As$ regions (darker contrast). In the rightmost image, the contrast is not uniform because the cross-section lamella was thinner than for the other samples. The embedding resin in the thinner lamellas are more susceptible to beam-induced heating.Heating of the resin can result in slight tilting of the sample and thus a distorted contrast due to additional backscattering. The nanowires exhibit a hexagonal cross-section with side facets pertaining to the {110} family. Al inhomogeneities are deduced from the presence of dark stripes at the corners. This has been previously observed and reported in other works [89, 88, 108].

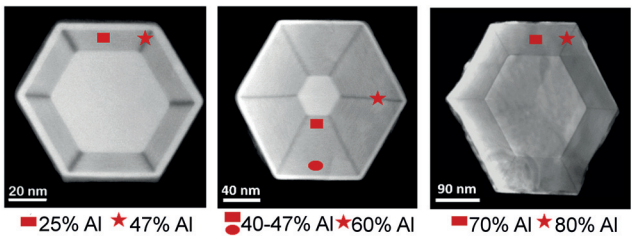

Figure 3.4 – High-angle annular dark field STEM micrographs of GaAs/$Al_xGa_{1-x}As$ core/shell nanowires in cross-section. From left to right, x = 25%, 50% and 70%. The darkest regions near the edges correspond to Al-rich areas. In each of the images, we indicate the Al content in some representative regions as determined using energy-dispersive X-ray spectroscopy (EDX).

The Raman scattering measurements were performed on single nanowires at room temperature. The 488.0, 520.8 and 647.1 nm lines of an Ar-Kr^+laser were used as excitation. The laser light incident with a power of ≈ 300 μW was focused on the nanowire with a microscope objective with numerical aperture $NA = 0.75$. The scattered light was analyzed by a TriVista triple spectrometer and detected by a liquid nitrogen cooled multichannel charge-coupled-device (CCD) detector. The nanowires were lying on a silicon substrate and probed in back-scattering geometry as depicted schematically in the inset of Figure 3.5. In order to obtain a high signal intensity, the incident light was polarized along the nanowire axis. The scattered light was not analyzed for its polarization. According to Raman selection rules, in the back-scattering configuration on {110} surfaces the longitudinal optical (LO) phonon is forbidden, while the transverse optical (TO) phonon is allowed. Finite-difference time-domain simulations of the electromagnetic field distribution in the nanowires were performed with the simulation package *Meep* [109]. We have considered the hexagonal geometry of the nanowires and the different dielectric constants of the core and shell, taken from Ref. [110].

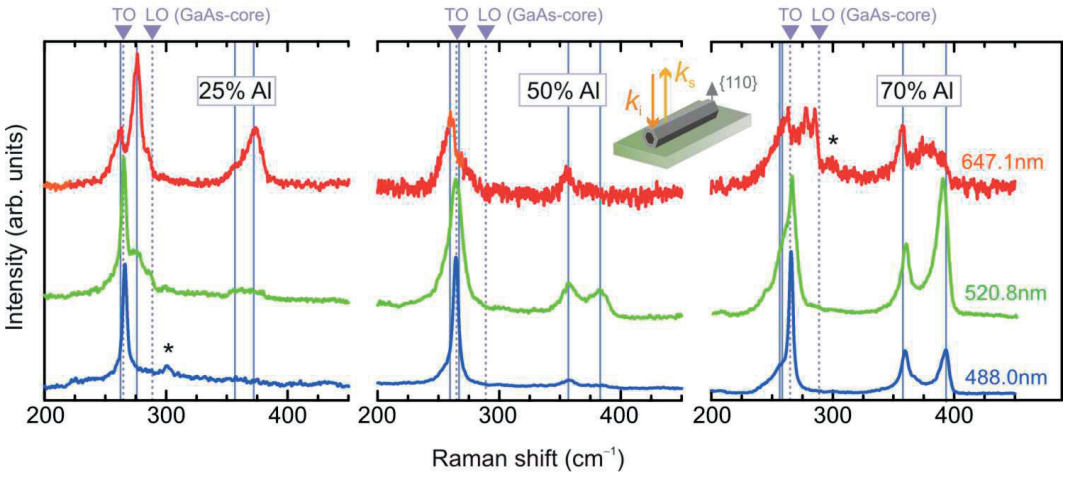

Figure 3.5 – Raman spectra of GaAs/$Al_xGa_{1-x}As$ core/shell nanowires with $x = 25\%$, 50% and 70% by using three different excitation wavelengths. The dotted (solid) lines correspond to the frequency position expected for the core (shell) modes. Silicon second order peak is indicated by a star.[111]

3.2.4 Results and Discussion

Raman spectra of GaAs/$Al_xGa_{1-x}As$ core/shell nanowires with x=25%, 50% and 70% are reported in Figure 3.5. Peaks corresponding to the optical phonons of the GaAs core and $Al_xGa_{1-x}As$ shell are identified. The TO mode from the GaAs core is at 265 cm^{-1}, in good agreement with the bulk value [51]. Due to the large mass difference between Al and Ga, two sets of alloy modes are given for the $Al_xGa_{1-x}As$ shell, whose frequency depends on the Al content. The GaAs-like modes lie very close to those from GaAs, while the AlAs-like are within the range of the 350 and 400 cm^{-1}. The alloy-related peaks are broader than those from GaAs, reflecting a higher degree of disorder. At a first glance, one can see that spectra of all samples are dependent on the excitation energy. Among the differences we find changes in the relative intensities between the peaks and the frequency position of the AlAs and GaAs-like modes.

We start reporting on the relative changes in the intensity of the TO and LO modes. As mentioned above, following the Raman selection rules the LO-related peaks should not be observed. In agreement with this, the LO mode from GaAs barely appears in all spectra, while this is not the case for the alloy-related LO modes. The shorter-range nature of alloy modes can contribute into a partial breaking in the selection rules. One should also consider that when the excitation source is close to the energy band-gap of the material, the exciton becomes the real intermediate state in the Raman process. This condition leads to resonant scattering and the intensity is enhanced. The enhancement is more important for the LO phonons as a consequence of the preferential interaction between the exciton and the longitudinal electric field induced by LO phonons. In general, we can see a higher ratio of the LO/TO intensities for conditions close to such a resonance. We can see this effect when measuring nanowires with $Al_xGa_{1-x}As$ shells containing x≈ 25% and x≈ 70% with respectively 647.1 nm and 520.8 nm

Table 3.1 – Optical phonon energies as obtained from fits to the spectra in Fig.3.5 and the relative alloy composition obtained from the expression given by Adachi. The fitting error was smaller than the experimental one (0.7 cm^{-1}), except for the frequencies marked with a star. In such cases, the signal was weak and the error in the Al content is calculated from the fitting error. Otherwise it was obtained by using the experimental value. LVM stands for local vibrational mode

λ	25% Al			50% Al			70% Al		
(nm)	Peak (cm^{-1})	Mode	Al%	Peak (cm^{-1})	Mode	Al%	Peak (cm^{-1})	Mode	Al%
647.1	262.2	TO,GaAs-like	38 ± 6	255.1*	TO,GaAs-like	81 ± 3	248.5*	GaAs-like	LVM
	276.0	LO,GaAs-like	27 ± 2	260.7	TO,GaAs-like	49 ± 5	261.3	TO,GaAs-like	45 ± 5
	285.6	LO,GaAs-like	7 ± 1	273.4	LO,GaAs-like	33 ± 2	278.0	LO,GaAs-like	23 ± 1
	361.7	LO,AlAs-like	7 ± 1	355.3	TO,AlAs-like	–	285.6	LO,GaAs-like	7 ± 1
	373.5	LO,AlAs-like	26 ± 1	372.0*	LO,AlAs-like	23 ± 3	356.9	TO,AlAs-like	–
							377.4	LO,AlAs-like	33 ± 1
							389.9	LO,AlAs-like	60 ± 2
520.8	258.0*	TO,GaAs-like	66 ± 4	256.7	TO,GaAs-like	73 ± 4	243.2*	GaAs-like	LVM
	265.3	*TO,GaAs*	*core*	265.9	*TO,GaAs*	*core*	257.3	TO,GaAs-like	70 ± 4
	276.3	LO,GaAs-like	27 ± 2	358.9	TO,AlAs-like	–	265.3	*TO,GaAs*	*core*
	286.7	LO,GaAs-like	5 ± 1	383.8	LO,AlAs-like	46 ± 1	358.6	TO,AlAs-like	–
	358.0*	TO,AlAs-like	–				383.3	LO,AlAs-like	45 ± 1
	373.4*	LO,AlAs-like	26 ± 4				389.8	LO,AlAs-like	60 ± 2
488.0	266.1	*TO,GaAs*	*core*	265.0	*TO,GaAs*	*core*	247.0*	GaAs-like	LVM
				358.2*	TO,AlAs-like	–	257.3	TO,GaAs-like	70 ± 4
							265.7	*TO,GaAs*	*core*
							359.6	TO,AlAs-like	–
							363.7*	LO,AlAs-like	10 ± 1
							389.9*	LO,AlAs-like	60 ± 2
							393.6	LO,AlAs-like	71 ± 2

wavelength, corresponding to 1.92 and 2.38 eV.

We now turn to the differences of intensity between the GaAs (core) and $Al_xGa_{1-x}As$ (shell) related peaks, as well as to the frequency position of the latter when probing with different excitation wavelengths. The Raman peaks were fitted with convoluted Lorentzian functions. The corresponding frequencies extracted from the fits are reported in Table 3.1. For the AlAs and GaAs-like peaks we also report on the corresponding aluminum composition, as obtained from the expression given by Adachi [112]. Due to the flat dispersion for the AlAs-like TO mode, we do not deduce any Al concentration from it.

Let us describe the spectra obtained for the nanowire with a 25% Al in the shell. When we excite with 488.0 nm, only the TO mode of GaAs is present. The spectrum does not show the existence of an $Al_xGa_{1-x}As$ shell. For longer wavelengths, other peaks appear, revealing the existence of the shell. This is a non-intuitive result, as in thin films one would expect to excite the parts closer to the surface with the shorter wavelengths. Exciting with 520.8 nm, two peaks are observed: the most intense one corresponds to the TO mode of GaAs (core), while the

less intense peak corresponds to a TO GaAs-like mode from the shell. There is an interesting change of the spectrum for the excitation with 647.1 nm. Here the AlAs and GaAs-like modes appear with a remarkably higher intensity. This increased scattering intensity is explained by approaching the resonance conditions. In fact, this excitation wavelength corresponds to the resonance condition of $Al_xGa_{1-x}As$ with x≈ 35%. The positions of the LO GaAs and AlAs-like peaks are consistent with an Al composition of 26-27%, while the TO GaAs-like peaks suggest a higher Al composition (38%). As a general trend, the Al content obtained from TO is higher than LO. We attribute this to a slight difference in the dependence of the TO and the LO GaAs-like modes as a function of the stoichiometry of the $Al_xGa_{1-x}As$.

We turn now to the nanowires with 50% Al in the $Al_xGa_{1-x}As$ shell. Also here, the signal from the GaAs core is mostly prominent when probed with the short wavelength (488.0 nm). The spectrum obtained with 520.8 nm excitation contains information on the core and the shell. In contrast, when we excite with 647.1 nm, mostly only the TO peaks related to the shell are present. Here, the TO GaAs-like peaks suggest an Al concentration around 50%. Interestingly, we observe a peak consistent with 33% Al when exciting with 647.1 nm. We attribute this to the existence of inhomogeneities in the shell as reported in Figure 3.4 and in agreement with what has been found in the past in similar structures.Indeed, previous studies [89] have shown that there is segregation of Al in {112} apex of hexagonal section. Moreover, in the facets {110}, there is an additional variation in composition at the nanometer scale. Even though these regions are in the order of few nanometers, the resonance conditions enable us to detect them in an enhanced manner.

To complete the picture, we comment on the measurements performed on the nanowire with an $Al_xGa_{1-x}As$ shell of x=70% Al. In addition to the variation of the signal intensity between core and shell as a function of excitation wavelength, we also observe a marked change in the frequency position of the shell related peaks. Since it is difficult to distinguish the GaAs-like TO and LO modes, we consider not appropriate to extract the concentration from one of the two curves, while it is possible to fit one peak, revealing their character of localized mode of an isolated Ga atom in AlAs. The position of the LO AlAs-like peak is consistent with an aluminium concentration x=70%, in the spectrum obtained with 488.0 nm wavelength, while we find the LO AlAs-like mode corrisponding to 60% Al content when probed with 520.8 nm. In fact this is consistent with the 520.8 nm wavelength being in resonance with an $Al_xGa_{1-x}As$ of x≈ 65%. The spectra obtained with the 647.1 nm wavelength are richer in peaks. The different observed peaks are consistent with different Al concentrations between 7% and 60%. Similar concentrations are obtained for both the GaAs and AlAs-like modes. As for the previous nanowires, the different Al concentration are attributed to the fluctuation of the Al composition in the shell.

Finally, we address the differences in the spectra as a function of the excitation wavelength by considering the distribution of the photonic modes within the nanowire as a function of the excitation wavelength. It is well-known that the Raman scattering intensity is directly linked to the local internal electric field of the excitation [24]. In order to assess the distribution of

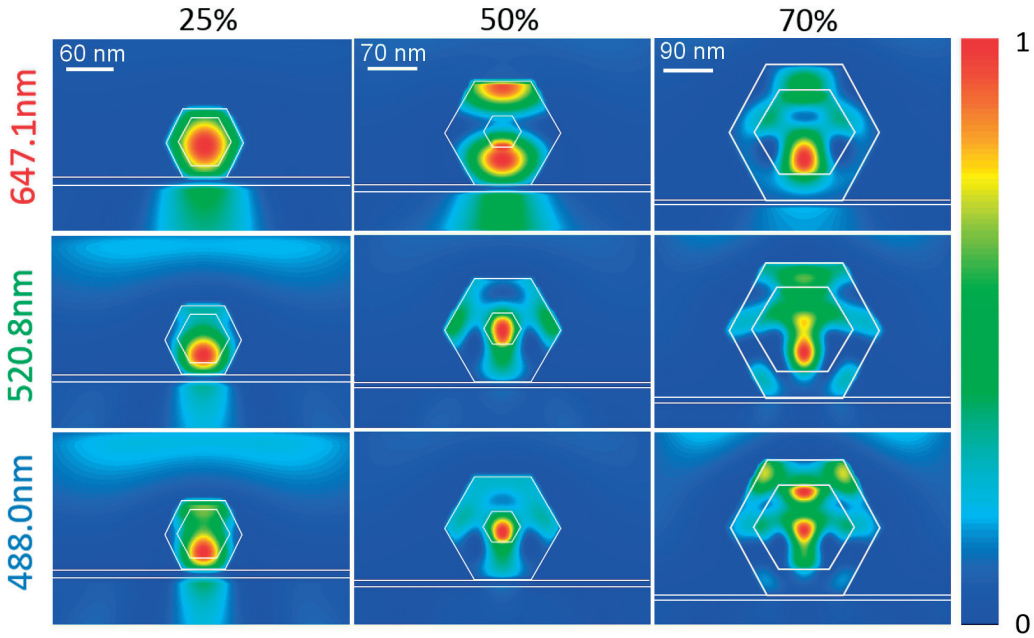

Figure 3.6 – Simulated cross-sectional maps of the internal field energy density distribution given by a top plane wave incoming onto GaAs/$Al_xGa_{1-x}As$ core/shell nanowire system, as described in the manuscript. From bottom to top, the fields correspond to a excitation wavelength of 488.0, 520.8 and 647.1 nm, respectively.

the radiation in the nanowires, we have performed Finite-Difference Time-Domain (FDTD) simulations considering the exact hexagonal geometry of the nanowire and the dielectric constants of the core and shell. We have simulated a plane wave polarized along the nanowire axis. We have reported in Appendix A an animation of the electric field energy density as a function of the time under periodic steady state. Figure 3.6 shows the cross-sectional maps of the time-averaged electric field energy density obtained for a nanowire lying on a Si/SiO_2substrate during illumination from a top monochromatic light source. Clearly, light distributes unevenly across the nanowire cross-section. The simplest case corresponds to the nanowires with a 25% of Al in the shell. The simulations show a gradual increase of the field in the shell by increasing the wavelength. However, the field in the core is always the most intense. This is because of the small size of the nanowire. The simulations match well with the experiments, where an increase of the peaks related to the shell is observed by increasing the wavelength. We must note here, that for the 647.1 nm excitation probing the Raman, intensities of the peaks related to the shell are also intensified because of the near resonance conditions.

In the case of the nanowires with 50% Al shell, the light field is more intense in the core (GaAs) for an incoming wavelength of 488.0 nm, while light becomes distributed around the shell when using longer wavelengths. These results are in excellent agreement with our experiments, where the core-related Raman signal mostly not present when exciting with the 647.1 nm wavelength. Finally, in the nanowire with x=70% , there is no obvious trend. It must be noted

that at short wavelength, the local field energy around the shell is confined at the edges of the nanowire cross-section where the Al content is found the largest. This would be in agreement with the observation of an increasing Al content from Raman spectra with excitation energy. However for this sample the photonic effects are in harmony with an increase of the Raman intensity of area with high Al content due to selective resonance. Consequently, we cannot discern the two effects here.

3.2.5 Conclusion

As a conclusion, we have shown that a complete chemical characterization of core-shell nanowire structures requires the probing with different wavelengths as well as simulations of the photonic modes existing in the nanowires for the different excitation wavelengths. The multi-spectral characterization enables the probing of different parts of the cross-section as well as the local inhomogeneities in chemical composition.

3.2.6 Acknowledgments

FA and AFiM thank funding from SNF through project nr 137648. EAL acknowledges funding from Marie Curie Actions Program. AFM thanks funding through the ERC Starting Grant UpCon and NCCR-QSIT. J.A. acknowledges the funding from the Generalitat de Catalunya 2014 SGR 1638. M.d.l.M. thanks the CSIC Jae-Predoc program.

3.3 Tuning the response of non-allowed Raman modes in GaAs nanowires

Francesca Amaduzzi[1], Esther Alarcón-Lladó[1], Hubert Hautmann[1], Rawa Tanta[2], Federico Matteini[1], Gözde Tütüncüoğlu[1], Tom Vosch[3], Jesper Nygard[2], Thomas Jespersen[2], Emanuele Uccelli[4] and Anna Fontcuberta i Morral[1]

3.3.1 Abstract

We report on the use of photonic resonances in Raman spectroscopy on single nanowires for the enhancement of forbidden modes and the study of the interaction of phonons with free-carriers. This is achieved by suspending nanowire over a trench and detecting Raman scattered light with light polarized along the radial direction. Thanks to the photonic nature of the light-nanowire interaction, light polarization inside the nanowire is modified. This results in the excitation of LO modes, forbidden on {110} surfaces. We apply this new configuration to the measurement of carrier concentration on doped GaAs nanowires. These results open new perspectives for the study of the interaction of free-carriers or plasmons with optical phonons in nanostructures.

3.3.2 Introduction

Raman spectroscopy is a widely used non-destructive technique used for the characterization of phonon spectra in materials [113, 114, 115]. The position and intensity of the Raman modes is related to the composition, crystal structure, lattice parameters and carrier density [92, 91, 56, 116]. From the birth of nanotechnology, this technique has also been applied to the characterization of nanostructures [24, 117, 118, 119, 26, 18, 94]. In particular Raman spectroscopy is a promising technique for the detection of free carriers in nanowires [120]. In fact, contactless techniques, such as Terahertz [41, 121] and Raman [120, 33] spectroscopies, have obvious technological advantages over traditional electrical measurements. In particular, thanks to its local nature, Raman spectroscopy is a suitable tool for the detection of free carriers in a single nanowire [33]. This is possible in polar semiconductors through the coupling of the longitudinal optical phonons with the longitudinal plasma oscillations of the free carriers.

For nanowires lying down on a substrate, the LO mode cannot be accessed with backscattering configuration. In fact, the intensity of Raman scattering follows certain selection rules. These depend on the direction of propagation and polarization of incident light as well as on the symmetry of the scattered mode [51]. Forward scattering geometry has to be set to access the LO mode [33]. However, the forward scattering geometry is not straightforward to implement. Alternatively, one could use resonant Raman scattering conditions to observe LO and LO-coupled modes in backscattering conditions, provide one uses a laser energy close to the bandgap [122]. On the other hand, it has been shown that the Raman scattering spectra follow different patterns when the dimension of the crystal size becomes of the order of the excitation wavelength [62, 64]. In particular, it has been shown that photonic resonances lead to the

enhancement of the local electric fields, similar to Mie scattering in dielectric spheres, and severely affect the response of the material [24, 65].

The intensity of Raman scattering follows certain selection rules. These depend on the direction of propagation and polarization of incident light as well as on the symmetry of the scattered mode [51]. In nanostructures such as nanowires, the presence of photonic modes produces not only a local enhancement of the light intensity inside the nanostructure, but also results in a modification of its direction and polarization [24, 123]. In an effective manner, this leads the breakdown of the selection rules from a macroscopic point of view: the Raman intensity of the modes is no longer directly linked to the characteristics of the incident and scattered light nor from the incident facets. In this work we show how it is possible to modify the macroscopic Raman selection rules by changing the photonic environment, i.e. by suspending the nanowire. We demonstrate the enhancement of longitudinal optical phonon mode, which is generally used for the characterization of free-carriers (plasmons) in semiconductors. This work opens new avenues for the use of Raman spectroscopy as a characterization tool in doped and high mobility nanowire heterostructures [124].

3.3.3 Experiment

In this work we use undoped and p-type doped GaAs nanowires obtained by molecular beam epitaxy (MBE) by the gallium assisted method as described in the references [105, 30]. The catalyst-free grown GaAs nanowires exhibit a hexagonal cross-section. According to the growth conditions, we expect the nanowires to have a zinc-blende structure and with side facets pertaining to the {110} family. The undoped nanowires present an average diameter of 88 nm and an average length of 12 μm. For the p-type GaAs nanowires, different doping concentrations were achieved by adding an additional source of Silicon during the axial growth of the nanowires [33]. This silicon flux leads respectively to a total Si concentration of 5.5×10^{18} cm^{-3}, 1.4×10^{19} cm^{-3} and 4.0×10^{19} cm^{-3} in a thin film grown at the same rate. The p-type nanowires present an average diameter of 150 nm and an average length of 15 μm. The nanowires were mechanically transferred onto new substrates. Two different kinds of substrates were used: bare silicon and 2 μm wide and 500 nm deep trenches opened on silicon wafers with 1 μm thick thermal oxide fabricated by photolitography and etching processes. Similar results were also obtained for trenches 200 nm high.

The trenches allowed the Raman scattering measurements on freely suspended nanowire segments. Raman scattering measurements were performed on single nanowires at room temperature. The 488.0 nm line of an Ar-Kr$^+$laser was used. The laser with a power of ≈ 100 μW was focused on the nanowire with a microscope objective with numerical aperture $NA = 0.75$. The nanowires were probed in back-scattering configuration. The polarization of the incident light was controlled with a polarizer. All scattered light was detected regardless of the polarization. The spectra of the scattered light were recorded by a TriVista triple spectrometer and a liquid nitrogen cooled multichannel charge-coupled-device (CCD) detector.

Three-dimensional finite-element in frequency domain simulations of the electromagnetic field distribution inside the nanowires were performed with the simulation package COMSOL Multiphysics.

3.3.4 Results and Discussion

Fig. 3.7 a and b show typical Raman spectra of a single GaAs nanowire for the two different substrate configurations and for two different incident polarizations: parallel to the nanowire axis and perpendicular (cross-polarization configuration).

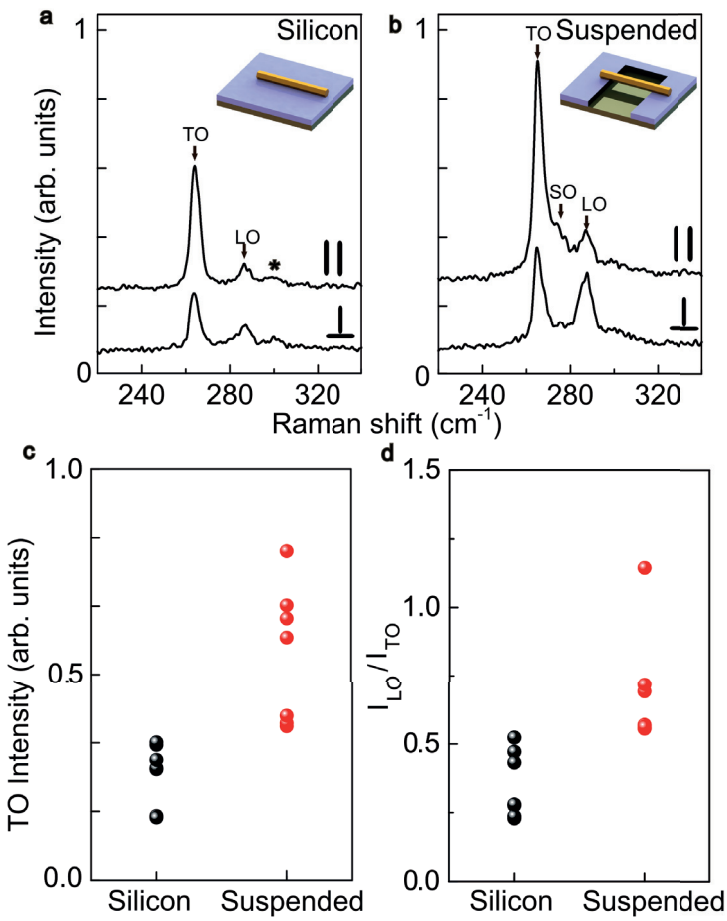

Figure 3.7 – Raman spectra of GaAs nanowires a) on silicon and b) freely suspended with incident light polarized perpendicular and parallel to the nanowire axis. Silicon second order peak is indicated by a star [111]. Each spectrum is normalized to the first order Raman mode of reference sample of Silicon. Plot depicting the TO intensity in parallel configuration c) and the ratio I_{LO}/I_{TO} for perpendicular configuration d) of individual wires on silicon and freely suspended.

To avoid artifacts from slight differences in set-up alignment, we have adjusted the spectra intensities to a Silicon reference. Two main peaks are identified at 265 cm^{-1} and 289 cm^{-1}, associated with the transverse optical (TO) and longitudinal optical (LO) phonons of GaAs, respectively. These values are in good agreement with the reported bulk values for GaAs [51]. We do not detect any of the peaks related to the wurtzite phase [18], indicating a good crystal purity. The scattering intensity is higher for the incident polarization parallel to the nanowire. This is due to the much higher absorption cross-section for this configuration and also called antenna effect [96]. The intensity of the TO mode is significantly higher than the LO mode. This difference can be attributed to the fact that only the TO mode is allowed in the backscattering configuration on {110} surfaces. Interestingly, the LO mode unexpectedly emerges when the light is polarized perpendicularly to the nanowire axis. The observation of symmetry forbidden peaks, with an increase of the peaks width, is often associated to the existence of impurities and reduced crystal quality [125, 126]. Due to the small width of the TO mode and the absence of polytypism, we expect neither of these effects to play a role here.

The Raman spectra obtained on the suspended GaAs nanowires present some different characteristics. First, the spectrum obtained with light polarized along the nanowire axis exhibits an extra peak slightly overlapping to the TO mode. We attribute this peak to the surface optical (SO) mode, typically detected in nanowires due to the high surface to volume ratio [21]. Interestingly, also a significant increase of the Raman scattering intensity is observed when the nanowire is suspended. We can observe that the intensity of the TO mode of the suspended nanowire is about twice the intensity of the TO mode of the one on the silicon. The same trend is observed with incident light polarized perpendicular to the nanowire axis. Finally, we see how the I_{LO}/I_{TO} ratio is also larger for the suspended configuration than for the nanowire on silicon, especially in cross-polarization configuration. In order to illustrate in a more representative manner the increase in intensity between two configurations, we have measured several nanowires (Fig 2c/d). We can observe a clear trend, where suspending the nanowire not only provides higher signal but also higher I_{LO}/I_{TO} ratio. This constitutes an optimal configuration for the assessment of the phonon-plasmon interaction to assess the density of free-carriers.

In order to further illustrate the dependence of the Raman intensity on the scattering geometry, polarization-dependent measurements were performed for the two different substrates, using the scattering configuration as shown in Fig. 3.8a. In Fig. 3.8c and d polar plots of the TO and LO intensities, normalized to the highest intensity value of TO mode of each plots, as well as the I_{LO}/I_{TO} ratio are reported as a function of the polarization angle of the incident light. As a reference, we show the polarization dependence expected from bulk material based on the Raman selection rules for back-scattering configurations in Fig. 3.8b, mentioned before. Only TO mode is allowed in the backscattering configuration on {110} surfaces. By comparing the theoretical plot to the experimental, we can observe that the experimental TO polar plot is slightly tilted with respect to theory, probably due to the antenna effect. Additionally, the I_{LO}/I_{TO} ratio shows an increased value in the case of cross-polarization configuration.

As it will be illustrated in the following, the differentiated Raman response of the suspended

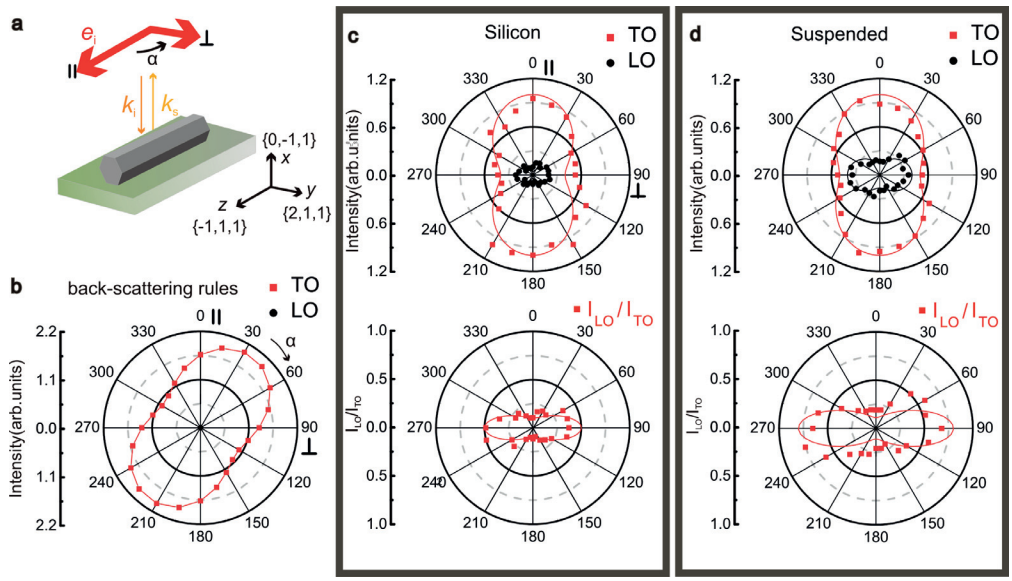

Figure 3.8 – a) Schematic diagram of the experimental scattering geometry. b) Calculated intensity polar pattern of the unpolarized scattered light as a function of the incident polarization respect to the wire axis for backscattering configurations. c) and d) Polar plots for the TO and LO modes and for I_{LO}/I_{TO} ratio intensities versus the angle of the polarization of the incident light respect to nanowire axis for a wire lying on Silicon and on air respectively. The lines are guides to the eyes.

nanowires can be ascribed to changes of local polarization within the nanowire core. This is the consequence of the photonic nature of the light-nanowire interaction. It is well known that the Raman scattered intensity is proportional $I_s \propto |\hat{e}_i \cdot \mathbf{R} \cdot \hat{e}_s|$, where $\mathbf{R}$ is the Raman tensor which depends on the crystal symmetry and $(\hat{e}_i)$ and $(\hat{e}_s)$ are the polarization of the incoming and scattered light respectively.

For zinc-blende GaAs, the Raman tensors and bases can be found in Ref. [51, 18]. Using the bulk Raman selection rules, we have calculated the I_{LO}/I_{TO} ratio in function of the angle β with respect to the direction of the light incident respect to the one in backscattering (β=0°)(Fig. 3.9). The scattered photon direction is maintained. In this case, the polarization of the incident light is perpendicular to the nanowire axis. As expected, the LO mode is not allowed in back-scattering (0°). At 90° scattering LO is allowed and the I_{LO}/I_{TO} ratio becomes 1. In forward scattering this ratio achieves the highest value, 3.

In the body of the nanowire, the wavevector and the polarization of the local field can differ significantly from the incident macroscopic ones [123]. We have calculated the polarization and direction of the internal electric field inside the nanowires by using the software COMSOL Multiphysics, with the electromagnetic waves module and the frequency domain model based on Maxwell's equations. We have considered a plane wave incident from the top and polarized along and perpendicularly to the nanowire axis in the two cases considered here: lying on a silicon substrate and freely suspended. In Fig. 3.10, the cross-sectional maps of the electric

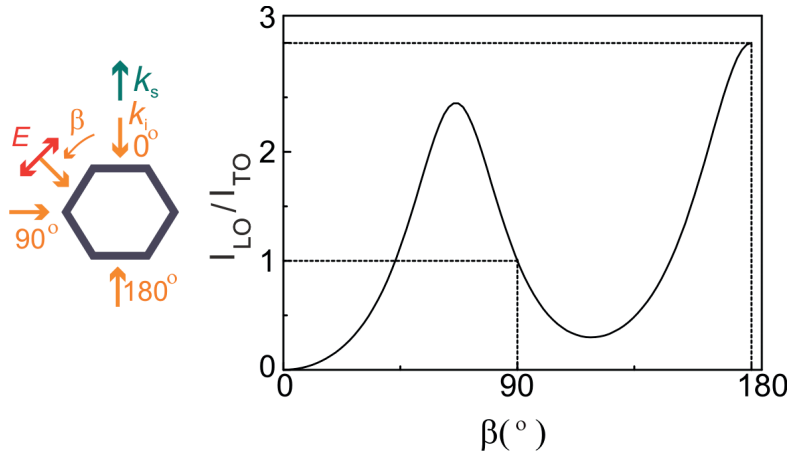

Figure 3.9 – Calculated LO/TO ratio using the Raman selection rules in function of the angle drawn by the direction of the light incident from back scattering configuration (β=0°) to forward configuration (β=180°).

field intensity squared inside the nanowire are presented. The cones inside the nanowire represent the direction of the wavevector and the polarization. The electric field intensity squared is color-coded.

We find that the distribution of the electric field intensity squared, the direction and polarization of the light depends on the incident polarization and on the photonic environment. For the two cases, the incident light polarized along the nanowire keeps to a high degree its polarization inside the nanowire. In general, the direction of the light propagation remains unchanged and one expects macroscopic-like selection rules. The situation is significantly different in the case of polarization perpendicular to the nanowire axis. Here, the propagation direction and the polarization change to a very high extent and depend on the environment. The propagation direction tends to point from the facets to the center of the nanowire. Light polarization inside the nanowire close to the facets is parallel to them and perpendicular to the nanowire axis. Thus, for the nanowires lying on silicon, light enters the nanowire from all facets, except from the one in contact with the substrate. With most of the light entering from the side, the scattering is now at ~90° scattering, for which the presence of LO is allowed. This is consistent with the observed increase of the I_{LO}/I_{TO} intensity ratio with the cross-polarized configuration. In the case of the nanowire freely suspended with perpendicular polarization, light also enters from the bottom facet. As a result almost the forward configuration can be achieved. With this one would expect a higher I_{LO}/I_{TO} ratio, as observed in the experimental data, i.e. the increase in the I_{LO}/I_{TO} intensity ratio of wire freely suspended compared to the one on substrate.

The existence of photonic resonances in nanowire structures can also explain the higher Raman signal in the case of suspended nanowires. In this case, light is confined in the high-refractive index material (for GaAs n=4.39 [127] at the wavelength of 488 nm).When the nanowire lies on the silicon light can drain through the substrate, which has almost the same

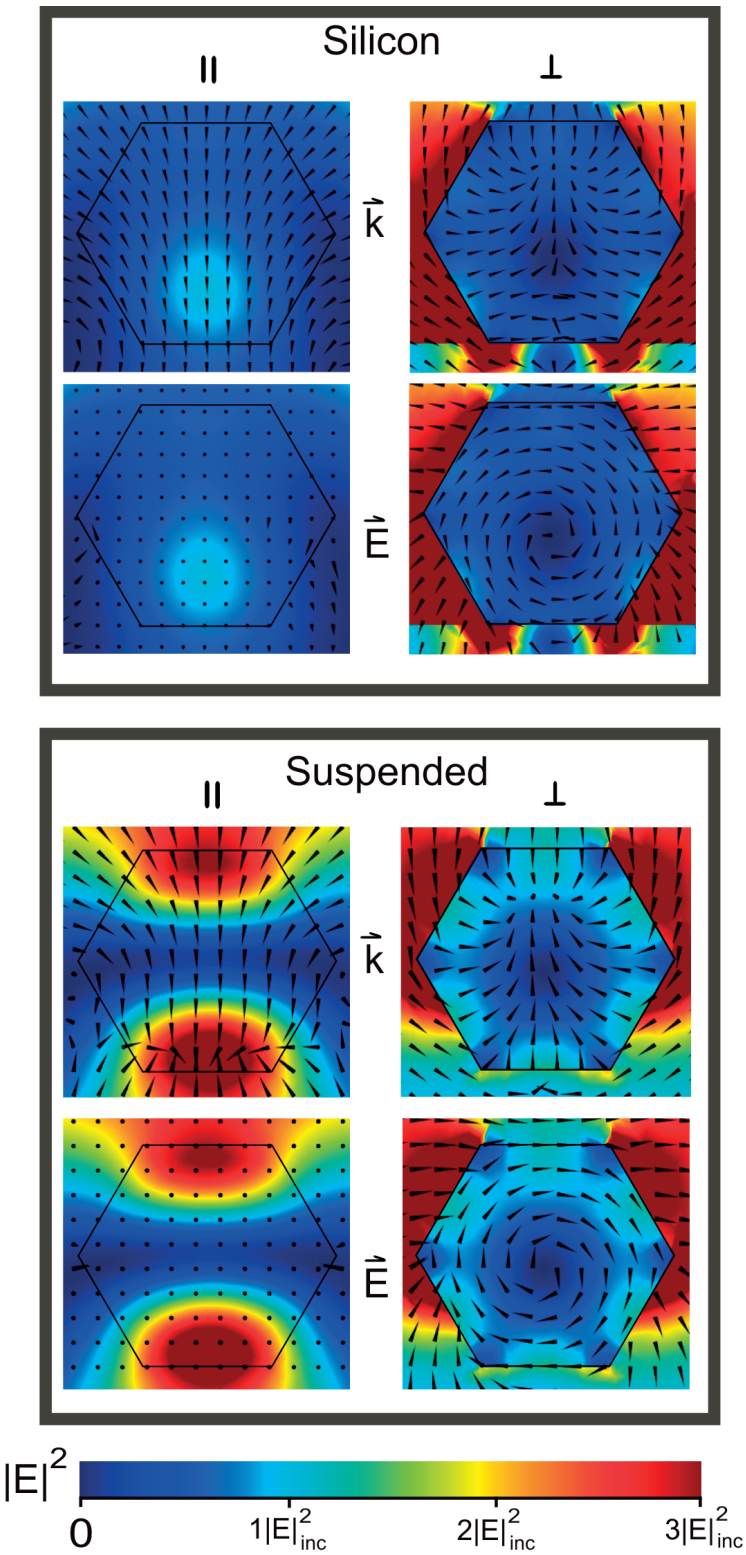

Figure 3.10 – Calculated electric field intensity squared maps for a wire lying on silicon and freely suspended for light parallel and perpendicular to the nanowire axis. The cones represent the direction (top) and the polarization (bottom) of the light.

refractive index (n=4.37 [128] at the wavelength of 488 nm). This results in a lower light absorption and extraction with respect to the suspended case.

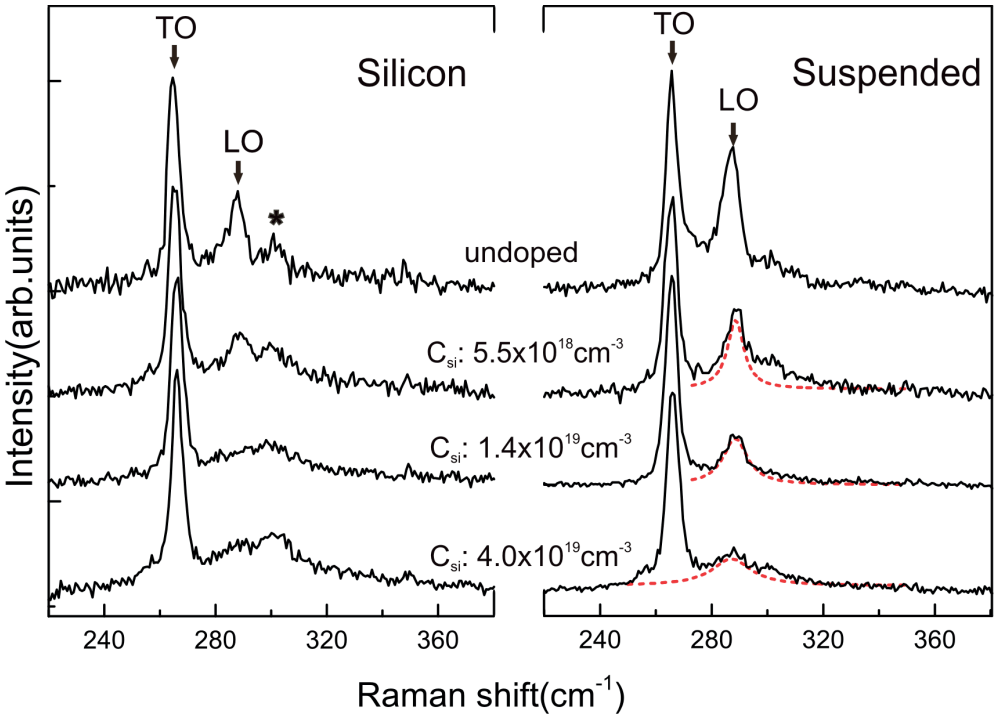

Figure 3.11 – Raman spectra of p-type GaAs nanowires taken in backscattering configuration. The polarization of the incident light is chosen perpendicular to the nanowire axis. The nominal Si concentration of the different samples is 5.5×10^{18} cm^{-3}, 1.4×10^{19} cm^{-3} and 4.0×10^{19} cm^{-3}. Silicon second order peak is indicated by a star. The intensity of each spectrum has been renormalized with respect to the TO.The dashed lines are fits of the coupled-mode obtained using Eq. 3.

Finally we turn to the application of this method to the measurement of coupling the LO mode with the plasmons generated by the free-carriers. This enables a quantification of the mobility and carrier density. For this, we have used GaAs nanowires with three different p-type doping concentrations which had been fully characterized in a previous study [33]. In this case the nanowires have a slightly larger diameter: 150 nm. While one expects photonic effects to play a less significant role in selection rules for larger diameters, this is still not the case. Fig. 3.11 shows the Raman spectra of GaAs nanowires with three increasing p-type doping concentrations. The measurements are performed in the best condition, thus with the light polarized perpendicular to the nanowire axis. We have probed nanowires on a silicon substrate and freely suspended to illustrate the potential of our technique. As expected, the LO signal is much better observed when the nanowires are suspended. In the case of the suspended nanowires (right), we observe a decrease of the intensity and a broadening of the LO mode, in excellent agreement to the previous work performed on the same nanowires in forward scattering configuration [33].

For nanowires lying on silicon (left), we observe a low intensity of the LO mode, only for the nanowire with the lowest doping concentration. For the other two samples it is not possible to recognize the LO mode. We have fitted the LO mode shape and position from the spectra of the suspended nanowires to determine the concentration and the mobility of free holes. For this, we have considered the standard dielectric theory in the formalism of Hon and Faust [129]. The differential Raman cross-section from coupled phonon-plasmon modes has the form:

$$\frac{\partial^2\sigma}{\partial\omega\partial\Omega} \propto (n(\omega)+1)I[\frac{1}{\epsilon(\omega)}[\frac{\epsilon_\infty}{4\pi}+2A\chi_I(\omega)-A^2\chi_I(\omega)(1+\frac{4\pi}{\epsilon_\infty}\chi_e(\omega))]] \tag{3.1}$$

where $\epsilon(\omega) = \epsilon_\infty + 4\pi(\chi_I(\omega)+\chi_e(\omega))$ is the dielectric function that is written as a sum of the ionic $\chi_I(\omega)$ and free carrier $\chi_e(\omega)$ contributions, $n(\omega)$ the Bose-Einstein distribution, $A = \omega_{TO}^2 C/(\omega_{LO}^2-\omega_{TO}^2)$ with C being the Faust-Henry coefficient and ω_{TO}^2 and ω_{LO}^2 are the frequencies of TO and LO modes respectively. The ionic contribution to the susceptibility is given by:

$$\chi_I(\omega) = \frac{\epsilon_\infty}{4\pi}\frac{\omega_{LO}^2-\omega_{TO}^2}{\omega_{TO}^2-\omega^2-i\omega\Gamma_i} \tag{3.2}$$

with Γ_i the phonon damping constant.

For a concentration of carriers in the range considered here, the free-carrier susceptibility can be calculated using the Drude model [130]:

$$\chi_e(\omega) = -\frac{\epsilon_\infty}{4\pi}\frac{\omega_p^2}{\omega^2-i\omega\Gamma_p} \tag{3.3}$$

where ω_p is the plasma frequency: $\omega_p^2 = \frac{4\pi}{\epsilon_\infty}\frac{pe^2}{m^*}$ with p the free-hole concentrations and Γ_p is the damping constant related to the mobility and the lifetime of the plasmon ($\Gamma_p = \frac{1}{\tau} = \frac{e}{\mu m^*}$).

We have summarized the input parameters for the coupled phonon-plasmon modes Raman cross-section in Table 1.

From the expression of the density of states, the ratio between the concentration of light holes and heavy holes is $(m_{lh}/m_{hh})^{3/2}$. As a result the light hole population is one order of magnitude smaller than the heavy holes. Most of holes are in the heavy-hole bands with an effective mass value of $0.51m_e$ [132]. In spite of that, we have included the contribution of light holes with effective mass of $0.082m_e$ [132] in the calculation of susceptibility. Because the main scattering process is due to the presence of the ionized impurities [133, 134, 135], we consider the heavy and light holes have a similar lifetime, so they can be fitted with the same damping constant. The coupled-mode fits to the spectra are displayed in Fig. 3.11 as a dashed lines superimposed to the corresponding Raman spectra. We extract the following free-hole concentrations: 5.5×10^{17} cm^{-3}, 2.6×10^{18} cm^{-3} and 7.3×10^{18} cm^{-3} for the samples with nominal

Table 3.2 – Input parameters for the coupled phonon-plasmon modes Raman cross section.

Symbol	Description	Value	Ref.
ω_{LO}	LO,GaAs	288 cm^{-1}	*
ω_{TO}	TO, GaAs	266 cm^{-1}	*
Γ_i	GaAs phonon damping constant	5 cm^{-1}	*
C	GaAs Faust-Henry coefficient	-0.55	[131]
m^*_{hh}	heavy hole effective mass	0.51	[132]
m^*_{lh}	light hole effective mass	0.082	[132]
ϵ_∞	GaAs high-frequency dielectric constant	10.9	[132]

* present work

Silicon concentrations of respectively 5.5×10^{18} cm^{-3}, 1.4×10^{19} cm^{-3} and 4.0×10^{19} cm^{-3}. If all Silicon atoms are active, the nominal holes concentrations are : 1.9×10^{18} cm^{-3}, 3.2×10^{18} cm^{-3} and 5.5×10^{18} cm^{-3} for the sample from the lowest to highest value of doping respectively, which are in agreement with the values extracted by the coupled-mode fits.

As expected, the mobility of heavy (light) holes decrease from 47 (300) cm^2/V sec to 12 (76) cm^2/V sec when the doping increases. As a result, we are able to probe the concentration and free-carrier density without complication of forward-scattering in the optical set-up. This configuration also enables a relatively straight forward measurement at cryogenic temperatures, which is much more challenging in the case of forward-scattering.

3.3.5 Conclusion

In conclusion, we have shown how Raman selection rules in nanowires can be modulated by making use of the photonic modes of freely-suspended nanowires. We have justified this in terms of the changes in the direction and the polarization of the field inside the nanowires. We have applied this method to the determination of carrier concentration and mobility in p-doped GaAs nanowires. This opens the path to the contact-less assessment of high mobility carriers in nanowire heterostructures.

Acknowledgments

We thank A. Dalmau Mallorqui and J. Vukajlovic Plestina for their precious help and advice in the cleanroom. FA and AFiM thank funding from SNF through project nr 137648. EAL acknowledges funding from Marie Curie Actions and the SNF-Ambizione Programs. AFM thanks funding through the ERC Starting Grant UpCon and the SNF NCCR-QSIT.

4 Determination of electronic properties with Raman spectroscopy

Semiconductor nanowires can be very attractive materials for certain nanoscale photonic and electronic devices, such as lasers, detectors and solar cells. In order for these future technologies to become a reality, a good understanding of their electronic properties is fundamental. Traditionally, the electronic properties are determined with electrical measurements. For this, time consuming, costly and complex clean-room processes are required. In this regard, thanks to its contact-free nature, micro-Raman spectroscopy is a powerful tool for the detection of free carriers in polar semiconductor. This is possible thanks to the coupling of plasmon with longitudinal optical modes.

In this chapter, we will assess the viability of the Raman spectroscopy as a non-destructive technique to obtain carrier densities and mobilities of two different type of nanowires.

Firstly, after a review of modulation doping in bulk materials, the electronic properties of modulation-doped GaAs-$Al_{1-x}Ga_xAs$ nanowires as a function of the temperature will be evaluated. Next, we will study $InAs_{1-x}Sb_x$ nanowires and the coupling between its LO phonons and carriers. In addition, we will investigate the dependence of the antimony content in InAsSb on the Sb content, and assess the role of the temperature sample and of the wire-passivation in the mobility.

4.1 Modulation-doped structures

4.1.1 Introduction

The term "low dimensional system" refers to a system, where the charge carriers are confined within a barrier potential in one or more dimensions, which restricts their free movement. One of the major developments in the semiconductor history was the implementation of 2DEG (2 Dimension Electron Gas). One of the most common system to obtain a 2DEG is the GaAs-$Al_{1-x}Ga_xAs$ interface. The possibility to control the band gap by replacing Ga atoms with Al in $Al_{1-x}Ga_xAs$, without suffering from strain and dislocation at the GaAs-$Al_{1-x}Ga_xAs$ interface, is a great advantage to grow heterostructures with such materials. In fact, $Al_{1-x}Ga_xAs$ exhibits almost the same lattice parameter the GaAs. In this section, we address doped structures of particular interest to electronics, the so-called modulation doped structures, which enable the presence of a 2DEG. Fig. 4.1 shows a scheme of a typical band alignment in a GaAs-$Al_{1-x}Ga_xAs$ 2DEG structure. Modulation doped heterostructures consist in general of a type I heterostructures, where the material with the larger bandgap is doped at certain distance from the interface, for example with donors. In order to maintain a constant chemical potential throughout the two materials, electrons will flow towards the material with lower band gap. This causes the band edge to bend at interface (band-bending) and thus, the electrons are confined by an approximately triangular potential near the interface in the form of a two dimensional electron gas. This 2D electron gas is physically separated from the ionized impurities. This enables the increase in mobility thanks to the reduction of impurity scattering mechanism. Moreover, the confinement in a triangular potential lead to energy levels called energy subband.

The first reported work on GaAs-$Al_{1-x}Ga_xAs$ Modulation-doped GaAs-$Al_{1-x}Ga_xAs$ system [136] showed an increase of the low-temperature mobility of GaAs. Fig. 4.2 shows how the improvement of the mobility has continued over the years, producing an increase of four order

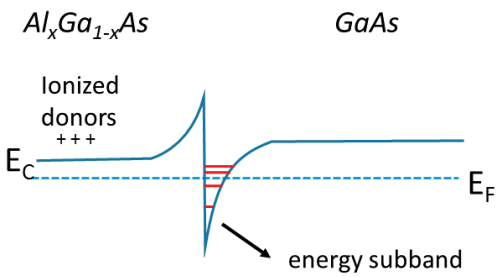

Figure 4.1 – Diagram showing the bending of the conduction band for GaAs-$Al_{1-x}Ga_xAs$ modulation doped heterojunction. The positions of the confined electrons and of the Si-doped atoms are indicated.

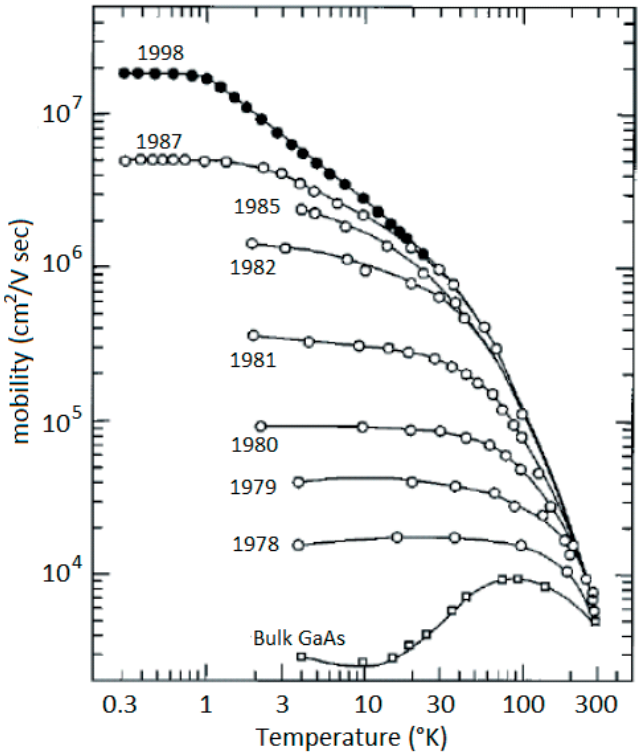

Figure 4.2 – Temperature dependence of the Hall mobility achieved during the years of the history of modulation-doped structures. Reprinted from Ref. [137], with the permission of AIP Publishing.

of magnitude for a thin film mobility. One of the major contributions for scattering at low temperature is due to the ionized impurities unintentionally or intentionally implemented in the material. Decreasing the sample temperature below 50K the effects of optical and acoustic phonons scattering fall rapidly and the ionized impurity scattering becomes dominant. In fact, the low-temperature mobility in modulation-doped system can increase by orders of magnitude since the impurities content can be decreased indefinitely. Therefore, at low temperature, samples of different quality can be discriminated easily. Contrarily, at high temperature, polar optical scattering dominate the mobility and a dramatic decrease of mobility happens reaching the value of bulk mobility.

In a modulation-doped system, additional scattering mechanism, which are absent in bulk materials can be relevant. In the following, we review the scattering mechanisms that play a role in these samples:

- *Alloy scattering*

  Alloy scattering is present in $Al_{1-x}Ga_xAs$ system due to the alloy disorder. This mechanism is not really relevant since electrons are confined in GaAs material and only the tail of electron wave-function falls inside the alloy material.

- *Interface scattering*

  Interface surface roughness constitutes a scattering source because the periodicity of the lattice is interrupted by it.

- *Background impurities scattering*

  This scattering mechanism is due to the presence of unintentional impurities incorporated during the growth. This can be decreased growing cleaner sample.

- *Remote donors scattering*

  Intentional dopants are located at certain distance from the carriers but they can still be source of scattering. The influence of this scattering mechanism become larger reducing the distance between dopants and carriers. Ideally, one could increase the distance to increase the mobility limited by this scattering mechanisms, but the spacer thickness cannot be increased indefinitely as this would reduce the electron density at the GaAs interface.

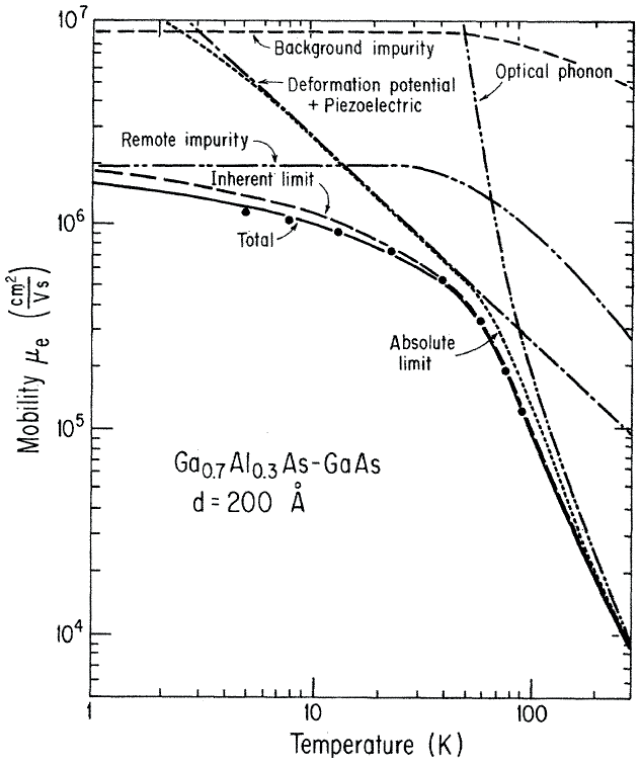

Figure 4.3 – Significance of different scattering mechanisms in modulation doped system. Reprinted figure with permission fromRef. [138]. Copyright 2014 by the American Physical Society.

Fig. 4.3 highlights the relevance of the different scattering mechanisms in modulation doped system GaAs-$Al_{1-x}Ga_xAs$. Alloy and interface roughness scattering are considered irrelevant

for extremely clean samples. Depending on the distance between dopants and carriers and on the concentration of background impurities, the saturation of mobility at low temperature can be related to the density of background impurity or remote donors scattering.

4.1.2 Inelastic light scattering in modulation-doped structures

Inelastic light scattering gives direct access to the elementary excitations of low-dimensional systems. The collective excitations are the so-called spin density excitation (SDE) and charge-density excitation (CDE). In the CDE the electrons are oscillating in phase. On the contrary, in the SDE, electrons with opposite spins are oscillating out of phase. At microscopic level, the charge density excitation consists of non-spin-flip transitions between subband states, coupled by Coulomb interactions, whereas the spin density excitation consists in intersubband spin-flip and non-spin-flip transitions, coupled by the exchange interaction [139]. The energies of the intersubband excitation are shifted from subband spacing by two effects associated with electron-electron interaction: an upward shift for CDE by the direct coulomb interaction and a downshift for SDE by the exchange interaction. Moreover, due to polarization selection rules, it is possible to separate the charge density excitation and the spin density excitation in different spectra, using different scattering geometries.

In 1978 Burnstein proposed the possibility to observe electronic excitations in a 2-dimensional systems, under resonant conditions [140]. For the first time in modulation-doped GaAs-AlGaAs heterostructures, the Raman scattering lines by 2 dimension electron system were observed [141, 142]. Fig. 4.4 [143] shows spectra of modulation doped GaAs-$Al_{0.18}Ga_{0.82}As$ super lattice quantum well. The well thickness were 204 Å and 202 Å. The inset shows the band bending of the conduction band and the subbands within the well. For this specific structure, only the lowest subband is occupied by carriers. The Raman scattering geometry for each spectrum is given by the Porto notation. The z direction corresponds to (001) normal to the plane, while x and y correspond to the (110) and (1-101$\bar{1}$0) respectively, both lying in the plane of the layers. Both spectra are recorded in back scattering geometry with light directed along z. Instead, the polarization of the light incident and scattered is different between the spectra. In z(y x)-z spectrum, with the incident and scattered light polarizations perpendicular to each other (polarized configuration), we observe a single peak. This is associated with the spin-flip intersubband transition (SDE) between the lowest subband 0 to the higher subband 1, labeled as E_{01}. In addition to the LO_1 and LO_2 phonons of AlGaAs, the depolarized spectrum z(xx)-z displays two more modes, labeled as I_- and I_+. These modes (I_- and I_+) are assigned to the coupled modes, resulting from the coupling between the LO phonon and the charge density intersubband transition (CDE) from subband 0 to subband 1. This is similar to the coupling between collective excitation of bulk electron plasma with the LO phonon in polar semiconductor.

As we stated, the energy excitations differ from the subband spacing for exchange interaction in case of SDE and for direct Coulomb interaction for CDE. Moreover, the coupling with the

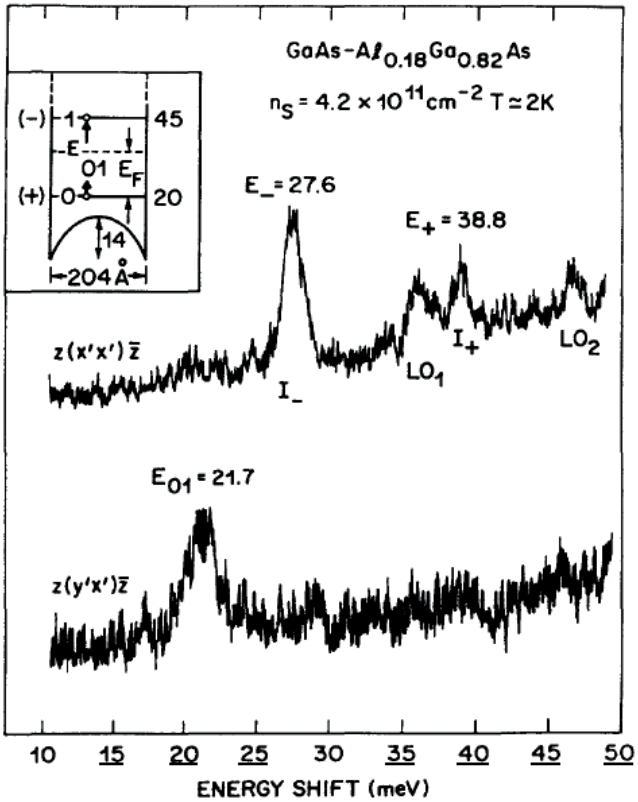

Figure 4.4 – Light scattering spectra of modulation doped quantum well GaAs-AlGaAs heterostructures. The lowest quantum-well states, the band bending and the fermi energy are showed in the inset. Reprinted from Ref. [143], Copyright (1980), with permission from Elsevier

longitudinal optical phonon with CDE is an additional contribution in changing the energy position of CDE. Because the exchange interaction effects are considered small, the SDE excitation is assumed to be the spacing between subbands. A quantitative analysis for the calculation of coupled modes energy have been used with success. Similar to the LO phonon plasmon coupled mode described in Sec. 2.7 for a 3Dimensional plasma, the coupling between collective intersubband excitations is determined by the dielectric function of the material. For example, we report the analysis of couple modes, I_- and I_+, shown in the depolarized spectra z(xx)-z of Fig. 4.4. Within this analysis, only the coupling with the lowest subbands transition excitations are considered, since the other subbands are well separated in energy.

The coupled mode energies $\omega_\pm$ are the solutions of :

$$1 - \left(\frac{\omega_{\mathrm{TO}}^2 - \omega_\pm^2}{\omega_{\mathrm{LO}}^2 - \omega_\pm^2}\right) \cdot \left(\frac{\omega_{\mathrm{P}}^2}{\omega_\pm^2 - \omega_{01}^2}\right) = 0 \tag{4.1}$$

where ω_{01} is the intersubband energy, ω_{TO} and ω_{LO} the TO and LO phonon frequency respec-

tively while ω_P is the effective plasma frequency, which has the form of:

$$\omega_P^2 = \frac{8\pi N_s e^2 \omega_{01} L_{01}}{\epsilon_\infty} \tag{4.2}$$

where N_s is the 2 dimension concentration of electrons. L_{01} is the matrix element of the direct Coulomb interaction of a length given by [144]:

$$L_{01} = \int_0^{d_1} dz \left[\int_0^z dz\prime \xi_1(z\prime)\xi_0(z\prime) \right]^2 \tag{4.3}$$

where $\xi_0(z)$ and $\xi_1(z)$ represents the envelope function of the two lowest states . The Coulomb matrix element L_{01} is the adjustable parameter. The value obtained from the analysis of the spectrum in Fig. 4.4 is 15 Å. This analysis, used in many studies of light scattering spectra [145, 146, 143], provides values of L_{01} in good agreement with those calculated by means of subband envelope function obtained from simple model calculation.

An interesting point is the relation of light scattering spectroscopy of intersubband excitations to electronic properties of 2 dimensional systems. Pinczuk et al. [147] have outlined a correlation between lineshapes in resonant light scattering spectra and the mobilities of 2Dimension electron system [147]. This study was carried out on four similar modulation-doping GaAs/AlGaAs quantum well with different spacer thickness, the distance between the dopants and the GaAs interface. As expected, Hall measurements showed an increase of mobility with the spacer thickness. They found a decrease of the widths of the intersubband transition observed from inelastic light spectra with the spacer thickness, and then with the mobility. This work represents an indication that inelastic light scattering can be used to characterize the electronic properties of modulation-doped GaAs/AlGaAs systems.

4.1.3 Nanowires with a modulation-doped structure

Inspired from the structures that led to record mobilities in planar III-V samples, modulation doping in nanowire radial heterostructures have been proposed. Fig. 4.5 shows the scheme of modulation doped nanowire radial heterostructures. A GaAs core nanowire is covered by an $Al_{1-x}Ga_xAs$ shell, which presents at certain distance from the core a δ Silicon layer. An additional GaAs capping layer is grown to prevent oxidation. Electrons coming from the Si impurities migrates to the lower energy potential of GaAs core.

Theoretical calculations were performed by Bertoni et al. [148]. Simulating the charge carrier distributions, they found different localization and symmetries of it in function of doping density and gate potential. In particular, the 1D electron channel formed at the edge of the

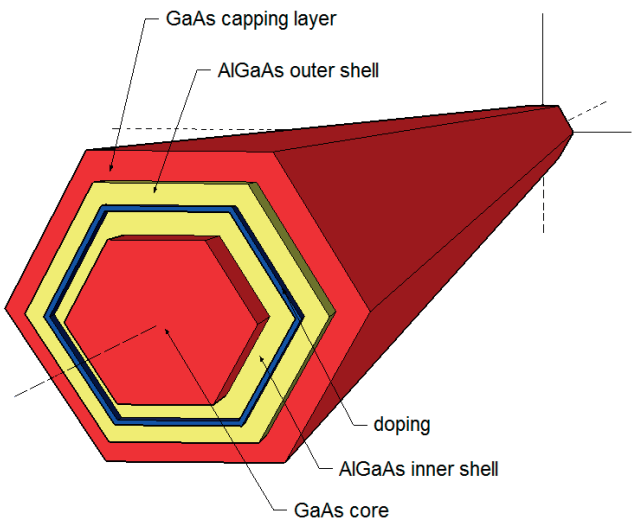

Figure 4.5 – Typical scheme of modulation-doped nanowires

core could give a better performance of such structure. For this reason, a great interest has been stimulated in the growth and characterization of them.

The doping in modulation-doping nanowire structures has been more challenging to realize than the one in layered samples, due to the inhomogeneous doping and compensation in (110) surfaces, which constitute the nanowire facets [149, 30]. In the last years, the growth of such structures have seen further progresses [150]. The assessment of the electron density and mobility is necessary for these structures. Contact-less techniques, such as Terahertz and Raman spectroscopy are suitable for the detection of electronic properties as electrical contacts are especially challenging in this kind of structure.

To the best of our knowledge, the use of Raman scattering to study modulation doping nanowires is only reported by Funk et al. [124]. They synthesized a different type of modulation doped core-shell nanowires as reported in Fig. 4.6. This structure presents a multishell, resulting in the confinement of electrons in the hexagonal-shaped coaxial quantum wells in the shell, and not in the core as for the typical modulation-doped. Since in such a structure electrons are confined in a quantum well, we can suppose they have lower mobility than electrons confined in the core of the typical structure depicted in Fig. 4.5. Indeed, we know that the mobility limited by interface scattering is predicted to be higher in a triangular shaped quantum well formed by AlGaAs/GaAs single heterojunction, as in the case of the confinement in the core, than in a square-shaped quantum well formed by AlGaAs heterojunction, as for the multishell nanowire structure [151].

Fig. 4.6 shows the density distribution of electrons, as obtained from self-consistent simulations by Funk et al. [124]. These simulations show a two-dimensional confinement at the facets and a one-dimensional at the corner. Authors performed polarized resonant inelastic light scattering measurements on modulation doped and the correspondent undoped structures.

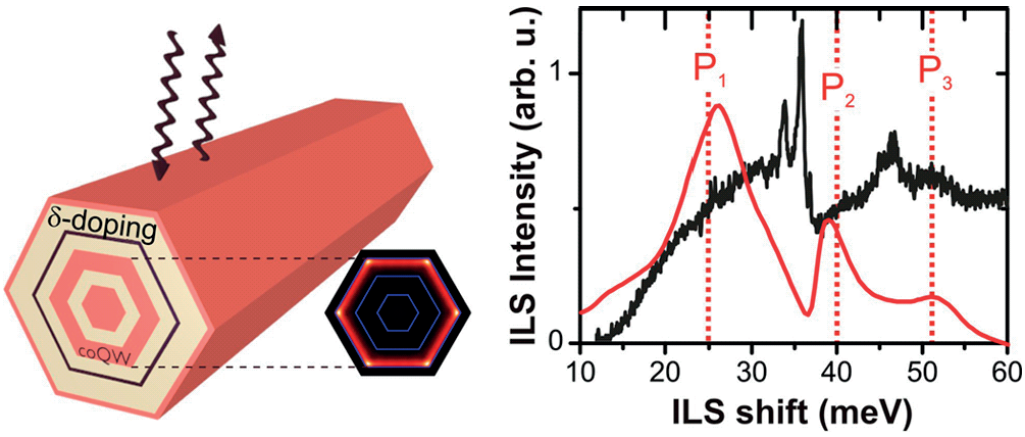

Figure 4.6 – Structure of the modulation doped core-multishell GaAs-AlGaAs with the distribution of electrons in the quantum well shell. Inelastic light spectrum of a single modulation doped multishell nanowires in the polarized configuration and calculations of Spin Density Excitations. Reprinted with permission from Ref. [124], Copyright 2013, American Chemical Society.

The two different back-scattering geometries used in the work were the polarized geometry (polarization of light incident parallel to the nanowire axis and the polarization of the light scattered perpendicular to it), and the depolarized one (polarizations of light incident and scattered both parallel to the nanowire axis).

Compared with undoped nanowires, Funk et al. observed additional broad features in both the polarized and the depolarized spectra. Fig. 4.6 shows the spectrum obtained in the polarized configuration for modulation doped structure. In this case, authors associated the broad peaks observed in the polarized spectrum to the spin density excitations, whereas the peaks observed in the depolarized spectrum were linked to the charge density excitations. They also performed calculations of the energies and intensities of SDE and CDE, by considering them as transitions from occupied to unoccupied subband states. Funk et al. conclude their work, by presenting the best match between simulations and data of the SDE and CDE, represented for SDE by the red line in the graph of Fig. 4.6, which is used to estimate the carrier density and the mobility.

However, though the work produced by Funk et al. is qualitative respectable, it is my opinion that the conspicuous mismatch between the simulations and data shown in Fig. 4.6 cannot provide a reliable quantitative evaluation of carrier density and mobility.

Moreover, Boland et al. [42] presented first Terahertz measurements on modulation doped nanowires, found a higher lifetime for modulation-doped sample respect to GaAs. Here, we compare electronic properties of GaAs-$Al_{1-x}Ga_xAs$ radial heterostructures nanowires with the corresponding n-type modulation-doped nanowires by LO phonon-plasmon coupled modes Raman scattering. The modulation-doped sample is the same investigated by Boland et al. [42].

4.1.4 Simulations

In order to design the structure of the nanowires, we have simulated the electron density of modulation doped structure by solving Poisson and Schrödinger self-consistently calculations with the software nextNano. Fig. 4.8 shows the electron density as a function of doping layer. At low doping level ($2 \cdot 10^{18}$ cm^{-3}), the electron distribution is homogeneous in the core. Increasing the doping, the electrons show localization effect. In particular, at higher doping level, charges have an isotopic cylindrical distribution, with a localization at GaAs/$Al_{1-x}Ga_xAs$ interface. At highest doping level ($7{\cdot}10^{18}$ cm^{-3}), a 6-fold symmetry 1D gas at the core hexagonal edges is observed. The absolute value of electron density also increases with the doping concentration. In order to have a density concentration of $\sim 10^{17}$ cm^{-3}, a doping concentration of $5 \cdot 10^{18}$ cm^{-3} is necessary.

Ketterer et al. [30] showed that compensation effects affect doping concentration of $< 3 \cdot 10^{18}$ cm^{-3}, limiting the free carrier concentration. Another parameter that changes the electron density is the the distance (d) between the doped layer and the GaAs/$Al_{1-x}Ga_xAs$ interface. We have to consider that increasing this distance a high mobility could be reached, but a decrease in carrier concentration occurs. To balance this effect, a distance of 15 nm is used [138].

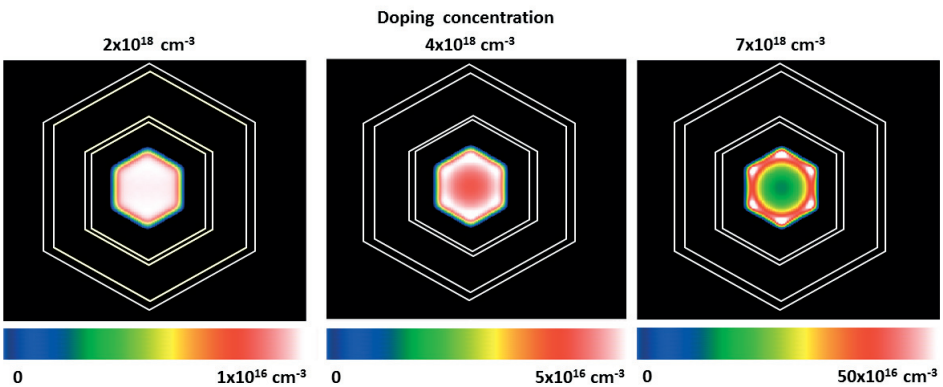

Figure 4.7 – Simulation of the electron density in modulation nanowires with a doping concentration of $2{\cdot}10^{18}$ cm^{-3}, $4{\cdot}10^{18}$ cm^{-3} and $7{\cdot}10^{18}$ cm^{-3}.

4.1.5 Experimental

The GaAs-$Al_{1-x}Ga_xAs$ radial heterostructures nanowires were grown using an MBE machine with vapor-liquid-solid mechanism for the core and vapor-solid mechanism for the shell. Vertical GaAs nanowire grown on a p-type Si wafer presents a diameter of 50 nm. Then, a 40 nm of $Al_{0.33}Ga_{0.67}As$ is grown around the GaAs core. Finally, the shell is capped with 5 nm of GaAs layer to prevent the oxidation of the wire in air. Modulation-doped nanowire presents a silicon doping layer at a distance of 12 nm from GaAs/AlGaAs interface, with $4{\cdot}10^{18}$ cm^{-3} dopant density. With this structure, simulations show that electron density is in a three

dimensions regime (fig. 4.8).

Raman scattering measurements are performed in back-scattering geometry configuration under 520.8 nm excitation wavelength laser. The laser beam with a power of 200 μW was focused through an objective of N.A. 0.75 on the growth sample with free-standing nanowires. Measurements at different temperature of the sample are performed using a temperature controlled helium cryostat. Details of the set-up for Raman experiments can be found in Section § 2.8. The polarization of the incident light, which is perpendicular to the NW axis, is controlled, whereas the polarization of the scattered light, which is in the same plane, is not investigated. According to Raman selection rules, in the back-scattering configuration from a {111} face of a zincblende crystal (up-configuration) both transverse and longitudinal optical modes are allowed, even if the TO mode is more pronounced than the LO one. The intensity of TO and LO modes are independent on the incident polarization.

4.1.6 Results

Fig. 4.8 shows spectra of modulation-doped and undoped GaAs-$Al_{1-x}Ga_xAs$ radial heterostructures nanowires recorded at room temperature and at 14 K. We remind that Raman spectra of $Al_{1-x}Ga_xAs$ show a two mode behavior, (see Section § 2.2) with two different set of modes, GaAs-like and AlAs-like modes. In the spectral range reported here, we identify peaks related to the pure GaAs (TO and LO) and the GaAs-like peaks (TO and LO) of the shell. The four spectra present significant differences. We distinguish difference in the frequency position and in the relative intensities of the peaks.

We start by reporting the differences of the spectra recorded at different temperature. In the spectra at low temperature, the most dominant peaks are the GaAs TO and GaAs-like TO and LO phonon modes, respectively at 269 cm^{-1}, 263 cm^{-1} and 280 cm^{-1} . The alloy related peaks exhibit a broad nature, due to the alloy disorder. In addition, we find the contribution of the GaAs LO peak at 293 cm^{-1}. The spectra at room temperature is dominated only by GaAs TO mode at 264.5 cm^{-1}.

At first glance, we observe that the peaks shift to lower energies respect to the spectrum of lower temperature. This is a common mark when decreasing the temperature and is a signature of the variation in lattice parameter. We can also observe differences in intensity between the GaAs TO mode and $Al_{1-x}Ga_xAs$ related modes: for low temperature the relative intensities of the shell for spectrum recorded at low temperature is higher than the one at room temperature. This can be explained with the fact that decreasing the temperature, the band-gap of $Al_{0.33}Ga_{0.67}As$ is approaching the near resonance condition with the 520.8 nm wavelength.

We turn now to the differences due to the presence or not of doping in the shell. The presence of doping affects only the spectra at higher temperatures. We can observe a decrease and a broadening of the GaAs LO mode for the spectra of modulation-doped nanowire. The

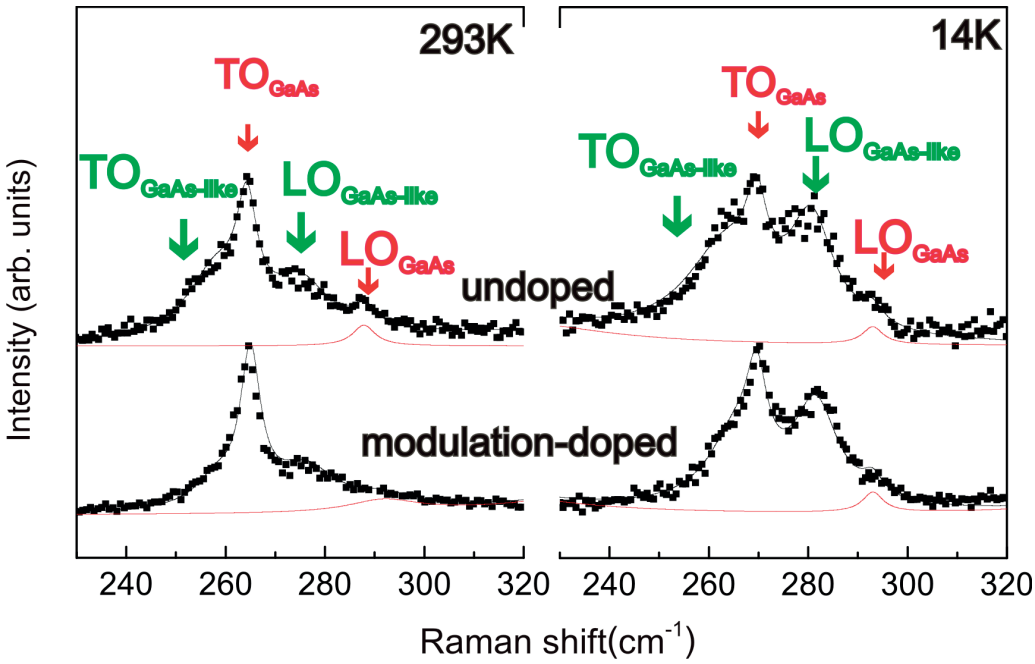

Figure 4.8 – Raman spectra of un-doped and modulation-doped nanowires recorded at 14 K and at room temperature.

decreasing of the LO phonon peak can be attributed to the LO phonon-plasmon coupled mode due to the presence of carriers. In bulk material, for n-type GaAs material two different coupled modes are expected. In order to explain the absence of the low frequency coupled mode, we have to consider a relevant reduction of the electron mobility for the material in nanowire form. At low electron mobilities in n-GaAs, similar spectral features, i.e. only one damped coupled mode, is expected as in p-type GaAs material [152].

We calculate the Raman line shapes by using the fluctuation-dissipation formalism of Hon and Faust and the Drude model (see Section § 2.7 and Subsection § 3.4.4 for details), with the aim to evaluate the carrier concentration and the mobility. Then, the calculated Raman lineshapes are fitted to the experimental Raman spectra. For the TO of GaAs and the alloy-related peaks, a Lorentzian profile is used. For the fit, the input parameter depending on the temperature (phonon frequency and phonon damping constant) are taken from Ref. [153] and the carrier concentrations N_e and the electronic damping constant Γ_e, both of which enter the electric susceptibility of the electron gas, are taken as free parameters.

In Fig. 4.9 and Fig. 4.10, we plot the electron concentration and the mobility extracted from the fits as a function of the temperature. The observed temperature dependence of electron concentration for modulation doped nanowires exhibit an abrupt increase beyond 14 K, followed by a less sharp increase from 50 to 293 K. Contrarily, the electron concentration of the undoped nanowires slightly increases within all the range of temperature, even if its value is lower than the modulation doped-sample. The increase of the carrier concentration for

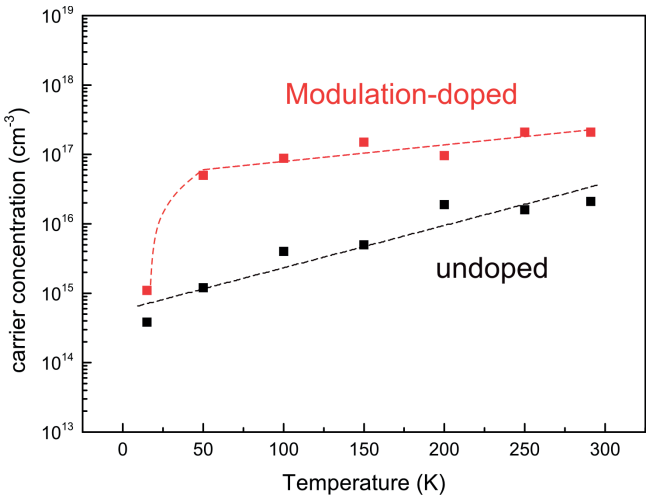

Figure 4.9 – The evolution with temperature of the electron concentration of undoped and modulation-doped nanowire extracted from the Raman fits.

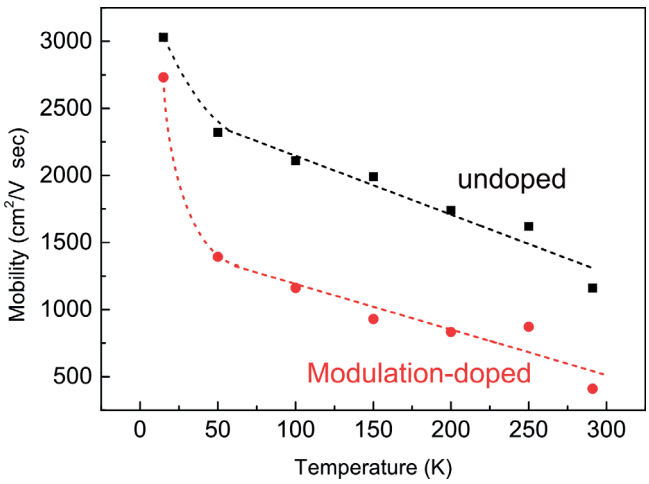

Figure 4.10 – The evolution with temperature of the electron mobility of undoped and modulation-doped nanowire extracted from the Raman fits.

modulation-doping sample at low temperature is due to the temperature-induced ionization of dopants atoms in $Al_{0.33}Ga_{0.67}As$ shell. The high value of carrier density respect to the expected intrinsic one for the undoped sample could be explained by the lightly presence of spurious impurities.

Fig. 4.10 shows the evolution of the mobility in function of the temperature for the undoped and doped nanowires. For both the samples, the mobility decreases moving from low to high temperature. At 14 K the mobility of modulation-doped nanowire is comparable with the undoped one. Then, we can observe an abrupt decrease in the mobility at 50 K for modulation doped nanowire with increasing temperature. On the contrary, the mobility of the undoped nanowire does not show a transition, and decreases slightly. Among the scattering

mechanisms, the phonon scattering gives rise to a decrease of mobility with the temperature. However, the low mobility found here cannot be explained by this typical bulk scattering effect.

Interestingly, we observe a decrease of mobility in function of carrier concentration, which could suggest that the main scattering mechanism is linked to carrier-carrier interaction. However, the low mobility recorded at low temperature indicates that the scattering at interface of this structure plays a role in the degradation of the electron mobility. Moreover, we can consider that the band-edge profile changes with the temperature. This gives rise to a change of the density-distribution inside the core. We have performed simulations of electron-density profile at different temperatures.

Fig. 4.11 shows the line-scan of the simulated electron density distribution for different temperatures. In addition to an increase of the carrier concentration, we observe a shift of the density-distribution from the center of the core to the edge at increasing temperature. This leads to higher possibility of the scattering with the interface, and could result in a decrease of the mobility with the temperature.

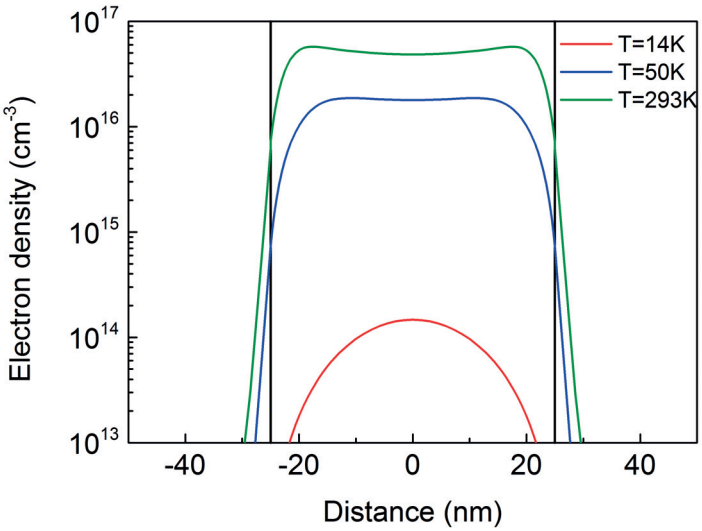

Figure 4.11 – Horizontal linescan of the electron density distribution through the nanowire center for different temperature, assuming a nominal doping concentration of$4 \cdot 10^{18}$ cm^{-3} and an activation energy of 6 meV. [154]. The vertical lines represent the GaAs/AlgaAs interfaces.

4.2 InAs-InAsSb nanowires

4.2.1 Introduction

As we stated in the Introduction chapter, III-V nanowires are suitable candidates for the future electronics, optics and quantum devices [155, 156]. Among them, InAs nanowires have attracted particular interest due to their properties, such as small band-gap and high mobility [157, 158]. Nanowires can grow either in zinc-blende either in wurtzite structures or, more often, in a mixture of the two. The presence of different polytytes modify the electronic properties [159, 160, 161]. Pure ZB or WZ phases InAs nanowires can be grown using gold as catalyst [162, 163]. To avoid metal contamination, a gold-free growth is desirable [164, 165]. The incorporation of Sb could represent one pathway to achieve highly uniform nanowires [166, 167, 168]. The presence of Sb could change the electronic properties of nanowires. Here, we use Raman spectroscopy by LO-phonon plasmon coupled mode to study the effect of antimony on the electronic properties of $InAs_{1-x}Sb_x$ nanowires.

4.2.2 Raman scattering by LOPPCM in InAs and $InAs_{1-x}Sb_x$ bulk material

After the discovery of LO phonon-plasmon coupled mode (LOPPCM) By Mooradian and Wright [31], many studies are reported on this interaction in n-type and p-type GaAs. Literature on Raman scattering by LO phonon-plasmon coupled modes is less frequent in InAs. First Raman results were reported by Patel and Slusher [169] for n-InAs sample. They observe the low frequency coupled mode branch below the LO phonon mode. Raman studies on n-InAs were extended by Buchner and Burnstein [170] to higher carrier concentration. They were able to observe only one mode in the range between LO and TO mode,as shown in Fig. 4.12. Only later, Li et al. [171] could observe also the presence of the high frequency mode in n-type InAs sample with carrier concentration up to $4 \cdot 10^{19}$ cm^{-3}.

To the best of our knowledge, no reports of LOPPCM scattering in $InAs_{1-x}Sb_x$ exist. However, Raman scattering by coupled modes are widely studied in other different ternary alloys [172, 173, 174, 175, 176]. As explained in Sec. § 2.2, usually III-V ternary alloy shows the two-mode behavior, with two set of optical phonon frequencies close to the ones of the sublattices. This is also the case of $InAs_{1-x}Sb_x$ [177]. We also show the two-mode behavior of phonon modes for a ternary alloy. In presence of carriers, the presence of two longitudinal phonon modes gives rise to an additional coupled mode (L_0) in addition to the low ($L-$) and the high ($L+$) frequency modes. This could be observed in Fig. 4.13, where three modes are observed in $Al_{1-x}Ga_xAs$ [172]. The character of these modes depends on the carrier concentration. As for the binary compounds, at low concentration regime $L-$ has a plasmon-like character and $L+$ a phonon-like one. In the opposite limit, they present a reversed character. Contrarily L_0 is confined between the frequency gap of the two optical phonon branches and it has plasmon-like character in both limits, i.e. high and low carrier concentration. It presents plasmon-like behavior only when it exhibits a frequency close to the plasmon.

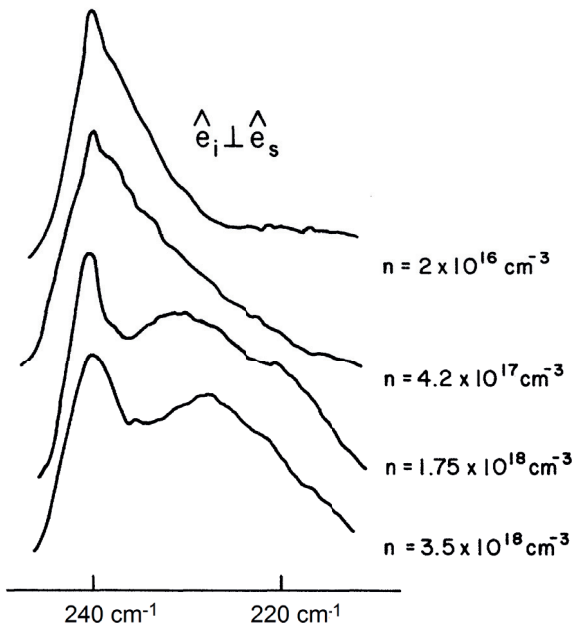

Figure 4.12 – Raman spectra in back scattering geometry of n-type (100) InAs with different doping concentration. Reprinted figure with permission from Ref. [170]. Copyright (1974) by the American Physical Society.

4.2.3 Theory of LO phonon plasmon coupled mode in a ternary alloy

We turn now to the description of the theory of coupling of the longitudinal optical modes with plasmon for binary compounds. For ternary alloy, the Raman cross-section from Coupled-modes scattering has to consider the contribution of the two different sublattices. Considering the standard dielectric theory in the formalism of Hon and Faust [129], the differential Raman cross-section from coupled phonon-plasmon modes of a doped two mode ternary alloy $A_xB_{1-x}C$ has the form [116]:

$$\begin{aligned}\frac{\partial^2\sigma}{\partial\omega\partial\Omega} \propto\ & (n_\omega+1)\Im\left\{\frac{-1}{\epsilon(\omega,x)}\left[\frac{1}{4\pi}+2\frac{A_1}{\epsilon_{\infty,1}}\chi_1(\omega,x)+2\frac{A_2}{\epsilon_{\infty,2}}\chi_2(\omega,x)\right.\right.\\ & -4\pi\left(\frac{A_1}{\epsilon_{\infty,1}}-\frac{A_2}{\epsilon_{\infty,2}}\right)^2\chi_1(\omega,x)\chi_2(\omega,x)\\ & \left.\left.-\left(1+\frac{4\pi}{\epsilon_\infty(x)}\chi_e(\omega)\right)\epsilon_\infty(x)\left[\left(\frac{A_1}{\epsilon_{\infty,1}}\right)^2\chi_1(\omega,x)+\left(\frac{A_2}{\epsilon_{\infty,2}}\right)^2\chi_2(\omega,x)\right]\right]\right\}\end{aligned} \tag{4.4}$$

where n_ω is the Bose-Einstein distribution, $\epsilon(\omega,x)=\epsilon_{\infty(x)}+4\pi(\chi_1(\omega,x)+\chi_2(\omega,x)+\chi_e(\omega))$ is the dielectric function of the alloy, with $\epsilon_\infty(x)=x\epsilon_{\infty,1}+(1-x)\epsilon_{\infty,2}$ the average high-frequency dielectric function, $\chi_i(\omega,x)=x_i\frac{\epsilon_{\infty,i}}{4\pi}\frac{(\omega^0_{LO,i})^2-(\omega^0_{TO,i})^2}{(\omega^2_{TO,i}-\omega^2-i\omega\Gamma_i)}$ the i-sublattice contribution to the sus-

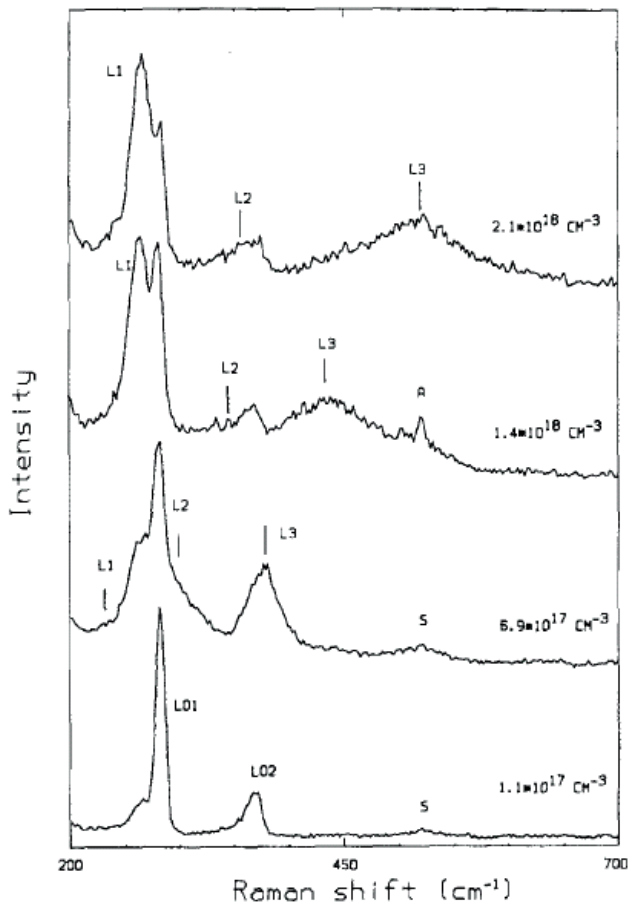

Figure 4.13 – Raman spectra of n-type $Al_{1-x}Ga_xAs$ with x= 0.75. The three coupled mode are labeled with L1, L2 and L3. The LO GaAs-lke and AlAs-like are labeled with L01 and L02, respectively. Reprinted from Ref. [172], with the permission of AIP Publishing.

ceptibility, where Γ_i is the phenomenological damping constant, $\omega^0_{TO,i}$ and $\omega^0_{LO,i}$ are the frequencies of TO and LO modes of the pure end-member compounds, whereas the $\omega_{TO,i}$ is the TO phonon frequency of the alloy i-sublattice, χ_e is the electronic susceptibility contribution, and $A_i = C^0_i \frac{\omega^2_{TO,i}}{(\omega^0_{LO,i})^2-(\omega^2_{TO,i})^2}$ with C^0_i being the Faust-Henry coefficient for the pure member compound.

We calculate the electronic susceptibility using the Hydrodynamical model [60]:

$$\chi_e = -\frac{\epsilon_\infty}{4\pi}\frac{\omega_p^2}{\omega^2 - \langle v^2\rangle q + i\omega\Gamma_e} \tag{4.5}$$

where ω_p is the plasma frequency ($\omega_p^2 = \frac{4\pi}{\epsilon_\infty}\frac{Ne^2}{m^*}$), Γ_e is the damping constant related to the lifetime of the plasmon,$\langle v^2\rangle$ the electron mean square velocity and q the wavevector. Considering

the low band gap energy of InAsSb, we expect that the non-parabolicity of the conduction band is not negligible. For this reason, we use the Kane two-band model to calculate the electronic dispersion [60]:

$$E(k) = \frac{E_G}{2}\left[\sqrt{1+\frac{4}{E_G}\frac{\hbar^2 k^2}{m^*}}-1\right] \tag{4.6}$$

We summarized the input parameters for the LOPCM line-shape model discussed above for $InAs_{1-x}Sb_x$ with $x = 0.35$, in Table 4.1.

Table 4.1 – Input parameters for the LOPCM line-shape model for $InAs_{0.65}Sb_{0.35}$. [a] Present work; [b] Reference [171]; [c] Reference [116]; [d] Reference [178];

Symbol	Description	Value
$\omega^0_{LO,InAs}$	LO,InAs	235 cm^{-1}[a]
$\omega^0_{TO,InAs}$	TO,InAs	214 cm^{-1}[a]
$\omega^0_{LO,InSb}$	LO,InSb	191 cm^{-1}[b]
$\omega^0_{TO,InSb}$	TO,InSb	180 cm^{-1}[b]
$\omega_{TO,InAs}$	TO,InAs-like	211 cm^{-1}[a]
$\omega_{TO,InSb}$	TO,InSb-like	180 cm^{-1}[b]
Γ_{InAs}	InAs phonon damping constant	4 cm^{-1}[c]
Γ_{InSb}	InSb phonon damping constant	12 cm^{-1}[c]
C^0_{InAs}	InAs Faust-Henry coefficient	-0.61[c]
C^0_{InSb}	InSb Faust-Henry coefficient	-0.36[c]
$m^*(x)$	electron effective mass	0.023-0.039x+0.03x^2[a]
$\epsilon_{\infty,InAs}$	InAs high-frequency dielectric constant	12.2[c]
$\epsilon_{\infty,InSb}$	InSb high-frequency dielectric constant	15.7[c]
$E_G(x)$	Energy bandgap	$0.41-\frac{3.410^{-4}T^2}{210+T}-0.876$ V+ $+0.70x^2+3.4*10^{-4}xT(1-x)$ eV [d]

The position of the coupled modes depends not only on the carrier density and the mobility but also on the alloy concentration (x). In Fig. 4.14 the maxima of the Raman lineshapes of coupled mode are plotted versus the concentration of electrons fixing the x=0.35 and the mobility at 14000 $cm^2/(Vs)$. The graph shows the trend of the high, middle and low frequency modes as a function of the concentration of electrons.

4.2.4 Experiment

Raman measurements are performed both on pristine and Al_2O_3 coated $InAs_{1-x}Sb_x$ nanowires. $InAs_{1-x}Sb_x$ nanowires studied here are grown vertically with a catalyst-free growth process. In order to obtain $InAs_{1-x}Sb_x$ nanowires with different Sb concentration, the antimony flux is changed meanwhile the rest of the growth parameters are taken constant. Details of the growth process are reports in the paper of Potts et al. [179]. Increasing Sb concentration, nanowires

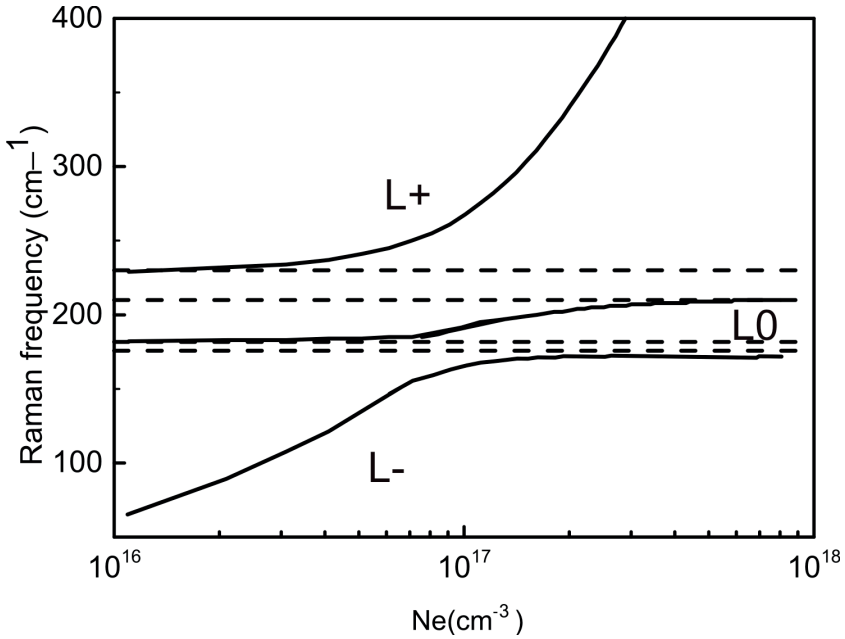

Figure 4.14 – Coupled-modes frequencies versus electron density in $InAs_{1-x}Sb_x$ with x =0.35. The dotted lines indicate the frequencies of InAs-like and InSb-like TO and LO modes.

showed an increase of the diameter and a decrease of the length. Moreover, regarding the crystal structures, an increase of antimony showed a significant decrease in the density of defects. Raman measurements were done using the 488 nm line of Ar-Kr+ for excitation. The laser with power of 250 μW was focused on each nanowire with a microscope objective with numerical aperture N.A.=0.75. The scattered light was collected by a TriVista spectrometer and detected by a CCD camera. The measurements were realized in back-scattering geometry with the nanowires suspended over a trench, in order to enhance the response of the longitudinal optical phonon mode [180]. The temperature measurements are performed using a temperature controlled helium cryostat.

4.2.5 Effect of Sb concentration

Fig. 4.15 shows the Raman spectra of pristine InAs and InAsSb with different percentage of antimony nanowires. In the spectra, LO and TO phonons frequencies, as well as the SO (surface optical modes) typically detected in nanowires, are indicated. In the case of InAs, TO and LO modes of zinc-blende phase are present, and no modes related to wurtzite crystal phase are observed. In the case of InAsSb, the position of the TO and LO modes are consistent with the composition, and follow a two mode model of ternary alloys. Raman modes of InAs and InSb are present, being the position and intensity weighted by the composition.

The Raman spectra show additional spectral features in the LO region for the InAs and in the InAs-like TO mode region for $InAs_{1-x}Sb_x$, which are not related to the composition, crystal

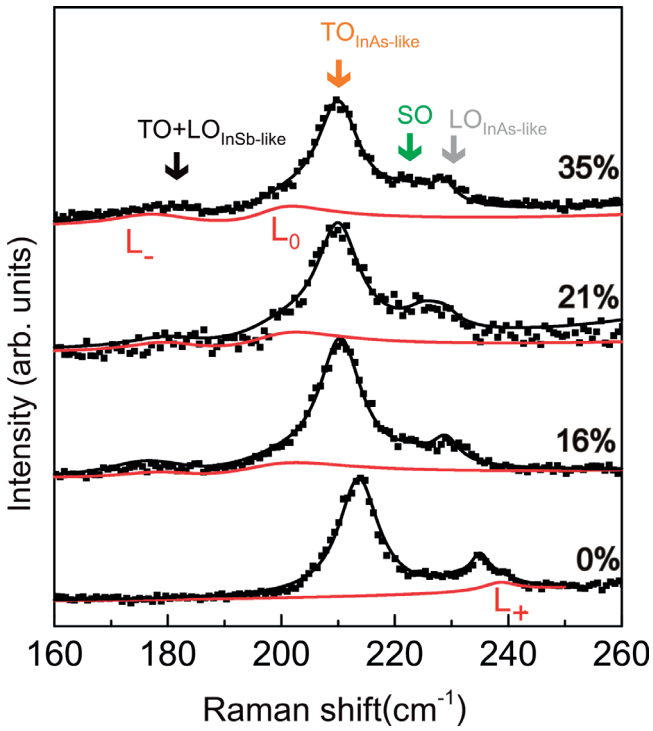

Figure 4.15 – Raman spectra of $InAs_{1-x}Sb_x$ nanowires for x=0, 0.16,0.21 and 0.35. Black lines show the convolution of the ternary modes with a Lorentzian profile and the coupled modes lineshape obtained by fitting the model. Red lines show the coupled modes obtained by the fitting.

phase, or shape of the nanowires. We attribute these additional peaks to the interaction of the carriers with the polar phonons. With free carriers, the unscreened LO mode and plasmon mode are replaced with coupled modes with mixed character. The coexistence of the peak at the LO phonon frequency and the coupled modes is observed in bulk material [181]. The peak LO-phonon frequency is associated from scattering of unscreened LO phonon in the low-density carrier area, usually the depleted region near the surface. Contrarily, the coupled modes originate from the region where the carrier concentration reach the bulk value.

The frequency position and the width of the coupled modes are related to the plasmon (carrier) density and the lifetime (mobility). We fitted the whole spectra by modeling both the modes related to the composition and to the presence of free carriers. A Lorentzian profile was used for the TO and LO modes, whereas the line shape of the coupled modes included the effect of damping (mobility) with the model described above. The electron concentration and the mobility extracted from the fits are reported in Fig. 4.16 versus the concentration of antimony. In general, the mobility and of the carrier concentration are found to be higher for antimony containing wires.

In order to understand the origin of the carriers and the region where carriers are present, a study as a function of the temperature and as a function of passivation with Al_2O_3 is performed.

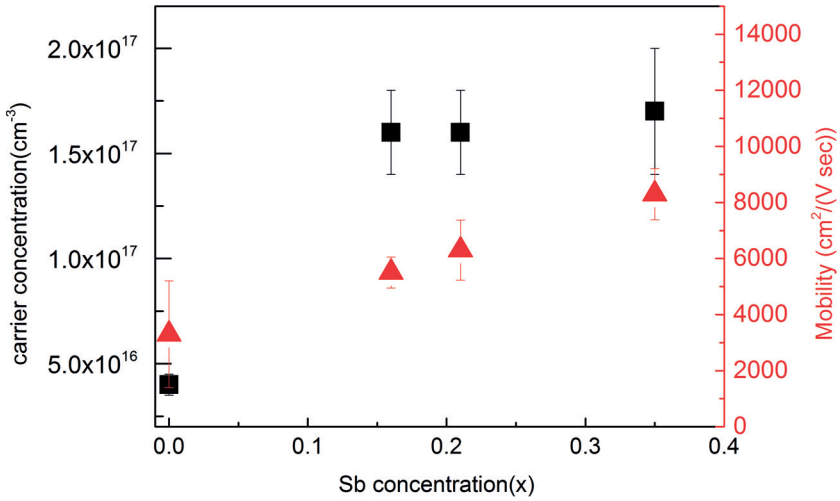

Figure 4.16 – Electrons concentration and mobility extracted from the fits of the Raman lineshapes of coupled modes at room temperature for $InAs_{1-x}Sb_x$ (cf. Fig. 4.15). The error in the mobility is the fitting error, instead the error in electrons concentration is calculated by using the experimental error(1 cm^{-1})

4.2.6 Effect of the temperature

Fig. 4.17 shows normalized Raman spectra of InAs and $InAs_{1-x}Sb_x$ with x=0.35 recorded at temperature in the range between 14-293 K range. At first glance, we observe that the different modes broaden and shift to lower frequencies as temperature increases. It is expected that with the temperature Raman shift, width and intensities vary. The common mark when increasing the temperature are the broadening and the shift of Raman lines: for Stokes scattering a blue shift is expected and a red shift for Anti-Stokes lines [182]. The anharmonic forces in the crystal lattice and the thermal expansion of it can explain this effect.

In the spectra, we observe also the features associated with the presence of carriers for all the temperatures both for InAs and $InAs_{1-x}Sb_x$ with x=0.35. The coupled modes also change their position and width with the temperature. In order to discriminate the effect of the temperature in the Raman scattering itself with the changes of the carries and mobility as a function of the temperature, the model presented above is used. The input parameters depending on the temperature, i.e. phonon frequencies and ionic damping constant, are taken into account.

The carrier concentrations as function of the temperature are plotted in Fig. 4.18 for InAs and $InAs_{0.65}Sb_{0.35}$, respectively nanowires.

As we can observe, the carrier concentration in InAs and $InAs_{0.65}Sb_{0.35}$ nanowires was almost constant within the range of temperatures, even if it differs by one order of magnitude between the two samples. As a consequence, impurities or surface states, from which carriers come

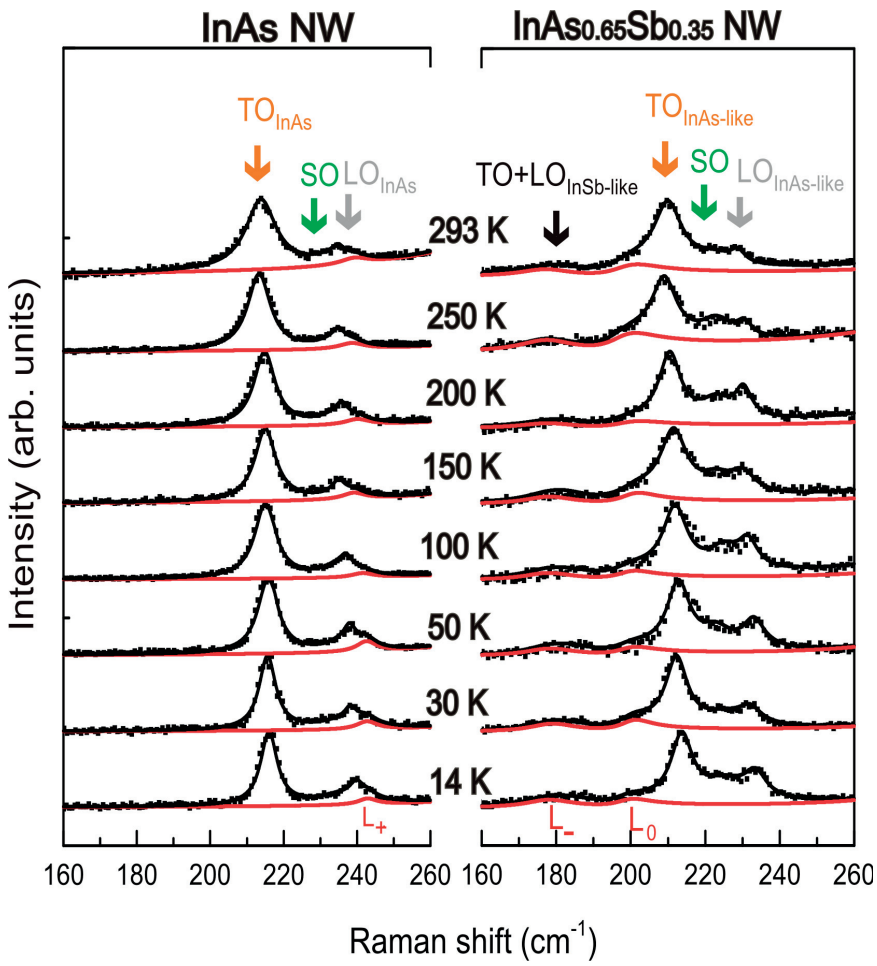

Figure 4.17 – Raman spectra of InAs and $InAs_{1-x}Sb_x$ with x=0.35 recorded at temperature in the range between 14 K and 293 K.

from, are completely ionized. The temperature dependence of mobility is also reported in Fig. 4.18. InAs nanowire shows a characteristic temperature dependence of mobility. It initially increases, reaching the maximum at ~ 50 K and then gradually decreases. Contrarily $InAs_{0.65}Sb_{0.35}$ nanowire shows a negative slope within the all range of temperatures.

4.2.7 Effect of surface passivation

Fig. 4.19 shows a comparison of the Raman spectra obtained on alumina coated and uncoated InAs and $InAs_{0.65}Sb_{0.35}$ nanowires at temperature of 14 K and 293 K. At first sight, we can observe a downshift of the surface optical modes respect to the uncoated modes. In fact, SO mode position depends on the dielectric constant of the medium surrounding the wires and the diameter.

For $InAs_{0.65}Sb_{0.35}$ nanowires, the spectra do not show any other differences. Both samples

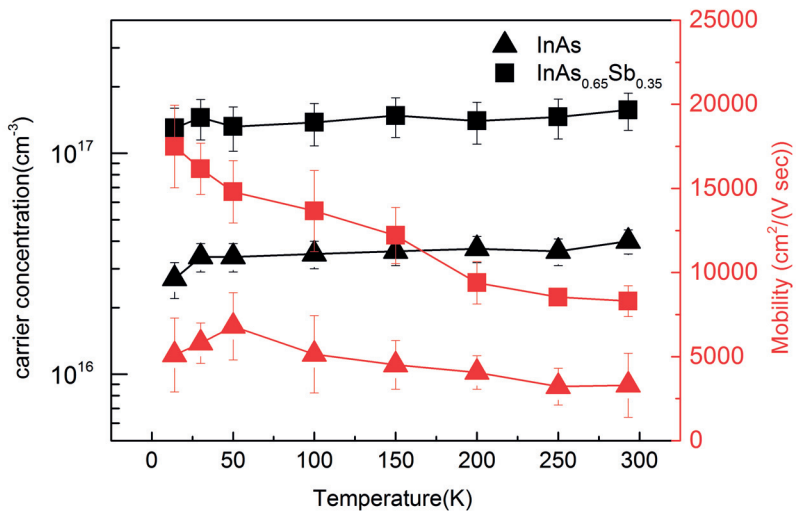

Figure 4.18 – Electron concentration and mobility extracted from the fits of the Raman lineshapes of coupled modes reported in Fig. 4.17 for different temperature for InAs and $InAs_{0.65}Sb_{0.35}$.

exhibit a similar concentration and mobility of the electrons, as reported in Fig. 4.20. For InAs nanowires, in addition to the shift of the SO position, we observe that the high frequency coupled mode disappears. This peak is not visible also outside the range reported here. This suggests that a decrease of carriers occurs.In fact at lower concentration of carriers, coupled modes are not detected in Raman spectra.

4.2.8 Discussion: origin of carrier and scattering mechanism

We interpret the presence of the unscreened LO mode and the coupled modes, in both InAs and $InAs_{1-x}Sb_x$ nanowires, with the existence of two regions. A first region with low carrier concentration is responsible of the unscreened LO mode. The second region, with higher carrier concentration, is related to the existence of LOPPCM. Considering the geometry of the nanowire, naturally we can suppose that the two regions consist of the inner part (the core) and the outer part (the shell) of the wire.

The trend of the mobility, together with the effect of the capping, can give information to discriminate from which region the carriers are originated. In general, considering the decrease of the effective mass for InSb with respect to InAs, the increase of the mobility with percentage of antimony content is expected, and it is in agreement with field-effect transistor device measurements [160, 179].

We move now to the discussion of the origin of the carrier and the scattering mechanism for InAs nanowires. For pristine InAs nanowires, the fits of the coupled modes of the spectra

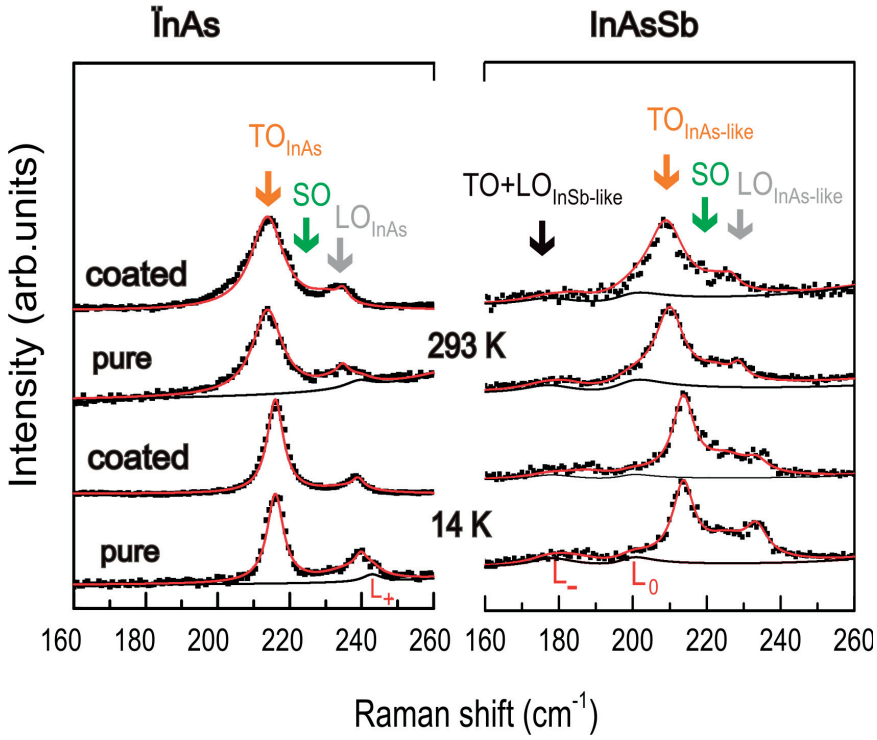

Figure 4.19 – Raman spectra of InAs and $InAs_{1-x}Sb_x$ with x=0.35 pure and coated with Al_2O_3, recorded at temperature of 14 and 293 K.

recorded at room temperature allowed us to estimate a carrier concentration of $3.9 \cdot 10^{16}$ cm^{-3}. This value is higher than the intrinsic carrier concentration of the material. Instead, for the mobility, we found 3300 $cm^2/(Vs)$, which is value lower than the mobility expected in the bulk.

From Raman measurements as a function of the temperature, we observe a slight decrease of the concentration with the decrease of the temperature. On the contrary, mobility increases with a temperature for temperatures below ~ 50 K, whereas a decrease of the mobility with the temperature is found above ~ 50 K . The dual behavior of the mobility as a function of the temperature is in agreement with other reports for InAs nanowires [183]. Contrarily, nanowires covered with Al_2O_3 do not exhibit the coupled mode, indicating a possible decrease of carrier density.

The interpretation of the results is based on the actual knowledge presented in the literature. In bulk material, InAs presents an accumulation layer at the surface, due to the Fermi level pinning. It is known that Fermi level pinning occurs in oxide free polar (100) and (111) InAs surfaces [184]. Dangling bonds at the surface act as donor states. Contrarily, no Fermi-pinning exists for (110) InAs surface without a native oxide [184].

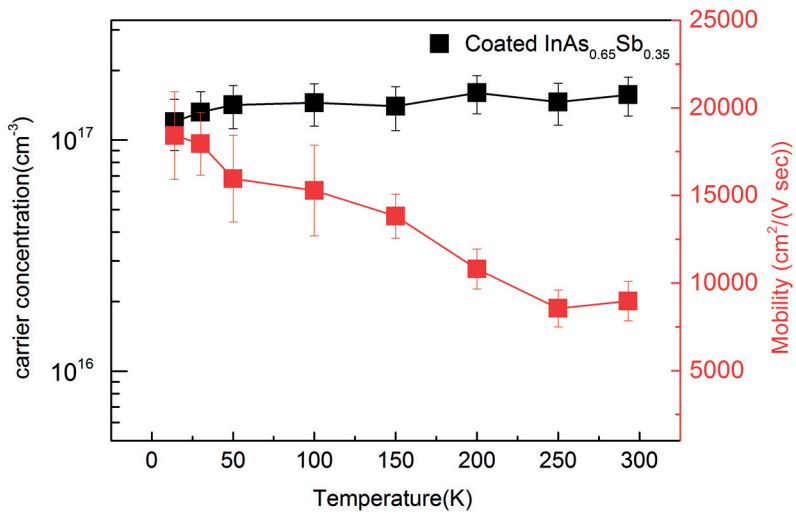

Figure 4.20 – Electron concentration and mobility extracted from the fits of the Raman lineshapes of coupled modes reported in Fig. 4.17 for different temperature for InAs and $InAs_{0.65}Sb_{0.35}$ coated with Al_2O_3.

However, a native oxide film is usually formed on the surface of the nanowire. For a native oxide (110) surface, the presence of a Fermi level pinning has been shown [185, 186]. It is related to the creation of donor states due to the preferentially formation of arsenic-oxygen bonds. Moreover, it is shown that electrons in the accumulation layer have higher concentration and lower mobility than the values obtained in bulk, because of the scattering at the surface [187]. This suggests that electrons detected by the coupled modes in pristine InAs nanowire come from the presence of states at the surface, and are located in the accumulation layer at the surface of the nanowire. Such an interpretation is in agreement with the disappearance of coupled modes for the Al_2O_3-coated nanowires. In fact, it is known that Al_2O_3 presents negative charge surface states at the interface [188]. This results in a decrease of electron concentration in the accumulation layer. To support the hypothesis that electrons are confined in the accumulation layer, we can look at the decrease of the mobility for temperatures below ~ 50 K, which is typically due to impurities or surface scattering, and that indicates the proximity of carriers to the surface. On the contrary, the increase of the mobility with the temperature above ~ 50 K is the trend expected to be limited by acoustic or optical phonon scattering in bulk materials. However, the mobility resulting from these scattering effects should be two order of magnitude higher than the experimental value [189]. To explain such a discrepancy, we need consider additional scattering mechanisms.

The limitation in the mobility can be assigned to the carrier-carrier interaction. Gupta et al. [183] provided an interesting interpretation for the trend in temperature, as well as values similar to our results for the mobility of InAs nanowires. The authors showed that the trend of mobility with the temperature, characterized by a peak at around ~ 50 K, could be ascribed to

the Coulomb scattering from ionized surface states. With the constant number of scatters, the probability of scattering with the ionized states decreases with the temperature, leading to an increase of the mobility. However, by increasing the temperature, an increase of the scatters occurs due to the thermally activation, together with a decrease of the mobility. The balance of these two effects can give rise to an initial increase and a subsequent decrease of the mobility with the temperature.

We turn now to $InAs_{1-x}Sb_x$ nanowires. The carrier concentration extracted from the fits of Raman spectra slightly increase with the temperature, reaching a value of $1.6{\cdot}10^{17}$ cm^{-3} at room temperature. This value is lower than with respect to the intrinsic one ($\sim 10^{16}$ cm^{-3}) [190]. On the contrary the mobility decrease with the temperature, passing from a value of 17500 cm^2/(Vs) at 14 K to a value of 8300 cm^2/(Vs) at room temperature. The presence of Al_2O_3 does not change the Raman spectra, and consequently the extracted mobility and concentration.

In fact, due to the strong dependence of the Fermi level pinning on the surface preparation and reconstruction, this effect depends also on the material composition. The presence of antimony indicates a difference in surface Fermi level pinning position, as demonstrated in $InAs_{1-x}Sb_x$ nanowires [191]. Moreover, we expect that also Al_2O_3 modifies the Fermi level pinning, as in the case of InAs. We suppose that the carriers are located in the inner part of the nanowire, and originate from spurious impurities, probably due to the presence of the alloying elements. This is consistent with the fact that the carrier concentration and the mobility are not influenced by the presence of Al_2O_3 capping layer.

The observed trend of the mobility with the temperature is consistent with the calculated mobility considering all the possible scattering mechanism in an alloy system [192]. However, in $InAs_{1-x}Sb_x$ bulk material a decrease of the mobility with the temperature is found [193]. In thin films, this trend is explained by the presence of dislocation scattering effect due to the growth of $InAs_{1-x}Sb_x$ on InAs, GaAs, InSb substrate [192]. However, in our nanowires there are no dislocations owing to geometries stand relaxation.

Despite that the calculated trends of the mobility as a function of the temperature in bulk material and in nanowires are similar, the absolute values are not of the same order. The mobilities observed here in nanowires are lower than the theoretically predicted value and measured one for bulk material (30000 cm^2/(Vs) at room temperature for n 10^{17} cm^{-3} [194]). Other scattering mechanisms should be proposed in order to explain this. Among them, scattering due to alloy inhomogeneity could act as a limiting mechanism in the mobility. In fact, $InAs_{1-x}Sb_x$ nanowire presents an antimony content homogeneous in the core, but slightly lower content of antimony in the shell and anti-segregation of antimony at the six corners of the hexagonal cross section [179], as a consequence of the radial growth.

In addition, considering the dimension and the morphology of nanowires, surface scattering may play a relevant role in limiting the mobility. In order to determine the influence of surface scattering, a systematic study on a series of nanowires with different diameter should be performed.

5 Conclusions and Outlook

In this thesis, we investigated the functional properties of Nanowires by Raman spectroscopy. Thanks to its non-destructive and spatial resolution, micro-Raman spectroscopy is a powerful contact-less tool for the characterization of semiconductor nanowires.

The first part of the thesis was dedicated to the study of the relation between the photonic properties of nanowires and the effect on the Raman spectroscopy measurements.

We have studied the effects on the Raman spectra, in terms of spatial selectivity and macroscopic selection rules. At the beginning, we have performed Raman spectroscopy with different wavelength on GaAs/AlGaAs core-shell nanowires, grown by self-catalyzed molecular beam epitaxy. Nanowires with different Aluminum contents and different diameter and shell thicknesses were also grown. We have used Raman spectroscopy to determine the chemical composition of GaAs/AlGaAs core-shell nanowires. We have found that the Raman spectra are dependent on the the excitation energy in a non-intuitive way, compared to what expected dependences in thin films.

By considering the distribution of the photonic modes within the nanowire as a function of the excitation wavelength, we were able to address the differences in the Raman spectra as a function of the excitation wavelength. FDTD simulations for the distribution of the electric field inside the nanowire were performed to validate the results. Effectively, photonic modes allow to selectively probe different areas in the nanowires, by using the appropriate wavelength.

Furthermore, we have taken advantage of the photonic nature of the light-nanowire interaction, to enhance the response of the longitudinal optical modes. Through the coupling of plasmon, longitudinal optical mode is usually used to characterize free-carrier by Raman spectroscopy. Raman scattering signal in bulk material is subject to certain selection rules, which depend on the light direction and polarization of the incoming and scattered light, as well as on the symmetry of the vibrational modes.

Raman selection rules predict that the LO mode is forbidden in back-scattering configuration

on $(1\bar{1}0)$ surface in a zinc-blende structure. Therefore, nanowires with $(1\bar{1}0)$ facets that are horizontally lying on a substrate are not expected to show the coupled mode. Polarized Raman scattering was performed both on nanowires lying down on the substrate and on nanowires freely suspended over a trench. In the freely suspended nanowire, higher signal and higher intensity ratio between LO and TO modes were observed, especially for the perpendicular polarization. We explained this behavior in terms of the changes in the direction and polarization of the internal field inside the nanowire. The results were validated with FDFD simulations for the local direction and polarization of the light.

Cross-polarized configuration on freely-suspended nanowires was used to detect the coupling of LO phonon with the free carriers, in p-type GaAs nanowires. From the coupling, we quantified the carriers concentration and the mobility of the nanowire. This method can be also applied to other systems, as we did for InAs and InAsSb nanowires.

The second part of the thesis concerned the assessment of carrier concentration and mobility in expected high mobility system, such as GaAs/AlGaAs modulation doping and InAsSb nanowires, by Raman spectroscopy.

One of the most promising possibilities that nanowires enable is modulation doping, as inspired from the structures that led to record high mobilities in planar III-V samples. A GaAs nanowire core is coated with an AlGaAs shell containing a delta-doping structure. Doping in the shell at a certain distance from the core provides carriers in the GaAs core, while reducing drastically impurity scattering at low temperatures. Overall, this should lead to the increase in carrier mobility by various orders of magnitude.

Raman measurements were performed on GaAs/AlGaAs modulation Si doped and undoped samples, as a function of the temperature. Modulation doping samples showed a decrease and a broadening of the LO mode of GaAs with the temperature. This mode was identified as a LO phonon-plasmon coupled mode.

Afterwards, we analyzed the LO phonon-plasmon couple modes (LOPPCM), obtaining the carriers concentration and the mobility. We have found that in modulation doped samples, the dopants are almost completely ionized for temperature above 50 K. Moreover, a decrease of mobility with the temperature and a dependence with the electron concentration were observed. We found a mobility of 2750 $cm^2/(Vs)$ in modulation doped nanowire at low temperature. We believe that the main mechanism limiting mobility is the interface scattering. This hypothesis is supported by simulations of carrier density distribution, which show a shift from the center of the core to the edge for increasing temperature. As a consequence, we believe that an improvement of the interface characteristics may increase the mobility.

Finally, we analyzed InAs and InAsSb nanowires by Raman spectroscopy. The high-frequency coupled mode for InAs, and the low-frequency and the intermediate-frequency coupled mode (typical of ternary alloy) for InAsSb, were identified. Fitting the LOPPCM spectra, we estimated the concentration and the mobility of electrons in the systems. An increase of both the mobility

and the concentration with the antimony content was found.

Measurements as a function of the temperature were carried out on pristine InAs and InAsSb nanowires, and on coated with Al_2O_3 InAs and InAsSb nanowires. These measurements aimed to understand the origin of the carriers and the region where they are. The presence of the coated Al_2O_3 layer around the nanowire causes the disappearance the high frequency mode in InAs, meanwhile leave unchanged the spectra of InAsSb. Our results suggest that electrons in InAs are located in the accumulation layer, being originated from the Fermi level pinning. On the contrary, electrons in InAsSb are presents in the inner part of the nanowire and are originated from spurious impurities. We discussed the possible scattering mechanisms which governed the mobility in these system, as alloy inhomogeneities and surface scattering.

In conclusion we applied Raman Spectroscopy as a non-destructive tool to study the functional properties of III-V semiconductor nanowires. This technique allowed to determine optical and electrical properties of nanowire. We can expect that from the study of the effects of photonic modes on the Raman spectra, strong implications for the use of Raman spectroscopy as local chemical characterization technique will follow. Moreover, we believe to have found a fast and accurate method to assess carriers in GaAs nanowire, without having to implement more difficult Raman configurations. This method can be also applied to other systems, as we did for InAs and InAsSb nanowires. The knowledge gained from the study of Modulation doped nanowires can be be used for the design of future high mobility nanoscale devices. At the moment, the application of modulation doping scheme looks very promising also on other systems such as nanomembranes. Preliminary simulations reveal the possibility to obtain 1D channel. These systems can benefit of their defect-free nature. Finally, we believe that our work on InAsSb yields an important contribution to the understanding of the carrier system on nanowire. For the future, it would be interesting to study the influence of surface scattering by performing a systematic study of nanowires having different diameters. The work on InAsSb also points the way for other studies, aiming the characterization of more complex structures, as InAs/GaSb core-shell nanowires.

A Supporting Information

A.1 Growth protocol

Self-catalyzed GaAs/$Al_xGa_{1-x}As$ core/shell nanowires have been grown on undoped 2"Si(111) substrate by using a DCA P600 molecular beam epitaxy machine. The nanowire core structures have been grown under a flux of Ga equivalent to a planar growth rate between 0.26 and 0.28 $\AA$/s, a V/III ratio between 45 and 60, at a temperature of 625°C and under a rotation of 7 r.p.m. After the growth of the core, the conditions were then switched from axial to radial growth by lowering the substrate temperature and increasing the As pressure up to $1.2 \cdot 10^{-5}$ Torr. $Al_xGa_{1-x}As$ shells have been grown with Al compositions x=0.25, 0.50 and 0.70 and capped with a 5 nm thick GaAs shell to prevent oxidation. For clarity the growth conditions are summarized in Fig. A.1.

SAMPLE	GaAs CORE			AlGaAs SHELL	
	Ga rate (Å/s)	V/III ratio	Growth Temp (°C)	Al conc (%)	Thickness (nm)
1	0.28	45	625	25	10
2	0.28	45	625	50	65
3	0.26	60	625	70	60

Figure A.1 – Ga equivalent growth rate, V/III ratio and substrate temperature used for the growth of the nanowire core of the different samples studied in the paper. Thickness and aluminum concentration of the relative $Al_xGa_{1-x}As$ shells.

A.2 Movie

The electric field energy density in the nanowires is calculated with Meep by using FDTD (Finite Difference Time Domain) method. A time domain electromagnetically simulation simply takes Maxwell's equations and evolves them over time within some finite computation

regime. In FDTD methods the time and the space are divided into a rectangular grid. After a certain initiation time, the system reaches a steady state: the steady state is not really stationary but shows a periodicity. Attached are the animated gif of the periodic steady state for GaAs/ $Al_xGa_{1-x}As$ core/shell nanowire with x=50% when excited by a top plane wave of 488.0 nm (A.2a) and 647.1 nm (A.2b) wavelengths.

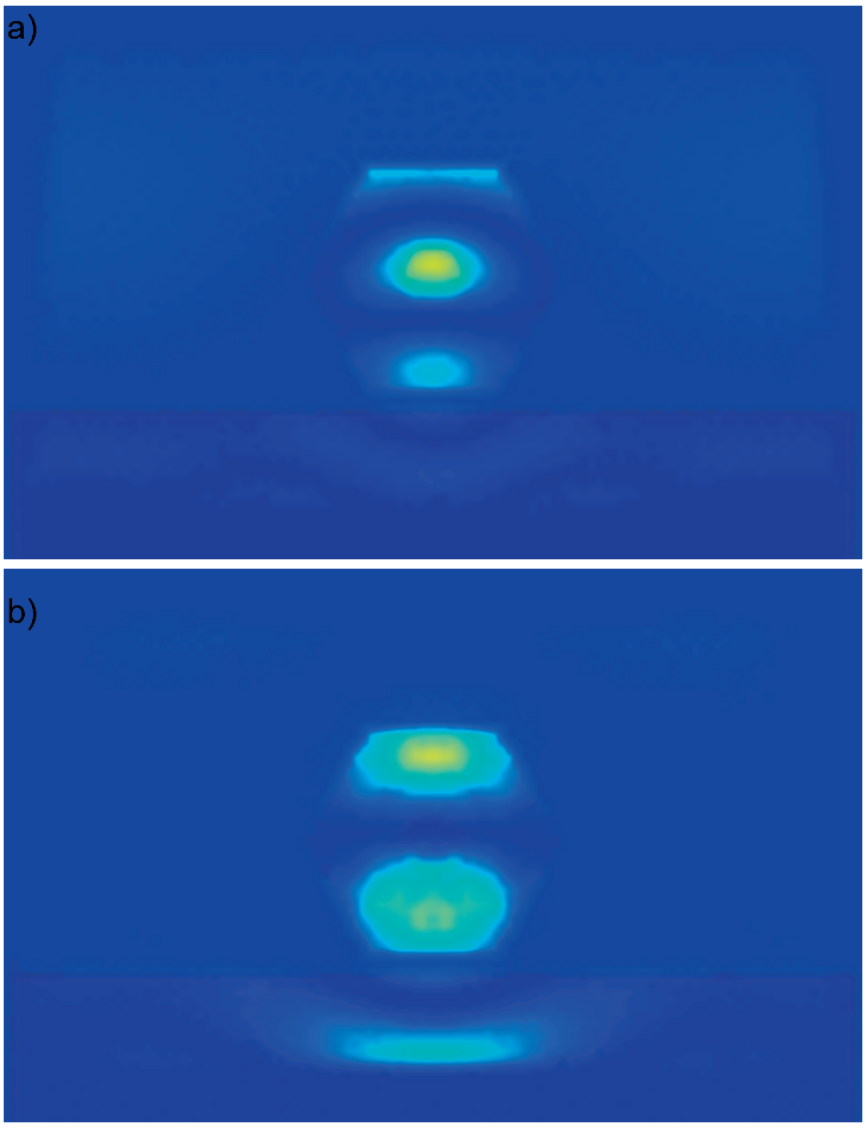

Figure A.2 – Evolution in time of the electric energy density for GaAs/$Al_{0.5}Ga_{0.5}As$ core/shell nanowire when excited by a top plane wave of 488.0 nm (a) and 647.1 nm (b) wavelength (enhanced online).

Bibliography

[1] J. Bardeen and W. H. Brattain, "The transistor, a semi-conductor triode," *Physical Review*, vol. 74, no. 2, p. 230, 1948.

[2] J. Kilby and E. Keonjian, "Design of a semiconductor-solid-circuit adder," in *Electron Devices Meeting, 1959 International*, pp. 76–78, IEEE, 1959.

[3] W. Lu and C. M. Lieber, "Nanoelectronics from the bottom up," *Nature materials*, vol. 6, no. 11, pp. 841–850, 2007.

[4] Z. I. Alferov, "The double heterostructure: Concept and its applications in physics, electronics and technology," *International Journal of Modern Physics B*, vol. 16, no. 05, pp. 647–675, 2002.

[5] F. Dimroth and S. Kurtz, "High-efficiency multijunction solar cells," *MRS bulletin*, vol. 32, no. 03, pp. 230–235, 2007.

[6] R. Wagner and W. Ellis, "Vapor-liquid-solid mechanism of single crystal growth," *Applied Physics Letters*, vol. 4, no. 5, pp. 89–90, 1964.

[7] M. Yazawa, M. Koguchi, and K. Hiruma, "Heteroepitaxial ultrafine wire-like growth of inas on gaas substrates," *Applied Physics Letters*, vol. 58, no. 10, pp. 1080–1082, 1991.

[8] H. Riel, L.-E. Wernersson, M. Hong, and J. A. Del Alamo, "Iii–v compound semiconductor transistors - from planar to nanowire structures," *MRS Bulletin*, vol. 39, no. 08, pp. 668–677, 2014.

[9] A. M. Ionescu and H. Riel, "Tunnel field-effect transistors as energy-efficient electronic switches," *Nature*, vol. 479, no. 7373, pp. 329–337, 2011.

[10] P. Krogstrup, H. Jorgensen, M. Heiss, O. Demichel, J. Holm, M. Aagesen, J. Nygard, and A. Fontcuberta i Morral, "Single-nanowire solar cells beyond the shockley-queisser limit," *Nature Photonics*, vol. 7, p. 306, 2013.

[11] S. Yazji, M. Swinkels, M. De Luca, E. Hoffmann, D. Ercolani, S. Roddaro, G. Abstreiter, L. Sorba, E. Bakkers, and I. Zardo, "Assessing the thermoelectric properties of single insb nanowires: the role of thermal contact resistance," *Semiconductor Science and Technology*, vol. 31, no. 6, p. 064001, 2016.

[12] M. H. Huang, S. Mao, H. Feick, H. Yan, Y. Wu, H. Kind, E. Weber, R. Russo, and P. Yang, "Room-temperature ultraviolet nanowire nanolasers," *science*, vol. 292, no. 5523, pp. 1897–1899, 2001.

[13] J. C. Johnson, H.-J. Choi, K. P. Knutsen, R. D. Schaller, P. Yang, and R. J. Saykally, "Single gallium nitride nanowire lasers," *Nature materials*, vol. 1, no. 2, pp. 106–110, 2002.

[14] A. Chin, S. Vaddiraju, A. Maslov, C. Ning, M. Sunkara, and M. Meyyappan, "Near-infrared semiconductor subwavelength-wire lasers," *Applied Physics Letters*, vol. 88, no. 16, p. 163115, 2006.

[15] P. K. Sahoo, R. Janissen, M. P. Monteiro, A. Cavalli, D. M. Murillo, M. V. Merfa, C. L. Cesar, H. F. Carvalho, A. A. de Souza, E. P. Bakkers, *et al.*, "Nanowire arrays as cell force sensors to investigate adhesin-enhanced holdfast of single cell bacteria and biofilm stability," *Nano letters*, vol. 16, no. 7, pp. 4656–4664, 2016.

[16] A. Cho and J. Arthur, "Molecular beam epitaxy," *Progress in Solid State Chemistry*, vol. 10, pp. 157 – 191, 1975.

[17] C. Colombo, D. Spirkoska, M. Frimmer, G. Abstreiter, and A. Fontcuberta i Morral, "Ga-assisted catalyst-free growth mechanism of GaAs nanowires by molecular beam epitaxy," *Phys. Rev. B*, vol. 77, p. 155326, 2008.

[18] I. Zardo, S. Conesa-Boj, F. Peiro, J. R. Morante, J. Arbiol, E. Uccelli, G. Abstreiter, and A. Fontcuberta i Morral, "Raman spectroscopy of wurtzite and zincblende GaAs nanowires-polariyation dependence, selection rules ans strain effects," *Phys. Rev. B*, vol. 80, p. 245324, 2009.

[19] Y. Xiang, L. Cao, S. Conesa-Boj, S. Estrade, J. Arbiol, F. Peiro, M.Heiss, I. Zardo, J. R. Morante, M. L. Brongersma, and A. Fontcuberta i Morral, "Single crystalline and core-shell indium-catalyzed germanium nanowires-a systematic thermal CVD growth study," *Nanotech.*, vol. 20, p. 245608, 2009.

[20] I. Zardo, A. F. i Morral, and G. Abstreiter, *Raman spectroscopy on semiconductor nanowires.* INTECH Open Access Publisher, 2010.

[21] D. Spirkoska, G. Abstreiter, and A. Fontcuberta i Morral, "Size and environment dependence of surface phonon modes of gallium arsenide nanowires as measured by raman spectroscopy," *Nanotech.*, vol. 19, p. 435704, 2008.

[22] R. Gupta, Q. Xiong, G. D. Mahan, and P. C. Eklund, "Surface optical phonons in gallium phosphide nanowires," *Nano Lett.*, vol. 3, p. 1745, 2003.

[23] J. Fréchette and C. Carraro, "Diameter-dependent modulation and polarization anisotropy in raman scattering from individual nanowires," *Physical Review B*, vol. 74, no. 16, p. 161404, 2006.

[24] L.Cao, B.Nabet, and J. Spanier, "Enhanced raman scattering from individual semiconductor nanocones and nanowires," *Phys. Rev. Lett.*, vol. 96, p. 157402, 2006.

[25] A. Casadei, E. A. Llado, F. Amaduzzi, E. Russo-Averchi, D. Rüffer, M. Heiss, L. Dal Negro, and A. F. i Morral, "Polarization response of nanowires à la carte," *Scientific reports*, vol. 5, p. 7651, 2015.

[26] E. Alarcon-Llado, S. Conesa-Boj, X. Wallart, P. Caroff, and A. Fontcuberta i Morral, "Raman spectroscopy of self-catalyzed $GaAs_{1-x}Sb_x$ nanowires grown on silicon," *Nanotech.*, vol. 24, p. 405707, 2013.

[27] X. Wang, I. Zardo, D. Spirkoska, S. Yazji, K. W. Ng, W. S. Ko, C. J. Chang-Hasnain, J. J. Finley, and G. Abstreiter, "Valence band splitting in wurtzite ingaas nanoneedles studied by photoluminescence excitation spectroscopy," *ACS nano*, vol. 8, no. 11, pp. 11440–11446, 2014.

[28] B. Ketterer, M. Heiss, E. Uccelli, J. Arbiol, and A. Fontcuberta i Morral, "Untangling the electronic band structure of wurtzite gaas nanowires by resonant raman spectroscopy," *ACS nano*, vol. 5, no. 9, pp. 7585–7592, 2011.

[29] I. Zardo, S. Yazji, N. Ho?rmann, S. Hertenberger, S. Funk, S. Mangialardo, S. Morko?tter, G. Koblmu?ller, P. Postorino, and G. Abstreiter, "E1 (a) electronic band gap in wurtzite inas nanowires studied by resonant raman scattering," *Nano letters*, vol. 13, no. 7, pp. 3011–3016, 2013.

[30] B.Ketterer, E. Mikheev, E. Uccelli, and A. F. i Morral, "Compensation mechanism in silicon-doped gallium arsenide nanowires," *Applied Physics Letters*, vol. 97, p. 223103, 2010.

[31] A. Mooradian and G. Wright, "Observation of the interaction of plasmons with longitudinal optical phonons in GaAs," *Physical Review Letters*, vol. 16, p. 999, 1966.

[32] K. Wan, J. Young, R. Devine, W. Moore, A. SpringThorpe, C. Miner, and P. Mandeville, "Free carrier density determination in p-type GaAs using raman scattering from coupled plasmon-phonon modes," *Journal of Applied Physics*, vol. 63, p. 5598, 1988.

[33] B. Ketterer, E. Uccelli, and A. Fontcuberta i Morral, "Mobility and carrier density in p-type GaAs nanowires measured by transmission raman spectroscopy," *Nanoscale*, vol. 4, p. 1789, 2012.

[34] B. Ketterer, *Raman Spectroscopy of GaAs Nanowires.* PhD thesis, STI, Lausanne, 2011.

[35] H. Kressel, J. Dunse, H. Nelson, and F. Hawrylo, "Luminescence in silicon-doped gaas grown by liquid-phase epitaxy," *Journal of Applied Physics*, vol. 39, no. 4, pp. 2006–2011, 1968.

[36] L. Titova, T. Hoang, H. Jackson, L. Smith, J. Yarrison-Rice, Y. Kim, H. Joyce, H. Tan, and C. Jagadish, "Temperature dependence of photoluminescence from single core-shell GaAs/AlGaAs nanowires," *Applied Physics Letters*, vol. 89, p. 173126, 2006.

[37] M. Hocevar, T. T. Giang, R. Songmuang, M. den Hertog, L. Besombes, J. Bleuse, Y.-M. Niquet, and N. T. Pelekanos, "Residual strain and piezoelectric effects in passivated GaAs/AlGaAs core-shell nanowires," *Applied Physics Letters*, vol. 102, p. 191103, 2013.

[38] V. Dhaka, J. Oksanen, H. Jiang, T. Haggren, A. Nykanen, R. Sanatinia, J.-P. Kakko, T. Huhtio, M. Mattila, J. Ruokolainen, S. Anand, E. Kauppinen, and H. Lipsanen, "Aluminum-induced photoluminescence red shifts in core-shell GaAs/$Al_xGa_{1-x}As$ nanowires," *Nano Letters*, vol. 13, p. 3581, 2013.

[39] Z. Yang, A. Surrente, G. Tutuncuoglu, K. Galkowski, M. Cazaban-Carrazé, F. Amaduzzi, P. Leroux, D. K. Maude, A. Fontcuberta i Morral, and P. Plochocka, "Revealing large-scale homogeneity and trace impurity sensitivity of GaAs nanoscale membranes," *Nano Letters*, vol. 17, no. 5, pp. 2979–2984, 2017. PMID: 28440658.

[40] H. Joyce, J. Wong-Leung, C.-K. Yong, C. J. Docherty, S. Paiman, Q. Gao, H. H. Tan, C. Jagadish, J. Lloyd-Hughes, L. M. Herz, and M. B. Johnston, "Ultralow surface recombination velocity in InP nanowires probed by terahertz spectroscopy," *Nano Letters*, vol. 12, p. 5325, 2012.

[41] H. J. Joyce, C. J. Docherty, Q.Gao, H. H. Tan, C. Jagadish, J. Lloyd-Hughes, L. M. Herz, and M. B. Johnston, "Electronic properties of GaAs, InAs and InP nanowires studied by terahertz spectroscopy," *Nanotech.*, vol. 24, p. 214006, 2013.

[42] J. L. Boland, S. Conesa-Boj, P. Parkinson, G. Tutuncuoglu, F. Matteini, D. Ruffer, A. Casadei, F. Amaduzzi, F. Jabeen, C. L. Davies, H. J. Joyce, L. M. Herz, A. Fontcuberta i Morral, and M. B. Johnston, "Modulation doping of GaAs/AlGaAs core-shell nanowires with effective defect passivation and high electron mobility," *Nano Letters*, vol. 15, no. 2, pp. 1336–1342, 2015.

[43] J. Waugh and G. Dolling, "Crystal dynamics of gallium arsenide," *Physical Review*, vol. 132, no. 6, p. 2410, 1963.

[44] R. Carles, N. Saint-Cricq, J. Renucci, M. Renucci, and A. Zwick, "Second-order raman scattering in InAs," *Physical Review B*, vol. 22, no. 10, p. 4804, 1980.

[45] Y.-S. Chen, W. Shockley, and G. Pearson, "Lattice vibration spectra of $GaAs_xP_{1-x}$ single crystals," *Physical Review*, vol. 151, no. 2, p. 648, 1966.

[46] M. Ilegems and G. L. Pearson, "Infrared reflection spectra of $ga_{1-x}al_xAs$ mixed crystals," *Phys. Rev. B*, vol. 1, pp. 1576–1582, Feb 1970.

[47] H. W. Verleur and A. S. Barker, "Infrared lattice vibrations in $Gaas_yp_{1-y}$ alloys," *Phys. Rev.*, vol. 149, pp. 715–729, Sep 1966.

[48] M. Brodsky, G. Lucovsky, M. Chen, and T. Plaskett, "Infrared reflectivity spectra of the mixed crystal system $Ga_{1-x}In_xSb$," *Physical Review B*, vol. 2, no. 8, p. 3303, 1970.

[49] M. Brodsky and G. Lucovsky, "Infrared reflection spectra of $Ga_{1-x}In_xAs$: A new type of mixed-crystal behavior," *Physical Review Letters*, vol. 21, no. 14, p. 990, 1968.

[50] G. Lucovsky and M. Chen, "Long wave optical phonons in the alloy systems: $Ga_{1-x}In_xAs$, $GaAs_{1-x}Sb_x$ and $InAs_{1-x}Sb_x$," *Solid State Communications*, vol. 8, no. 17, pp. 1397–1401, 1970.

[51] P. Yu and M. Cardona, *Fundamentals of Semiconductors.* Berlin: Springer, Berlin, 1996.

[52] W. Hayes and R. Loudon, *Scattering of Light by Crystals.* Mineola: Dover Publications, 2004.

[53] M. Cardona, *Light Scattering in Solids I.* Springer-Verlag Berlin Heidelberg, 1983.

[54] R. Loudon, "Theory of the first-order raman effect in crystals," *Proceedings of the Royal Society of London A: Mathematical, Physical and Engineering Sciences*, vol. 275, no. 1361, pp. 218–232, 1963.

[55] H. Zeng, W. Cai, B. Cao, J. Hu, Y. Li, and P. Liu, "Surface optical phonon raman scattering in Zn/ZnO core-shell structured nanoparticles," *Applied physics letters*, vol. 88, no. 18, p. 181905, 2006.

[56] D. Olego and M. Cardona, "Raman scattering by coupled LO-phonon-plasmon modes and forbidden TO-phonon raman scattering in heavily doped p-type GaAs," *Phys. Rev. B*, vol. 24, pp. 7217–7232, Dec 1981.

[57] T. Kozawa, T. Kachi, H. Kano, Y. Taga, M. Hashimoto, N. Koide, and K. Manabe, "Raman scattering from lo phonon-plasmon coupled modes in gallium nitride," *Journal of Applied Physics*, vol. 75, no. 2, pp. 1098–1101, 1994.

[58] B. Jusserand, D. Richards, G. Fasol, G. Weimann, and W. Schlapp, "Single particle excitations and plasmons in a single asymmetric modulation-doped GaAs quantum well," *Surface Science*, vol. 229, no. 1-3, pp. 394–397, 1990.

[59] G. Fasol, N. Mestres, H. P. Hughes, A. Fischer, and K. Ploog, "Raman scattering by coupled-layer plasmons and in-plane two-dimensional single-particle excitations in multi-quantum-well structures," *Phys. Rev. Lett.*, vol. 56, pp. 2517–2520, Jun 1986.

[60] U. Nowak, W. Richter, and G. Sachs, "LO-phonon-plasmon dispersion in GaAs hydrodynamical theory and experimental results," *physica status solidi (b)*, vol. 108, no. 1, pp. 131–143, 1981.

[61] N. D. Mermin, "Lindhard dielectric function in the relaxation-time approximation," *Physical Review B*, vol. 1, no. 5, p. 2362, 1970.

[62] D.V.Murphy and S. Brueck, "Enhanced raman scattering from silicon microstructures," *Optics Letters*, vol. 8, p. 9, 1983.

[63] T. Livneh, J. Zhang, G. Cheng, and M. Moskovits, "Polarized raman scattering from single GaN nanowires," *Phys. Rev. B*, vol. 74, p. 035320, 2006.

[64] L.Cao, J. White, J. Park, J. Schuller, B.M.Clemens, and M. Brongersma, "Engineering light absorption in semiconductor nanowire devices," *Nat. Mat.*, vol. 8, p. 643, 2009.

[65] G.Mie, "Beitragezur optiktruber medien, speziell kolloidaler metallosungen," *Annales der Physick*, vol. 25, p. 377, 1908.

[66] F.J.Lopez, J.K.Hyun, U.Givan, I.S.Kim, and A. Holsteen, "Diameter and polarization-dependent raman scattering intensities of semiconductor nanowires," *NanoLett.*, vol. 12, p. 2266, 2012.

[67] X. Duan, Y. Huang, R. Agarwal, and C. Lieber, "Single-nanowire electrically driven lasers," *Nature*, vol. 421, p. 241, 2003.

[68] C.Soci, A. Zhang, B. Xiang, S. A. Dayeh, D. Aplin, J. Park, X. Bao, Y. H. Lo, and D. Wang, "ZnO nanowire UV photodetectors with high internal gain," *NanoLett.*, vol. 7, p. 1003, 2007.

[69] E. C. Garnett, M. L. Brongersma, Y. Cui, and M. D. McGehee, "Nanowire solar cells," *Annu. Rev. Mater. Sci.*, vol. 41, p. 269, 2011.

[70] E.Garnett and P. Yang, "Light trapping in silicon nanowire solar cells," *NanoLett.*, vol. 10, no. 3, p. 1082, 2010.

[71] M. D. Kelzenberg, S. W. Boettcher, J. A. Petykiewicz, D. B. Turner-Evans, M. C. Putnam, E. L. Warren, J. M. Spurgeon, R. M. Briggs, and H. A. Lewis, Nathan S.and Atwater, "Enhanced absorption and carrier collection in Si wire arrays for photovoltaic applications," *Nat. Mat.*, vol. 9, p. 368, 2010.

[72] J. R. Maiolo, B. M. Kayes, M. A. Filler, M. C. Putnam, M. D. Kelzenberg, H. A. Atwater, and N. S. Lewis, "High aspect ratio silicon wire array photoelectrochemical cells," *J. Am. Chem. Soc.*, vol. 129, no. 41, pp. 12346–12347, 2007.

[73] Y. Cui, Q. Wei, H. Park, and C. M. Lieber, "Nanowire nanosensors for highly sensitive and selective detection of biological and chemical species," *Science*, vol. 293, no. 5533, pp. 1289–1292, 2001.

[74] M. S. Gudiksen, L. J. Lauhon, J. Wang, and C. M. Smith, David C.and Lieber, "Growth of nanowire superlattice structures for nanoscale photonics and electronics," *Nat. Mat.*, vol. 415, p. 617, 2002.

[75] D. Saxena, S. Mokkapati, P. Parkinson, N. Jiang, Q. Gao, H. H. Tan, and C. Jagadish, "Optically pumped room-temperature GaAs nanowire lasers," *Nat. Phot.*, vol. 7, p. 963, 2013.

[76] Y. Wang, V. Schmidt, S. Senz, and U. Goesele, "Epitaxial growth of silicon nanowires using an aluminium catalyst," *Nat. Nanotechnol.*, vol. 1, p. 186, 2006.

[77] B. Mandl, J. Stangl, T. Martensson, A. Mikkelsen, J. Eriksson, L. S. Karlsson, G. Bauer, L. Samuelson, and W. Seifert, "Au-free epitaxial growth of InAs nanowires," *NanoLett.*, vol. 6, p. 1817, 2006.

[78] C. J. Novotny and P. K. L. Yu, "Vertically aligned, catalyst-free InP nanowires grown by metalorganic chemical vapor deposition," *Appl. Phys. A*, vol. 87, p. 203111, 2005.

[79] E. A. Stach, P. J. Pauzauskie, T. Kuykendall, J. Goldberger, R. He, and P. Yang, "Watching GaN nanowires grow," *NanoLett.*, vol. 3, p. 867, 2003.

[80] C. P. T. Svensson, W. Seifert, M. W. Larsson, L. R. Wallenberg, J.Stangl, G. Bauer, and L. Samuelson, "Epitaxially grown GaP/$GaAs_{1-x}P_x$/GaP double heterostructure nanowires for optical applications," *Nanotech.*, vol. 16, p. 936, 2005.

[81] K. A. Dick, S. Kodambaka, M. C. Reuter, K. Deppert, L. Samuelson, W. Seifert, L. R. Wallenberg, and F. M. Ross, "The morphology of axial and branched nanowire heterostructures.," *Nano Letters*, vol. 7, p. 1817, 2007.

[82] N. Zakharov, P. Werner, G. Gerth, L. Schubert, L. Sokolov, and U. Goesele, "Growth phenomena of Si and Si/Ge nanowires on Si (111) by molecular beam epitaxy," *J. Cryst. Growth*, vol. 290, p. 6, 2006.

[83] J. Noborisaka, J. Motohisa, S. Hara, and T. Fukui, "Fabrication and characterization of freestanding GaAs/AlGaAs core-shell nanowires and AlGaAs nanotubes by using selective-area metalorganic vapor phase epitaxy," *Appl. Phys. Lett.*, vol. 87, p. 093109, 2005.

[84] F.Qian, M.Brewster, S.K.Lim, Y.Ling, C.Greene, O. Laboutin, J.W.Johnson, S. Gradecak, Y. Cao, and Y. Li, "Controlled synthesis of AlN/GaN multiple quantum well nanowire structures and their optical properties," *NanoLett.*, vol. 12, no. 6, p. 3344, 2012.

[85] F.Qian, S.Gradecak, Y. Li, C. Wen, and C. Lieber, "Core/multishell nanowire heterostructures as multicolor, high-efficiency light-emitting diodes," *NanoLett.*, vol. 5, no. 11, pp. 2287–2291, 2005.

[86] F. Qian, Y. Li, S. Gradecak, D. Wang, C. J. Barrelet, and C. M. Lieber, "Gallium nitride-based nanowire radial heterostructures for nanophotonics," *NanoLett.*, vol. 4, no. 10, pp. 1975–1979, 2004.

[87] M. Fickenscher, T. Shi, H. E. Jackson, L. M. Smith, J. M. Yarrison-Rice, C. Zheng, P. Miller, J. Etheridge, B. M. Wong, Q. Gao, S. Deshpande, H. H. Tan, and C. Jagadish, "Optical, structural, and numerical investigations of GaAs/AlGaAs core-multishell nanowire quantum well tubes," *NanoLett.*, vol. 13, no. 3, pp. 1016–1022, 2013.

[88] C. Zheng, J.Wong-Leung, Q. Gao, H. H. Tan, C. Jagadish, and J. Etheridgel, "Polarity-driven 3-fold symmetry of GaAs/AlGaAs core multishell nanowires," *NanoLett.*, vol. 13, p. 3742, 2013.

[89] M. Heiss, Y. Fontana, A. Gustafsson, G. Wust, C. Magen, D. D. O. Regan, J. W. Luo, B. Ketterer, S. Conesa-Boj, A. V. Kuhlmann, J. Houel, E.Russo-Averchi, J. R. Morante, M. Cantoni, N. Marzari, J. Arbiol, A.Zunger, R. J. Warburton, and A. Fontcuberta i Morral, "Self-assembled quantumdots in a nanowire system for quantum photonics," *Nat. Mat.*, vol. 12, p. 439, 2013.

[90] D. E. Perea, E. R. Hemesath, E. J. Schwalbach, J. L. Lensch-Falk, P. W. Voorhees, and L. J. Lauhon, "Direct measurement of dopant distribution in an individual vapoura liquida solid nanowire," *Nat. Nanotechnol.*, vol. 4, p. 315, 2009.

[91] P. Parayanthal, F. H. Pollak, and J. M. Woodall, "Raman scattering characterization of $Ga_{1-x}Al_xAs$/GaAs heterojunctions: Epilayer and interface," *Appl. Phys. Lett.*, vol. 41, p. 961, 1982.

[92] S. Hernandez, R.Cusco, D. Pastor, L. Artus, K. P. ODonnell, R. W. Martin, I. M. Watson, Y. Nanishi, and E. Calleja, "Raman-scattering study of the InGaN alloy over the whole composition range," *J. Appl. Phys.*, vol. 98, p. 013511, 2005.

[93] P. M. Mooney, F. H. Dacol, J. C. Tsang, and J. O. Chu, "Raman scattering analysis of relaxed Ge_xSi_{1-x} alloy layers," *Appl. Phys. Lett.*, vol. 62, p. 2069, 1993.

[94] G. Signorello, E. Lortscher, P. Khomyakov, S. Karg, D. Dheeraj, B. Gotsmann, H. Weman, and H. Riel, "Inducing a direct-to-pseudodirect bandgap transition in wurtzite GaAs nanowires with uniaxial stress," *Nat. Commun*, vol. 5, no. 7, p. 3655, 2014.

[95] G. Signorello, S. Karg, M. Bjork, B. Gotsmann, and H. Riel, "Tuning the light emission from GaAs nanowires over 290 mev with uniaxial strain," *NanoLett.*, vol. 13, no. 3, p. 917, 2013.

[96] G. Chen, J. Wu, Q. Lu, H. R. Gutierrez, Q. Xiong, M. E. Pellen, J. S. Petko, D. H. Werne, and P. C. Eklund, "Optical antenna effect insemiconducting nanowires," *NanoLett.*, vol. 8, p. 1341, 2008.

[97] J. Wang, M. S. Gudiksen, X. Duan, Y. Cui, and C. M. Lieber, "Highly polarized photoluminescence and photodetection from single indium phosphide nanowires," *Science*, vol. 293, p. 1455, 2001.

[98] X. Wang, C. J. Summers, and Z. L. Wang, "Large-scale hexagonal-patterned growth of aligned zno nanorods for nano-optoelectronics and nanosensor arrays," *NanoLett.*, vol. 4, p. 423, 2004.

[99] L. Cao, P. Fan, A. P. Vasudev, J. S. White, Z. Yu, W. Cai, J. A. Schuller, S. Fan, and M. L. Brongersma, "Semiconductor nanowire optical antenna solar absorbers," *NanoLett.*, vol. 10, p. 439, 2010.

[100] S. A.Mann and E. Garnett, "Extreme light absorption in thin semiconductor films wrapped around metal nanowires," *NanoLett.*, vol. 13, no. 7, p. 3173, 2013.

[101] E. Kim, A. Steinbruck, M. T. Buscaglia, V. Buscaglia, T. Pertsch, and R. Grange, "Second-harmonic generation of single BaTiO3 nanoparticles down to 22nm diameter," *ACS Nano*, vol. 7, p. 5343, 2013.

[102] F. Dutto, C. Raillon, K. Schenk, and A. Radenovic, "Nonlinear optical response in single alkaline niobate nanowires," *NanoLett.*, vol. 11, p. 2517, 2011.

[103] F. Dutto, M. Heiss, A. Lovera, O. Lopez-Sanchex, A. Fontcuberta i Morral, and A. Radenovic, "Enhancement of second harmonic signal in nanofabricated cones," *NanoLett.*, vol. 13, p. 6048, 2013.

[104] E. Uccelli, J. Arbiol, C. Magen, P. Krogstrup, E. Russo-Averchi, M. Heiss, G. Mugny, F. Morier-Genoud, J. Nygard, J. Morante, and A. Fontcuberta i Morral, "Three-dimensional multiple-order twinning of self-catalyzed GaAs nanowires on Si substrates," *Nano Lett.*, vol. 11, p. 3827, 2011.

[105] E. Russo-Averchi, M. Heiss, L. Michelet, P. Krogstrup, J. Nygard, C. Magen, J. R. Morante, E. Uccelli, J.Arbiol, and A. Fontcuberta i Morral, "Suppression of three dimensional twinning for a 100% yield of vertical GaAs nanowires on silicon," *Nanoscale*, vol. 4, p. 1486, 2012.

[106] M. Heigoldt, J. Arbiol, D. Spirkoska, J. M. Rebled, S. Conesa-Boj, G. Abstreiter, F. Peiró, J. R. Morante, and A. Fontcuberta i Morral, "Long range epitaxial growth of prismatic heterostructures on the facets of catalyst-free GaAs nanowires," *J. Mater. Chem.*, vol. 19, p. 840, 2009.

[107] D. C. Watson, R. V. Martinez, Y. Fontana, E. Russo-Averchi, M. Heiss, A. Fontcuberta i Morral, G. M. Whitesides, and M. Loncar, "Nanoskiving core-shell nanowires: A new fabrication method for nano-optics," *NanoLett.*, vol. 14, p. 524, 2014.

[108] L. Ouattara, A. Mikkelsen, N. Skold, J. Eriksson, T. Knaapen, E. Cavar, W. Seifert, L. Samuelson, and E. Lundgren, "GaAs/AlGaAs nanowire heterostructures studied by scanning tunneling microscopy," *NanoLett.*, vol. 7, p. 2859, 2007.

[109] A. F. Oskooi, D. Roundy, M. Ibanescu, P. Bermel, J. Joannopoulos, and S. G. Johnson, "Meep: A flexible free-software package for electromagnetic simulations by the FDTD method," *Comput. Phys. Commun.*, vol. 181, p. 687, 2010.

[110] D. E. Aspnes, S. M. Kelso, R. Logan, and R. Bhat, "Optical properties of $Al_xGa_{1-x}As$," *J. Appl. Phys.*, vol. 60, p. 754, 1986.

[111] C.S.Wang, J. Chen, R.Becker, and A.Zdetsis, "Second order raman spectrum and phonon density of states of silicon," *Phys. Lett. A*, vol. 44, p. 517, 1973.

[112] S. Adachi, "GaAs, AlAs, and $Al_xGa_{1-x}As$: Material parameters for use in research and device applications," *J. Appl. Phys.*, vol. 58, p. R1, 1985.

[113] J. Menendez and M. Cardona., "Temperature dependence of the first-order raman scattering by phonons in Si, Ge, and α – Sn: Anharmonic effects," *Phys.Rev.B*, vol. 29, p. 2051, 1984.

[114] A.Volkmer, "Vibrational imaging and microspectroscopies based on coherent antistokes raman scattering microscopy," *J.Phys. D: Appl. Phys.*, vol. 38, p. R59, 2005.

[115] J.Zhang, L. Zhang, and W. Xu, "Surface plasmon polaritons: physics and applications," *J.Phys. D: Appl. Phys.*, vol. 45, p. 113001, 2012.

[116] R. Cuscó, E. Alarcón-Lladó, L. Artús, W. S. Hurst, and J. E. Maslar, "Raman scattering by LO-phonon-plasmon coupled modes in $Ga_{1-x}In_xAs_ySb_{1-y}$: Role of Landau damping," *Phys. Rev. B*, vol. 81, p. 195212, 2010.

[117] L. Cao, B. Garipcan, E. M. Gallo, S. S. Nonnenmann, B. Nabet, and J. Spanier, "Excitation of local field enhancement on silicon nanowires," *NanoLett.*, vol. 8, p. 601, 2008.

[118] L. Cao, L. Laim, P. Valenzuela, B. Nabet, and J. Spanier, "On the raman scattering from semiconducting nanowires," *Journal of Raman Spectroscopy*, vol. 38, p. 697, 2007.

[119] O. M. Berengue, A. Rodrigues, C. Dalmaschio, A. J. C. Lanfredi, E. Leite, and A. J.Chiquito, "Structural characterization of indium oxide nanostructures: a raman analysis," *J. Phys. D: Appl. Phys*, vol. 43, p. 045401, 2010.

[120] K.Jeganathan, R. Debnath, R. Meijers, T. Stoica, R. Calarco, D. Grutzmacher, and H. Luth, "Raman scattering of phonon-plasmon coupled modes in self-assembled GaN nanowire," *Journal of Applied Physics*, vol. 105, p. 123707, 2009.

[121] H. J. Joyce, P. Parkinsonand, N. Jiang, C. J. Docherty, Q.Gao, H. H. Tan, C. Jagadish, L. M. Herz, and M. B. Johnston, "Electron mobilities approaching bulk limits in "Surface-Free" GaAs nanowires," *NanoLetters*, vol. 14, p. 5989, 2014.

[122] M. Brewster, O. Schimek, S. Reich, and S. Gradecak, "Exciton-phonon coupling in individual gaas nanowires studied using resonant raman spectroscopy," *Phys. Rev. B*, vol. 80, p. 201314, 2009.

[123] F. Amaduzzi, E. Alarcon-Llado, E. Russo-Averchi, F. Matteini, M. Heiss, G. Tutuncoglu, S. Conesa-Boj, M. de la Mata, J. Arbiol, and A. F. i Morral, "Probing inhomogeneous composition in core/shell nanowires by raman spectroscopy," *Journal of Applied Physics*, vol. 116, p. 184303, 2014.

[124] S. Funk, M. Royo, I. Zardo, D. Rudolph, S. Morktter, B. Mayer, J. Becker, A. Bechtold, S. Matich, M. Dblinger, M. Bichler, G. Koblmuller, J. J. Finley, A. Bertoni, G. Goldoni, and G. Abstreiter, "High mobility one- and two-dimensional electron systems in nanowire-based quantum heterostructures," *NanoLett.*, vol. 13, p. 6189, 2013.

[125] H. Abe, H. Harima, S. Nakashima, M. Tani, K. Sakai, Y. Tokuda, K. Kanamoto, and Y. Abe, "Characterization of crystallinity in low-temperature-grown GaAs layers by raman scattering and time-resolved photoreflectance measurements," *Japanese Journal of Applied Physics*, vol. 35, p. 5955, 1996.

[126] Y. Wooa, T. Kangb, and T. Kimc, "Improvement of the crystallinity of a GaAs epitaxial film grown on a Si substrate using a Si/SiGe/Ge buffer layer," *Thin Solid Films*, vol. 279, p. 166, 1996.

[127] D. Aspnes, S. Kelso, R. Logan, and R. Bhata, "Optical properties of $\mathrm{al}_x\mathrm{ga}_{1-x}$ as," *Journal of Applied Physics*, vol. 60, p. 754, 1986.

[128] D. Aspnes and A. Studna, "Dielectric functions and optical parameters of Si, Ge, GaP, GaAs, GaSb, InP, InAs, and InSb from 1.5 to 6.0 ev," *Phys. Rev. B*, vol. 27, p. 985, 1983.

[129] D. Hon and W. L. Faust, "Dielectric parameterization of raman lineshapes for GaP with a plasma of charge carriers," *Appl. Phys. A*, vol. 1, p. 241, 1973.

[130] N. W. Ashcroft and N. D. Mermin, *Solid State Physics.* Philadelphia: Holt, Rineheart and Winston, 1976.

[131] C. Flytzanis, "Electro-optic coefficients in III-V compounds," *Applied Physics Letters*, vol. 23, p. 1136, 1969.

[132] J. Blakemore, "Semiconducting and other major properties of gallium arsenide," *Journal of Applied Physics*, vol. 53, p. R123, 1982.

[133] A. Casadei, J. Schwender, E. Russo-Averchi, D. Ruffer, M. Heiss, E. Alarcón-Lladó, F. Jabeen, M. Ramezani, K. Nielsch, and A. Fontcuberta i Morral, "Electrical transport in C-doped GaAs nanowires: surface effects," *physica status solidi (RRL)-Rapid Research Letters*, vol. 7, pp. 890–893, 2013.

[134] J. Lowney and H. S.Bennett, "Majority and minority electron and hole mobilities in heavily doped GaAs," *Journal of Applied Physics*, vol. 69, p. 7102, 1991.

[135] M. Brown, M. Melloch, and M.S.Lundstrom, "Transistor based measurements of electron injection currents in p-type GaAs doped 10^{18}-10^{20}," *Applied Physics Letters*, vol. 56, p. 160, 1990.

[136] R. Dingle, H. Störmer, A. Gossard, and W. Wiegmann, "Electron mobilities in modulation-doped semiconductor heterojunction superlattices," *Applied Physics Letters*, vol. 33, no. 7, pp. 665–667, 1978.

[137] L. Pfeiffer, K. West, H. Stormer, and K. Baldwin, "Electron mobilities exceeding 107 cm2/v s in modulation-doped gaas," *Applied Physics Letters*, vol. 55, no. 18, pp. 1888–1890, 1989.

[138] W. Walukiewicz, H. E. Ruda, J. Lagowski, and H. C. Gatos, "Electron mobility in modulation-doped heterostructures," *Phys. Rev. B*, vol. 30, pp. 4571–4582, Oct 1984.

[139] C. Schüller, *Inelastic light scattering of semiconductor nanostructures: fundamentals and recent advances*, vol. 219. Springer Science & Business Media, 2006.

[140] E. Burstein, A. Pinczuk, and S. Buchner, "Resonance inelastic light scattering by charge carriers at semiconductor surfaces," *Physics of Semiconductors*, pp. 1231–1234, 1978.

[141] G. Abstreiter and K. Ploog, "Inelastic light scattering from a quasi-two-dimensional electron system in gaas-al x ga 1- x as heterojunctions," *Physical Review Letters*, vol. 42, no. 19, p. 1308, 1979.

[142] A. Pinczuk, H. Störmer, R. Dingle, J. Worlock, W. Wiegmann, and A. Gossard, "Observation of intersubband excitations in a multilayer two dimensional electron gas," *Solid State Communications*, vol. 32, no. 11, pp. 1001–1003, 1979.

[143] A. Pinczuk, J. Worlock, H. Störmer, R. Dingle, W. Wiegmann, and A. Gossard, "Intersubband spectroscopy of two dimensional electron gases: Coulomb interactions," *Solid State Communications*, vol. 36, no. 1, pp. 43–46, 1980.

[144] D. A. Dahl and L. Sham, "Electrodynamics of quasi-two-dimensional electrons," *Physical Review B*, vol. 16, no. 2, p. 651, 1977.

[145] A. Pinczuk and J. Worlock, "Light scattering by two-dimensional electron systems in semiconductors," *Surface Science*, vol. 113, no. 1-3, pp. 69–84, 1982.

[146] G. Fishman, "Energy levels and coulomb matrix elements in doped gaas-(gaal) as multiple-quantum-well heterostructures," *Physical Review B*, vol. 27, no. 12, p. 7611, 1983.

[147] A. Pinczuk, J. Worlock, H. Störmer, A. Gossard, and W. Wiegmann, "Light scattering spectroscopy of electrons in gaas–(alga) as heterostructures: Correlation with transport properties," *Journal of Vacuum Science and Technology*, vol. 19, no. 3, pp. 561–563, 1981.

[148] A. Bertoni, M. Royo, F. Mahawish, and G. Goldoni, "Electron and hole gas in modulation-doped gaas/al$_{1-x}$ga$_x$as radial heterojunctions," *Phys. Rev. B*, vol. 84, p. 205323, Nov 2011.

[149] M. Hilse, M. Ramsteiner, S. Breuer, L. Geelhaar, and H. Riechert, "Incorporation of the dopants si and be into gaas nanowires," *Applied Physics Letters*, vol. 96, no. 19, p. 193104, 2010.

[150] D. Spirkoska, A. Fontcuberta i Morral, J. Dufouleur, Q. Xie, and G. Abstreiter, "Free standing modulation doped core–shell gaas/algaas hetero-nanowires," *physica status solidi (RRL)-Rapid Research Letters*, vol. 5, no. 9, pp. 353–355, 2011.

[151] J. Xiao, Z. Hong, Z. Rongxiu, and J. Zhao, "Interface roughness scattering in an algaas/-gaas triangle quantum well and square quantum well," *Journal of Semiconductors*, vol. 34, no. 7, p. 072004, 2013.

[152] J. Ibáñez, R. Cuscó, E. Alarcón-Lladó, L. Artús, A. Patanè, D. Fowler, L. Eaves, K. Uesugi, and I. Suemune, "Electron effective mass and mobility in heavily doped n-gaasn probed by raman scattering," *Journal of Applied Physics*, vol. 103, no. 10, p. 103528, 2008.

[153] G. Irmer, M. Wenzel, and J. Monecke, "The temperature dependence of the lo (t) and to (t) phonons in gaas and inp," *physica status solidi (b)*, vol. 195, no. 1, pp. 85–95, 1996.

[154] A. G. Milnes, *Deep impurities in semiconductors*. Wiley, 1973.

[155] Y. Li, F. Qian, J. Xiang, and C. M. Lieber, "Nanowire electronic and optoelectronic devices," *Materials today*, vol. 9, no. 10, pp. 18–27, 2006.

[156] J. A. Del Alamo, "Nanometre-scale electronics with III-V compound semiconductors," *Nature*, vol. 479, no. 7373, pp. 317–323, 2011.

[157] V. Mourik, K. Zuo, S. M. Frolov, S. Plissard, E. Bakkers, and L. P. Kouwenhoven, "Signatures of majorana fermions in hybrid superconductor-semiconductor nanowire devices," *Science*, vol. 336, no. 6084, pp. 1003–1007, 2012.

[158] S. R. Plissard, I. Van Weperen, D. Car, M. A. Verheijen, G. W. Immink, J. Kammhuber, L. J. Cornelissen, D. B. Szombati, A. Geresdi, S. M. Frolov, *et al.*, "Formation and electronic properties of InSb nanocrosses," *Nature nanotechnology*, vol. 8, no. 11, pp. 859–864, 2013.

[159] M. Heiss, S. Conesa-Boj, J. Ren, H.-H. Tseng, A. Gali, A. Rudolph, E. Uccelli, F. Peiró, J. R. Morante, D. Schuh, *et al.*, "Direct correlation of crystal structure and optical properties in wurtzite/zinc-blende GaAs nanowire heterostructures," *Physical Review B*, vol. 83, no. 4, p. 045303, 2011.

[160] C. Thelander, P. Caroff, S. Plissard, A. W. Dey, and K. A. Dick, "Effects of crystal phase mixing on the electrical properties of inas nanowires," *Nano letters*, vol. 11, no. 6, pp. 2424–2429, 2011.

[161] N. Vainorius, S. Lehmann, D. Jacobsson, L. Samuelson, K. A. Dick, and M.-E. Pistol, "Confinement in thickness-controlled GaAs polytype nanodots," *Nano letters*, vol. 15, no. 4, pp. 2652–2656, 2015.

[162] K. A. Dick, C. Thelander, L. Samuelson, and P. Caroff, "Crystal phase engineering in single InAs nanowires," *Nano letters*, vol. 10, no. 9, pp. 3494–3499, 2010.

[163] H. J. Joyce, J. Wong-Leung, Q. Gao, H. H. Tan, and C. Jagadish, "Phase perfection in zinc blende and wurtzite III-V nanowires using basic growth parameters," *Nano letters*, vol. 10, no. 3, pp. 908–915, 2010.

[164] E. Dimakis, J. La?hnemann, U. Jahn, S. Breuer, M. Hilse, L. Geelhaar, and H. Riechert, "Self-assisted nucleation and vapor-solid growth of InAs nanowires on bare Si (111)," *Crystal Growth & Design*, vol. 11, no. 9, pp. 4001–4008, 2011.

[165] T. Grap, T. Rieger, C. Blömers, T. Schäpers, D. Grützmacher, and M. Lepsa, "Self-catalyzed VLS grown InAs nanowires with twinning superlattices," *Nanotechnology*, vol. 24, no. 33, p. 335601, 2013.

[166] K. A. Dick, P. Caroff, J. Bolinsson, M. E. Messing, J. Johansson, K. Deppert, L. R. Wallenberg, and L. Samuelson, "Control of III-V nanowire crystal structure by growth parameter tuning," *Semiconductor Science and Technology*, vol. 25, no. 2, p. 024009, 2010.

[167] S. Conesa-Boj, D. Kriegner, X.-L. Han, S. Plissard, X. Wallart, J. Stangl, A. Fontcuberta i Morral, and P. Caroff, "Gold-free ternary III-V antimonide nanowire arrays on silicon: twin-free down to the first bilayer," *Nano letters*, vol. 14, no. 1, pp. 326–332, 2013.

[168] X. Yuan, P. Caroff, J. Wong-Leung, H. H. Tan, and C. Jagadish, "Controlling the morphology, composition and crystal structure in gold-seeded $GaAs_{1-x}Sb_x$ nanowires," *Nanoscale*, vol. 7, no. 11, pp. 4995–5003, 2015.

[169] C. Patel and R. E. Slusher, "Light scattering by plasmons and landau levels of electron gas in inas," *Physical Review*, vol. 167, no. 2, p. 413, 1968.

[170] S. Buchner and E. Burstein, "Raman scattering by wave-vector-dependent LO-phonon-plasmon modes in n-InAs," *Physical Review Letters*, vol. 33, no. 15, p. 908, 1974.

[171] Y. B. Li, I. T. Ferguson, R. A. Stradling, and R. Zallen, "Raman scattering by plasmon-phonon modes in highly doped n-inas grown by molecular beam epitaxy," *Semiconductor Science and Technology*, vol. 7, no. 9, p. 1149, 1992.

[172] D. Kirillov, Y. Chai, C. Webb, and G. Davis, "Raman scattering by coupled plasmon-phonon modes in n-type ga1- x al x as epitaxial layers," *Journal of applied physics*, vol. 59, no. 1, pp. 231–233, 1986.

[173] J. Maslar, J. Dorsten, P. Bohn, S. Agarwala, I. Adesida, C. Caneau, and R. Bhat, "Electron-phonon interactions in n-type in 0.53 ga 0.47 as and in 0.52 al 0.48 as studied by inelastic light scattering," *Physical Review B*, vol. 50, no. 23, p. 17143, 1994.

[174] M. Qi, M. Konagai, and K. Takahashi, "Raman scattering from longitudinal-optical phonon-plasmon-coupled mode in carbon-doped p-type ingaas," *Journal of applied physics*, vol. 78, no. 12, pp. 7265–7268, 1995.

[175] K. Sinha, A. Mascarenhas, S. R. Kurtz, and J. Olson, "Determination of free carrier concentration in n-gainp alloy by raman scattering," *Journal of applied physics*, vol. 78, no. 4, pp. 2515–2519, 1995.

[176] A. Mintairov and H. Temkin, "Lattice vibrations and phonon-plasmon coupling in raman spectra of p-type in 0.53 ga 0.47 as," *Physical Review B*, vol. 55, no. 8, p. 5117, 1997.

[177] Y. Li, S. Dosanjh, I. Ferguson, A. Norman, A. De Oliveira, R. Stradling, and R. Zallen, "Raman scattering in inas1-xsbx alloys grown on gaas by molecular beam epitaxy," *Semiconductor science and technology*, vol. 7, no. 4, p. 567, 1992.

[178] A. Rogalski, *New ternary alloy systems for infrared detectors.* SPIE Press, 1994.

[179] H. Potts, M. Friedl, F. Amaduzzi, K. Tang, G. Tutuncuoglu, F. Matteini, E. Alarcon-Llado, P. C. McIntyre, and A. Fontcuberta i Morral, "From twinning to pure zincblende catalyst-free InAs(Sb) nanowires," *Nano Letters*, vol. 16, no. 1, pp. 637–643, 2016. PMID: 26686394.

[180] F. Amaduzzi, E. Alarcón-Lladó, H. Hautmann, R. Tanta, F. Matteini, G. Tütüncüo?lu, T. Vosch, J. Nygård, T. Jespersen, E. Uccelli, *et al.*, "Tuning the response of non-allowed raman modes in gaas nanowires," *Journal of Physics D: Applied Physics*, vol. 49, no. 9, p. 095103, 2016.

[181] G. Abstreiter, E. Bauser, A. Fischer, and K. Ploog, "Raman spectroscopy: A versatile tool for characterization of thin films and heterostructures of GaAs and $Al_xGa_{1-x}As$," *Applied Physics A: Materials Science & Processing*, vol. 16, no. 4, pp. 345–352, 1978.

[182] T. R. Hart, R. L. Aggarwal, and B. Lax, "Temperature dependence of raman scattering in silicon," *Phys. Rev. B*, vol. 1, pp. 638–642, Jan 1970.

[183] N. Gupta, Y. Song, G. W. Holloway, U. Sinha, C. M. Haapamaki, R. R. LaPierre, and J. Baugh, "Temperature-dependent electron mobility in inas nanowires," *Nanotechnology*, vol. 24, no. 22, p. 225202, 2013.

[184] L. Olsson, C. Andersson, M. Håkansson, J. Kanski, L. Ilver, and U. O. Karlsson, "Charge accumulation at inas surfaces," *Physical review letters*, vol. 76, no. 19, p. 3626, 1996.

[185] C. Castleton, A. Höglund, M. Göthelid, M. Qian, and S. Mirbt, "Hydrogen on iii-v (110) surfaces: Charge accumulation and stm signatures," *Physical Review B*, vol. 88, no. 4, p. 045319, 2013.

[186] E. Halpern, G. Elias, A. Kretinin, H. Shtrikman, and Y. Rosenwaks, "Direct measurement of surface states density and energy distribution in individual inas nanowires," *Applied Physics Letters*, vol. 100, no. 26, p. 262105, 2012.

[187] C. Affentauschegg and H. H. Wieder, "Properties of inas/inalas heterostructures," *Semiconductor science and technology*, vol. 16, no. 8, p. 708, 2001.

[188] G. Agostinelli, A. Delabie, P. Vitanov, Z. Alexieva, H. Dekkers, S. De Wolf, and G. Beaucarne, "Very low surface recombination velocities on p-type silicon wafers passivated with a dielectric with fixed negative charge," *Solar Energy Materials and Solar Cells*, vol. 90, no. 18, pp. 3438–3443, 2006.

[189] O. Madelung, *Physics of III-V compounds.* J. Wiley, 1964.

[190] A. Rogalski and K. Jozwikowski, "Intrinsic carrier concentration and effective masses in $InAs_{1-x}Sb_x$," *Infrared Physics*, vol. 29, no. 1, pp. 35 – 42, 1989.

[191] C. Thelander, P. Caroff, S. Plissard, and K. A. Dick, "Electrical properties of inas1- xsbx and insb nanowires grown by molecular beam epitaxy," *Applied Physics Letters*, vol. 100, no. 23, p. 232105, 2012.

[192] R. J. Egan, V. W. L. Chin, and T. L. Tansley, "Dislocation scattering effects on electron mobility in InAsSb," *Journal of Applied Physics*, vol. 75, no. 5, pp. 2473–2476, 1994.

[193] M. Y. Yen, "Molecular-beam epitaxial growth and electrical properties of lattice mismatched $InAs_{1-x}Sb_x$ on (100) GaAs," *Journal of Applied Physics*, vol. 64, no. 6, pp. 3306–3309, 1988.

[194] G. Stringfellow and P. Greene, "Liquid phase epitaxial growth of inas1- x sb x," *Journal of The Electrochemical Society*, vol. 118, no. 5, pp. 805–810, 1971.

Francesca Amaduzzi
born on 19.07.1986
in Teramo, Italy

Chemin de la Roche, 6
1020 Renens VD (Suisse)
amaduzzi.francesca@gmail.com

Education

PhD in Materials Science and Technology Jan. 2013–Jul. 2017
École Polytechnique Fédérale de Lausanne (Switzerland)
Master in Physics cum laude Jan. 2009–Jan. 2012
Università Sapienza di Roma (Italy)
Bachelor in Physics Oct. 2005–Jan. 2009
Università Sapienza di Roma (Italy)

Teaching Assistant

Exercise class "Semiconductor materials and properties:from bulk to the nanostructures" for engineers in materials science (Master level) 2013–2016
Master student projects 2013–2016

Languages

Italian: Native speaker
English: Fluent
French: Intermediate

Technical Skills

Raman spectroscopy, Photoluminescence, Dielectric spectroscopy, Dynamic light scattering, Zeta potential measurement, UV-VIS spectroscopy, IR spectroscopy.

Informatics Competencies

Mathematica, Origin, Nextnano, Comsol Multiphysics, Meep.

Publications

[1] F. Amaduzzi, F. Bomboi, A. Bonincontro, F. Bordi, S. Casciardi, L. Chronopoulou, M. Diociaiuti, F. Mura, C. Palocci and S. Sennato, *Chitosan-DNA complexes: Charge inversion and DNA condensation*, Colloids and surfaces B: Biointerfaces, 2013, 114C, 1-10

[2] F. Amaduzzi, E. Alarcon Llado, E. Russo-Averchi, F. Matteini, M. Heiss, G. Tutuncuoglu, S. Conesa-Boj, M. de la Mata, J. Arbiol, and A. Fontcuberta i Morral, *Probing inhomogeneous composition in core/shell nanowires by Raman spectroscopy*, Journal of Applied Physics, 2014, 116(18), 184303

[3] A. Casadei, E. Alarcon Llado, F. Amaduzzi, E. Russo-Averchi, D. Ruffer, M. Heiss, L. Dal Negro, A. Fontcuberta i Morral, *Polarization response of nanowires à la carte*, Scientific Reports, 2015, 5, 7651

[4] J. L. Boland, S. Conesa-Boj, P. Parkinson, G. Tutuncuoglu, F. Matteini, D. Ruffer, A. Casadei, F. Amaduzzi, F. Jabeen, C.L. Davies, H.J. Joyce, L. M. Herz, A. Fontcuberta i Morral and M.B. Johnston, *Modulation Doping of GaAs/AlGaAs Core–Shell Nanowires With Effective Defect Passivation and High Electron Mobility*, Nano Letters, 2015, 15, 1336-1342

[5] H. Potts, M. Friedl, F. Amaduzzi, K. Tang, G. Tutuncuoglu, F. Matteini, E. Alarcon Llado, P.C. McIntyre, and A. Fontcuberta i Morral, *From Twinning to Pure Zincblende Catalyst-Free InAs(Sb) Nanowires*, Nano Letters, 2015, 16(1), 637–643

[6] F. Amaduzzi, E. Alarcon Llado, H. Hautmann, R. Tanta, F. Matteini, G. Tutuncuoglu, T. Vosch, J. Nygard, T. Jespersen, E. Uccelli and A. Fontcuberta i Morral, *Tuning the response of non-allowed Raman modes in GaAs nanowires*, Journal of Physics D Applied Physics, 2015, 49(9), 095103

[7] R. Tanta, T. Kanne, F. Amaduzzi, Z. Liao, M.H. Madsen, E. Alarcon Llado, P. Krogstrup, E. Johnson, A. Fontcuberta i Morral, T. Vosch, J. Nygard and T.S. Jespersen, *Morphology and composition of oxidized InAs nanowires studied by combined Raman spectroscopy and transmission electron microscopy*, Nanotechnology, 2016, 27(30), 305704

[8] Z. Yang, A. Surrente, G. Tutuncuoglu, K. Galkowski, M. Cazaban-Carrazé, F. Amaduzzi, P. Leroux, D. K. Maude, A. Fontcuberta i Morral, and P. Plochocka, *Revealing Large-Scale Homogeneity and Trace Impurity Sensitivity of GaAs Nanoscale Membranes*, Nano Letters, 2017, 17 (5), pp 2979–2984

[9] J. Vukajlovic Plestina, V. Derek, L. Francaviglia, H. Potts, F. Amaduzzi, M. Ivanda and A. Fontcuberta i Morral, *Nanoporous silicon tubes: the role of geometry in nanostructure formation and application to light emitting diodes*, Journal of Physics D: Applied Physics, Accepted Manuscript online 8 May 2017